Maladaptive nutrient signalling sustains the m.3243A>G mtDNA mutation

Chih-Yao Chung[1], Kritarth Singh[1], Vassilios N Kotiadis[1], Jee Hwan Ahn[1], Lida Kabir[1], Emilie Topley[1], Joycelyn Tan[1], William D Andrews[1], Nicoletta Plotegher[1,2], Graziano Guella[3], Robert D S Pitceathly[4], Gyorgy Szabadkai[1,5,6], Mariia Yuneva[6], Michael R Duchen[1,7,*]

1 Department of Cell and Developmental Biology and Consortium for Mitochondrial Research, UCL, Gower Street, London WC1E 6BT

2 Department of Biology, University of Padua, Padua, Italy

3 Bioorganic Chemistry Laboratory, Department of Physics, University of Trento, Trento, Italy

4 Department of Neuromuscular Diseases, UCL Queen Square Institute of Neurology and The National Hospital for Neurology and Neurosurgery

5 Department of Biomedical Sciences, University of Padua, Padua, Italy

6 The Francis Crick Institute, London

7 Lead Contact

*Correspondence: m.duchen@ucl.ac.uk

Keywords: mitochondria; mtDNA; mtDNA mutations; nutrient signalling; m.3243A>G; PI3K; Akt; mTORC1; mitophagy

ABSTRACT

Mutations of the mitochondrial genome (mtDNA) cause a range of profoundly debilitating clinical conditions for which treatment options are very limited. Most mtDNA diseases show heteroplasmy – tissues express both wild-type and mutant mtDNA. While the level of heteroplasmy broadly correlates with disease severity, the relationships between specific mtDNA mutations, heteroplasmy, disease phenotype and severity are not well-understood. We have found that the m.3243A>G mutation, the most prevalent mutation of mtDNA diseases and the major cause of mitochondrial encephalomyopathy, lactic acidosis and stroke-like episodes, leads to metabolic changes, promoting the upregulation of the PI3K-Akt-mTORC1 axis in patient-derived cells and tissues. Remarkably, pharmacological inhibition of PI3K, Akt, or mTORC1 activated mitophagy, reduced mtDNA mutant load and rescued cellular bioenergetics. The rescue was prevented by inhibition of mitophagy. The PI3K-Akt-mTORC1 axis thus represents a therapeutic target with translational potential that may benefit people suffering from the consequences of the m.3243A>G mutation.

31 **INTRODUCTION**

32 Mitochondria control cellular bioenergetic homeostasis and serve as a hub for cell metabolism and
33 cell signalling pathways. Human mitochondria contain a circular plasmid-like DNA (mtDNA) which
34 encodes 13 proteins which act as subunits of the electron transport chain (ETC) and 24 RNAs essential
35 for mitochondrial protein synthesis. Mutations of mtDNA affect around 1 in 5000 of the population
36 (Gorman et al., 2015) and cause a range of diseases for which no effective treatment is available
37 (Craven et al., 2017; Russell et al., 2020). Over half of the known pathogenic mutations are found
38 within tRNA genes, in which the m.3243A>G mutation, a $tRNA^{Leu}$ point mutation accounts for about
39 40% of adult patients of primary mitochondrial diseases (Gorman et al., 2015; Schon et al., 2012).
40 Clinically, patient symptoms associated with mtDNA mutations are highly heterogeneous (Russell et
41 al., 2020; Szczepanowska et al., 2012). The tissues primarily affected vary depending on the specific
42 mtDNA mutations, and our understanding of the relationships between mtDNA mutations, disease
43 phenotype and severity is still very limited (Craven et al., 2017; Russell et al., 2020). The majority of
44 diseases caused by mutations of mtDNA are heteroplasmic – tissues express both normal and
45 mutation carrying mtDNA. This is a confounding complication, as disease expression may differ
46 radically between patients with the same mutation but different mutant load. While disease severity
47 broadly correlates positively with the relative burden of mutant mtDNA, we know remarkably little
48 about the determinants of the mutant mtDNA burden (Craven et al., 2017; Maeda et al., 2016; Picard
49 and Hirano, 2016; Stewart and Chinnery, 2015).

50 Mitochondrial quality control pathways, including mitophagy, mitochondrial biogenesis pathways and
51 mitochondrial shaping mechanisms, are critically involved in regulating mitochondrial energy
52 homeostasis (Kotiadis et al., 2014; Valera-Alberni and Canto, 2018). Several studies have
53 demonstrated the accumulation of damaged mitochondria and defective mitophagy as a hallmark of
54 mtDNA diseases and age-related neurodegeneration, suggesting that the presence of pathogenic
55 mtDNA alone is not sufficient to drive selection against the mutation by the activation of mitophagy
56 (Cotán et al., 2011; Deus et al., 2020; Gilkerson et al., 2012; Morán et al., 2014; Plotegher and Duchen,
57 2017). We therefore asked how cell signalling pathways influence these pathways in the disease
58 model, as adaptive - or maladaptive – responses to impaired oxidative phosphorylation (OxPhos) and
59 changes in intermediary metabolism, and whether these pathways play a role as determinants of
60 mutant load and disease severity.

61 Here, we have characterised the metabolic phenotype of patient-derived cells bearing the m.3243A>G
62 ($tRNA^{Leu}$) mutation. This is the most common heteroplasmic mtDNA mutation (Gorman et al., 2015;
63 Schon et al., 2012), and, clinically, is expressed variably but may include diabetes, sensorineural

deafness, myopathy, encephalopathy, lactic acidosis and stroke-like episodes (MELAS). We have found that the expression and activity of the PI3K-Akt-mTORC1 pathway were increased in the mutant cells, and was strongly associated with redox imbalance, oxidative stress, and glucose dependence. Phosphorylation of Akt and ribosomal protein S6 (a downstream target of mTORC1) were also increased in muscle biopsies from other patients with the mutation, confirming that this signalling pathway is constitutively activated in patient tissues. Remarkably, inhibition of PI3K, Akt, or mTORC1 all substantially reduced mutant load and rescued mitochondrial bioenergetic function. We found that this process is mediated by upregulation of mitophagy which is absolutely required for rescue of mitochondrial function and reduction in mutant load. Our study reveals that in response to the m.3243A>G mutation, metabolism is rewired, and activity of the PI3K-Akt-mTORC1 axis is increased, as an adaptive response to metabolic changes driven by the mutation. The finding that inhibition of the pathway reduces mutant load and rescues function suggests that activation of this signalling pathway is, in fact, maladaptive, that activation of the pathway sustains disease progression and that pharmacological intervention in this signalling pathway represents a potential therapeutic strategy in patients with these dreadful diseases.

RESULTS

The m.3243A>G mutation causes mitochondrial dysfunction and glucose dependence, resulting in redox imbalance and oxidative stress.

To explore the metabolic and cell signalling impact of the m.3243A>G mutation, we used six cell lines: fibroblasts derived from two patients carrying the mutation, two controls matched for age and gender, an A549 cybrid cell line carrying the mutation and its Wild-type (WT) counterpart. PCR-RFLP (Nigou et al., 1998) and ARM-qPCR (Wang et al., 2011) were used to quantify the m.3243A>G mutation load in these cell models. One patient-derived line (henceforth referred to as patient 1) showed a mutant load of 86.2 ± 2.3%; a second line (referred to as patient 2) showed a mutant load of 30.3 ± 3.5%, and the mutant load was 79.0 ± 0.3% in the cybrid cells (Fig. 1A; for more details about the patients please see Methods).

To characterise the metabolic phenotype of the mutant cells, respiratory rate was measured using the Seahorse XFe96 extracellular flux analyser. These measurements showed a profound decrease in resting respiratory rate, ATP dependent respiration and in maximal respiratory capacity in both patient lines (Fig. 1B, D). Respiratory rates were also significantly reduced in the cybrid cells, when normalised to their increased mtDNA copy number (Fig. S1A), compared to the control A549 cells (Fig. 1C-D). In line with these findings, immunoblotting of respiratory chain supercomplexes using blue native gels electrophoresis (BNGE), which identify macromolecular assemblies, revealed disrupted expression of respiratory chain proteins in the mutant cells (Fig. 1E). Notably, there was a very large decrease in supercomplex I_2+ III_2 +IV_n, III_2+IV_1 and III_2/IV_2 assembly and in complex IV_1 (Fig. 1E). Mitochondrial membrane potential ($\Delta\psi_m$) was reduced in both patient-derived fibroblast lines (Fig. 1F) and the cybrid cells (Fig. S1B). The decrease in $\Delta\psi_m$ was significantly greater in cells from patient 1 than from patient 2, consistent with the greater mutant load in patient 1. Mitochondrial morphology was also altered in patient fibroblasts, showing significant fragmentation of the mitochondrial network, which was more severe in cells from patient 1 than from patient 2 (Fig. 1F).

Mitochondrial dysfunction may alter rates of free radical generation by the respiratory chain. The rate of increase of dihydroethidium (DHE) fluorescence (Fig. S1C), reflecting the intracellular rate of production of reactive oxygen species (ROS), was significantly increased both in patient fibroblasts and in the cybrid cells, compared to matched controls (Fig. 1G and S1D). MitoSOX, a mitochondria-targeted form of DHE, revealed a significant increase in the rate of ROS generation in the mitochondria in the mutant cells (Fig. 1G, ii; Fig. S1D, ii), suggesting that the increased rate of ROS generation is likely the consequence of an impaired respiratory chain. Together, the m.3243A>G mutation results in mitochondrial dysfunction, mitochondrial fragmentation and elevated ROS generation.

112 We wondered whether glucose metabolism is altered in the mutant cells, supporting their
113 bioenergetic homeostasis and compensating for the mitochondrial dysfunction. Using time-lapse live-
114 cell imaging, we quantified cell growth rates by fitting the curves of cell confluency with an exponential
115 cell growth model (Fig. S1E) under a variety of nutrient conditions. Growth rates were significantly
116 reduced in all mutant fibroblasts compared to their control counterparts (Fig. S1F). Moreover, the cell
117 proliferation rate was significantly reduced in all mutant cells in 1 and 5 mM glucose media (Fig. 1H
118 and S1G) but not in low concentrations of glutamine, suggesting that the patient-derived cells are
119 significantly more dependent on glucose metabolism. Consistently, the rate of uptake of the
120 fluorescent glucose analogue, 2-NBDG, was significantly increased in both patient fibroblasts and the
121 cybrid cells, compared to controls (Fig. 1I and S1H).

122 The cytosolic NADH:NAD^+ ratio is a function of glycolytic flux (which consumes NAD^+, generating
123 NADH), lactate production through lactate dehydrogenase (LDH) which produces lactate and
124 regenerates NAD^+ from NADH and the activity of malate/aspartate and the glycerol phosphate
125 shuttles that exchange NADH and NAD^+ between cytosol and mitochondrial matrix (Fig. 1J). We used
126 the genetically encoded reporter SoNar (Zhao et al., 2015) to quantify the cytosolic NADH:NAD^+ ratio
127 (Fig. S1I). The basal NADH:NAD^+ ratio was significantly increased in the patient fibroblasts and cybrid
128 cells compared to controls, consistent with reduced mitochondrial activity and higher glucose
129 catabolism through glycolysis (Fig. 1K and S1J). It was also consistent with significantly higher levels of
130 lactate produced by the patient fibroblasts compared to controls (Fig. 1L). The pH of the growth
131 media, reflecting cellular lactate production, was also measured using the absorbance of phenol red.
132 The acidification of media by mutant cells was significantly greater than that of controls (Fig S1K).
133 These data recapitulate the lactic acidosis which is characteristic of patients with the m.3243A>G
134 mutation (El-Hattab et al., 2015)**,** and suggest that in patient fibroblasts, increased activity of LDH may
135 compensate for the decreased regeneration of NAD^+ by mitochondria, supporting increased glycolytic
136 flux. Addition of exogenous pyruvate can support mitochondrial activity, increasing OxPhos, and
137 stimulate LDH activity to generate lactate, changing the NADH:NAD^+ ratio. In control cells, pyruvate
138 addition decreased the cytosolic NADH:NAD^+ ratio, but had a negligible effect on the high NADH:NAD+
139 ratio in mutant cells (Fig. 1K and S1J), suggesting that in the latter, LDH flux is already operating at its
140 maximum capacity. Together, these data confirm that in the mutant cells, decreased mitochondrial
141 activity results in higher glucose uptake, glucose catabolism into lactate and increased cytosolic
142 NADH:NAD^+ ratio.

143

144 **The m.3243A>G mutation remodels glucose and lipid metabolism towards increased anabolic**
145 **biosynthesis and lipid accumulation.**

146 To investigate the glucose-dependent metabolic alterations in the mutant cells and identify metabolic
147 signals which might result in cell signalling changes, glucose uniformly labelled with isotopic carbon
148 ([U-^{13}C]-glucose) was used to trace its metabolic fate in the cells by gas chromatography-mass
149 spectrometry (GC-MS). The pattern and abundance of ^{13}C enrichment in downstream metabolites
150 were used to determine the relative contribution of glucose into different metabolic pathways. First,
151 partial least squares discriminant analysis (PLS-DA) for the concentration of metabolites (Fig. S2A)
152 showed a clear separation between patient fibroblasts and controls (Fig. S2B). The analysis of
153 metabolic pathways revealed enrichment of lipid metabolism, pentose phosphate pathway (PPP),
154 glycolysis and the tricarboxylic acid (TCA) cycle (Fig. 2A). Tracing the fate of ^{13}C-glucose through
155 glycolysis (Fig. 2B), we found that the enrichment of ^{13}C in glucose-6-phosphate (G6P) in the mutant
156 cells was at a similar level as in controls (Fig 2B), but the total pools of G6P were increased (Fig. S2A)
157 consistent with increased glucose uptake. Although the end products of glycolysis, intracellular pools
158 of pyruvate and lactate in the mutant cells, were maintained at similar levels with controls in terms of
159 ^{13}C enrichments and concentrations (Fig. 2B and S2A), the levels and the ^{13}C enrichment of glycerol-3-
160 phosphate (G3P) were increased. The latter suggests the increased activity of glycerol-3-phosphate
161 dehydrogenase in response to increased cytosolic NADH/NAD$^+$ ratio, which may drive elevated lipid
162 biosynthesis (Fig. 2B). Interestingly, the levels of alanine were increased but its ^{13}C enrichment was
163 decreased, suggesting a contribution from other nutrient sources. Similarly, the total amount of serine
164 was increased in patient fibroblasts, despite decreased synthesis of serine from glucose, suggesting
165 increased serine uptake from extracellular media (Fig. 2B, S2A and S2C).

166 Consistent with OxPhos defects, levels of the TCA cycle intermediates, malate, fumarate and
167 succinate, were decreased in the mutant cells, while the levels of citrate were increased (Fig. S2A).
168 Interestingly, the enrichment of m+3 isotopologues of these TCA cycle intermediates and aspartate
169 were significantly increased in the mutant cells (Fig. 2B). To enter the TCA cycle, glucose-derived
170 pyruvate is converted into acetyl-CoA by pyruvate dehydrogenase (PDH). In this case the catabolism
171 of [U-^{13}C]-glucose results in m+2 enrichment of TCA cycle intermediates, including oxaloacetate (OAA),
172 a precursor of aspartate. In contrast, m+3 isotopologues of TCA cycle intermediates are generated if
173 pyruvate is converted into OAA by pyruvate carboxylase (PC). Metabolite set enrichment analysis of
174 the metabolomics data also predicted that PC is affected (Fig. S2D). Immunoblotting for phospho-PDH
175 and PC expression revealed elevated PC expression and increased levels of phosphorylated PDH
176 (indicating its reduced activity) in both patient fibroblasts and cybrid cells (Fig. 2C). As the glucose
177 contribution into the TCA cycle is usually low in conventional cell culture systems, this slight but
178 significant difference in the enrichment of ^{13}C is meaningful. The switch from PDH to PC as means of
179 channelling glucose-derived carbon into the TCA cycle in mutant fibroblasts is consistent with the

180 increased NADH/NAD+ ratio, which stimulates the activity of pyruvate dehydrogenase kinase,
181 phosphorylating PDH and inhibiting its activity.

182 As increased levels and glucose-derived enrichment of G3P suggest increased lipid biosynthesis, we
183 asked whether lipid metabolism is altered in the mutant cells. Nile Red O staining, which labels neutral
184 lipids, showed a substantial and significant accumulation of lipid droplets in the mutant cells,
185 increasing both the number and the area of droplets (Fig. 2D). Interestingly, accumulation of lipid
186 droplets has also been seen in biopsies from patients with MELAS (Golla et al., 2017). A systematic
187 lipidomic analysis using LC-MS showed that lipid profiles of patient fibroblasts were distinct from the
188 controls, with a striking increase in membrane and storage lipids, including
189 glycerophosphatidylinositols, cholesteryl esters and sphingomyelins (Fig. 2E). PLS-DA again showed a
190 clear separation of lipidomic profile between patient and control fibroblasts (Fig. S2E). Similarly, the
191 enrichment of metabolic pathways from the lipidomic data revealed upregulation of processes
192 involved in membrane lipid metabolism and signalling systems (Fig. S2F). Our findings from the stable-
193 isotope-labelling approach and comparative metabolomics thus reveal a profound remodelling of
194 glucose and lipid metabolism as a consequence of OxPhos defects arising from the m.3243A>G
195 mutation.

196

197 **The chronic activation of PI3K-Akt-mTORC1 in the m.3243A>G mutant cells impairs autophagy and**
198 **induces a deleterious integrated stress response**

199 The metabolic phenotype shown above points to reprogramming of nutrient-sensing signalling
200 networks in the m.3243A>G mutant cells. We therefore carried out an RNA sequencing screen to
201 examine global changes in the expression profiles of the patient fibroblasts. Using a significance level
202 of false discovery rate (FDR) < 0.05, we identified 3394 transcripts of which 1849 were upregulated
203 and 1545 were downregulated. A multi-dimensional principal component analysis also confirmed
204 good accordance between biological triplicates as well as close clustering of transcripts from patient
205 fibroblasts (Fig. S3A-C). The enrichment analysis of these differentially expressed genes identified
206 'mitochondrial dysfunction', 'superoxide radical degradation', 'Cholesterol biosynthesis' as the top-
207 scoring pathways in patient fibroblasts (Fig. 3A). Analysis of individual genes involved in these
208 pathways showed a general downregulation of OxPhos genes (Fig. S3D), but increased expression of
209 genes involved in oxidative stress defence pathways and membrane lipid synthesis/remodelling (Fig.
210 S3E-F). Specifically, the increased expression of PC was consistent with the immunoblotting data (Fig.
211 2C) and correlated with altered TCA cycle activity (Fig. S3G). The enhancement of glycolytic flux in the
212 mutant cells reported by the metabolomic data was supported by the increased expression of

213 hexokinase 1 (HK1). These findings further validated the metabolic footprint observed in patient-
214 derived cells from the metabolomic studies.

215 Consistent with the above results, the network analysis of upregulated genes identified the strong
216 enrichment of NRF2 signalling as well as PI3K-Akt and mTOR pathways in patient fibroblasts (Fig. 3B
217 and Fig. S4A; Table S1). We next validated these data at the protein expression level. Immunoblotting
218 confirmed increased phosphorylation of Akt compared to total Akt, as well as the downstream
219 mTORC1 target S6 ribosomal protein in patient fibroblasts (Fig. 3C) and the cybrid cells (Fig. S4B).
220 While control fibroblasts showed a growth factor-dependent Akt activation in response to increased
221 serum concentration in growth media, phospho-Akt was elevated in patient cells even when growth
222 factors were low (1% FBS) and increased only slightly in response to an elevated serum concentration.
223 Similarly, the patient fibroblasts exhibited increased mTORC1 activation independently of the serum
224 concentration, revealed by increased phospho-S6 levels. PI3K-Akt-mTORC1 signalling also antagonizes
225 the activity of the cellular energy sensor, AMP-activated protein kinase (AMPK) and suppresses
226 macromolecular catabolism by autophagy. We therefore measured AMPK phosphorylation in
227 response to different serum concentration by immunoblotting, but found no significant difference
228 between patient and control fibroblasts. These results suggest that the constitutive induction of PI3K-
229 Akt-mTORC1 signalling remodels cell metabolism, independently of growth factor stimulation.

230 We next explored the impact of chronic induction of PI3K-Akt-mTORC1 signalling on autophagic flux
231 in the mutant cells (Fig. 3D) (Deus et al., 2020; Manning and Toker, 2017). We monitored LC3B
232 turnover in the presence and absence of chloroquine (CQ) using LC3B immunoblotting. The mutant
233 cells showed an increased conversion to LC3BI to LC3BII form (autophagosome) but the difference in
234 LC3BII accumulation in the presence of CQ was not significantly different between control and mutant
235 cells (Fig. 3E and S4C), indicating a defect in the late stage of autophagosome to autolysosome
236 conversion/fusion in mutant cells. We also measured the autophagic flux using a mCherry-EGFP-LC3B
237 tandem reporter (N'Diaye et al., 2009) by live-cell imaging. Consistent with the above result, the ratio
238 of green/red puncta was low in control compared to patient cells, representing the formation of
239 mature autolysosomes and a high autophagy flux. In contrast, the ratio of green/red puncta and both
240 the number and size of double-positive puncta were increased in mutant cells, indicating impaired
241 autophagosome maturation into autolysosomes (Fig. 3F and S4D). Altogether, these results confirm
242 that autophagic flux is impaired in the mutant cells and further indicate that an autophagy imbalance
243 may contribute to metabolic and proteostatic stress in PI3K-Akt-mTORC1 activated cells.

244 Indeed, the network analysis of downregulated genes identified EIF2 and PTEN signalling as the top
245 downregulated pathways (Fig. 3B). PTEN is a negative regulator of the PI3K-Akt-mTORC1 axis.
246 Interestingly, inhibition of EIF2 signalling, a hub for the integrated stress response (ISR) and regulation

247 of protein translation under stress, in the m.3243A>G mutant cells indicated an attenuation of protein
248 synthesis and induction of ISR (Shpilka and Haynes, 2018; Suomalainen and Battersby, 2018). Analysis
249 of the individual transcripts from EIF2 signalling pathway showed a general downregulation of genes
250 involved in ribosomal biogenesis and upregulation of transcription factors – ATF4, ATF5 and DDIT3
251 (CHOP) (Fig. S4A; Table S2-3). ATF4 acts as a prototypical downstream target coupling mitochondrial
252 proteotoxic stress to the activation of ISR (Quirós et al., 2017). We therefore examined the protein
253 expression levels of these genes to demonstrate the activation of the ISR in patient-derived cells. A
254 significant increase in the phosphorylation levels of translation factor, eIF2α as well as the
255 downstream targets, ATF4, ATF5 and CHOP confirmed the induction of the ISR in the mutant cells (Fig.
256 3G and Fig. S4E).

257 To establish that the PI3K-Akt-mTORC1 axis is constitutively active in patients with the m.3243A>G
258 mtDNA mutation, we measured p-Akt/Akt and p-S6/S6 by immunofluorescence in a muscle biopsy
259 from a patient with an 82% mutant load of the m.3243A>G mutation causing MELAS, (not one of the
260 donors used to obtain the fibroblasts). A significant increase in p-Akt and p-S6 in the muscle biopsy
261 argues that upregulation of this pathway is a clinical feature of the disease and not a specific function
262 of the cultured cells (Fig. 3H). Re-analysis of a published RNA-seq data set (Deng et al., 2020) from
263 muscle biopsies of MELAS patients also confirmed alterations in cholesterol and serine biosynthesis
264 (Fig. 3I) and the activation of PI3K-Akt-mTORC1 signalling and induction of ISR in patients (Table S4).
265 Although activation of the ISR has been proposed to be cytoprotective and promote longevity (Gaude
266 et al., 2018; Molenaars et al., 2020), our data suggest that the activation of ISR in the context of the
267 m.3243A>G mtDNA mutation is not protective. Combined mitochondrial dysfunction, metabolic
268 remodelling and impaired autophagy may act as an overarching inducer of ISR in PI3K-Akt-mTORC1
269 activated m.3243A>G mutant cells (Mick et al., 2020).

270

271 **Pharmacological inhibition of PI3K-Akt-mTORC1 signalling reduces mutant load, resolves ISR,**
272 **rescues mitochondria function and lowers glucose dependence in the m.3243A>G mutant cells**

273 At this point, we asked what the functional consequences of the activation of the PI3K-Akt-mTORC1
274 axis are and whether it represents an adaptation to impaired OxPhos. We therefore systematically
275 inhibited each component of the axis in turn using well-established pharmacological inhibitors (Fig.
276 4A) (Manning and Toker, 2017) and explored the consequences for mutant mtDNA burden and the
277 pathophysiological and biochemical features that we have described above.

278 In both the fibroblasts from patient 1 and the cybrid cells, treatment with LY294002 (referred to below
279 as 'LY', 5 μM, an inhibitor of PI3K) or with rapamycin (referred to as 'RP', 5 μM, the canonical inhibitor

280 of mTORC1) led to a progressive decrease in mutant mtDNA load over 12 weeks of sustained
281 treatment (Fig. 4B). The efficacy of each drug as the inhibitor of the PI3K-Akt-mTORC1 axis was
282 confirmed by immunoblotting the downstream kinase targets, showing significant changes in
283 phosphorylated to unphosphorylated forms. Interestingly, in the absence of RP or LY, the fibroblasts
284 from patient 2 showed a progressive increase in mutant load with time in culture, rising from ~30% to
285 around 70% over 3 months (Fig. 4B). Treatment with the inhibitors significantly suppressed the rate
286 of increase in mutant load decreasing the total change by around 20%. Although the decrease in
287 mutant load took many weeks to develop, changes in protein phosphorylation state were evident
288 within a day of starting treatment (Fig. 4C and S5A). Accordingly, inhibition of PI3K by LY reduced p-
289 Akt/Akt ratio and mTOR phosphorylation, while rapamycin inhibited mTOR phosphorylation but had
290 no impact on Akt. None of the treatments had any immediate effect on AMPK phosphorylation.
291 However, AMPK activity gradually increased at later time points after drug treatments, suggesting an
292 induction of catabolic processes such as autophagy and improvement in sensing the bioenergetic
293 status of the m.3243A>G mutant cells (Garrido-Maraver et al., 2015). The ISR/UPR^{mt} pathway also
294 changed accordingly after the drug treatments (Fig. 4C and S5B), which restored the expression of
295 ATF4 and ATF5 to levels that were comparable to that of control. In LY-treated cells, ATF4 and ATF5
296 were downregulated almost immediately, while, interestingly, in RP-treated cells, ATF4 and ATF5 were
297 decreased after a week of treatment. These data confirmed that PI3K-Akt-mTORC1 axis is an upstream
298 regulator of ISR (Koromilas and Mounir, 2013; Suomalainen and Battersby, 2018), although the
299 mechanisms by which inhibition of mTORC1 or PI3K/Akt resolves the ISR may differ (Mick et al., 2020).

300 To investigate whether the decrease in mutant load and suppression of ISR after drug treatment were
301 reflected by a concomitant change in mitochondrial function, we measured the mitochondrial
302 bioenergetic status and the metabolic phenotype of the patient-derived cells. Measurements of
303 mitochondrial membrane potential showed a complete recovery to levels that were not significantly
304 different from control cells (Fig. 4D and S5C). These changes were accompanied by a decrease in the
305 fragmented phenotype in the mutant cells and a significant elongation and reformation of a
306 mitochondrial network (Fig. 4D and S4C). Measurements of mitochondrial respiration showed that
307 both basal and maximal respiratory capacity were increased in cells treated with LY or RP (Fig. 4E and
308 S5D). Treatment of mutant cells with MK2206 (MK, 1 μM), a pan Akt inhibitor, also caused a
309 progressive decrease in mutation load and restored mitochondrial function (Fig. S5E-I). We also
310 examined the effects of LY and RP in cells carrying another heteroplasmic mtDNA point mutation –
311 the m.8993T>G – generated by the Minczuk lab (Gaude et al., 2018). In these cells, inhibition of the
312 PI3K-Akt-mTORC1 axis had no impact on mutant load (Fig. S5J), suggesting that hyperactivation of the
313 PI3K-Akt-mTORC1 axis is relatively disease specific.

314 The improvement in mitochondrial respiration suggested a metabolic shift towards OxPhos.
315 Measurements of cytosolic redox state using SoNar (Fig. 4F and S5K) showed a significant reduction
316 in basal NADH:NAD^+ ratio and increased response to pyruvate addition in the long-term treated
317 patient-derived cells, implying a decreased glycolytic flux. Measurements of glucose and lactate
318 concentration in the media showed a profound decrease in lactate secretion following LY and RP
319 treatments (Fig 4G and S5L). The cells were also cultured in media containing glucose or galactose as
320 a primary carbon source to further assess their dependence on glycolysis. LY- and RP-treated cells, but
321 not mutant controls, grew well in the galactose media, indicating a reduced glycolytic dependence
322 after the drug treatments (Fig. 4H). Also, the mutant cells showed an increased supercomplex
323 formation as well as individual components of the mitochondrial ETC following drug treatments (Fig.
324 4I). In Gel activity assay for CI and CIII+CIV revealed a significant increase in enzyme activity of ETC in
325 response to the inhibitors (Fig. S5M). Further, the rates of ROS production were also reduced in cells
326 treated with LY and RP (Fig. 4J and S5N). Altogether, our results demonstrate that the long-term
327 treatment of the mutant cells with either LY or RP reverses the biochemical consequences of the
328 mutation, rescuing mitochondrial function, reducing glucose dependence and decreasing the
329 mutation load. These data strongly argue that the chronic activation of the PI3K-Akt-mTORC1 axis,
330 presumably as an adaptive response to impaired oxidative metabolism, instead serves as a
331 maladaptive response in this disease model.

332

333 **Reduction of the m.3243A>G mutant load by inhibition of the PI3K-Akt-mTORC1 axis is cell-**
334 **autonomous**

335 The chronic activation of the PI3K-Akt-mTORC1 axis and increased mutant load have deleterious
336 effects on cellular function and amplify the pathophysiological consequences of the mutation.
337 However, this raises questions about the underlying mechanism by which inhibition of the axis reduces
338 mutant load and rescues mitochondrial function. A possible explanation for the response to drug
339 treatments is that inhibition of the signalling pathway may promote the selective growth of cell
340 populations with low mutant load or selective elimination of cells with high mutant loads. We
341 therefore carried out long term measurements of growth rates and cell death (Fig. 5A, i and ii).
342 Although treatment with either LY or RP significantly slowed cell proliferation in both fibroblast and
343 cybrid cells (Fig. 5B, upper panel), the changes were small. The cell growth rate was stable in cybrid
344 cells treated with LY or RP, suggesting that there was no clonal expansion. In fibroblasts, growth rates
345 of cells were not altered by treatment with drugs for 4 or 8 weeks, while a significant decrease of
346 mutation load was clearly established after 4 weeks of treatment. This suggests that the change of
347 mutation load is independent of the rate of cell growth. Cell death rates in the drug-treated groups

348 were even lower than in the mutant controls, suggesting that the drug treatments were beneficial,
349 and there was no selective killing of mutant cells (Fig. 5B, lower panel). Treating the mutant cells with
350 MK showed similar results in terms of cell growth and death (Fig. S5A).

351 To determine definitively whether the reduction of mutant load in response to the drug treatments is
352 cell-autonomous, we used a PCR-based technique, TaqMan SNP genotyping, at single cell resolution
353 to measure the distributions of the m.3243A>G heteroplasmy in a cell population (Fig. 5Aiii). The
354 TaqMan technique was first validated by measuring the mutation loads of a population of cells and
355 then to establish the range of single cell mutant load across the population (Fig. S6B). The distribution
356 of mutant load in the cybrid cells ranged from 50-80%, showing a Gaussian distribution (Fig. S6C). The
357 average single cell mutant load was consistent with that of the whole cell population. Measurement
358 of the relative m.3243A>G heteroplasmy in patient fibroblasts and cybrid cells following treatment
359 with LY and RP for 6 and 12 weeks respectively showed a frequency distribution which clearly
360 segregated the treated group as a distinct population from the untreated group (Figs. 5C-D). The
361 distribution of the mutant load in treated groups, although showing stochastic variation within the
362 population, shifted to significantly lower levels compared to the untreated group. To determine
363 whether the reduction in the burden of the m.3243A>G heteroplasmy is also phenocopied at the
364 protein expression level, we immunostained the mtDNA-encoded cytochrome c oxidase I (MT-COI) in
365 patient 1 fibroblasts. The presence of 7 UUA-encoded leucine residues within MT-COI renders the
366 m.3243A>G $tRNA^{Leu(UUR)}$ cells prone to codon-specific translational defect (Janssen et al., 2007).
367 Immunofluorescence staining revealed a significant decrease in MT-COI expression in patient 1
368 fibroblasts compared to controls (Fig. S6D). Following drug treatments, these cells showed a partial
369 but significant recovery of MT-COI expression. The single cell analysis of MT-COI expression
370 segregated the drug-treated and untreated groups in a distribution pattern similar to the m.3243A>G
371 proportion in Fig. 5D. A diminished expression of MT-COI also correlated with the lower assembly and
372 activity of supercomplexes in Fig. 4I. Together, these results strongly suggest that rather than the
373 enrichment of a specific cell population, the reduction in m.3243A>G heteroplasmy caused by
374 inhibition of PI3K-Akt-mTORC1 signalling operates across the whole population and is likely cell-
375 autonomous.

376

377 **Restoration of autophagic/mitophagic flux by PI3K-Akt-mTORC1 inhibition is necessary to reduce**
378 **the m.3243A>G mutant load.**

379 Our results from the single cell analysis strongly argue that the change in heteroplasmy is a cell-
380 autonomous phenomenon. We then asked what mechanisms select against the mutant mtDNA. A

381 possible explanation could be the elimination of the mutant mtDNA by reducing the total mtDNA copy
382 number and then amplifying the dominant mtDNA, resembling 'the bottleneck' effect – the selection
383 mechanism of mtDNA in germline or embryo (Schon et al., 2012; Stewart and Chinnery, 2015). We
384 therefore quantified the total mtDNA copy number of the drug-treated cells at a series of time points,
385 but no significant changes were seen between the mutant control and drug-treated cells (Fig. S7A)
386 and the total mtDNA copy number remained stable across the duration of drug treatments.

387 It also seemed plausible that the removal of dysfunctional mitochondria via mitophagy may reduce
388 the mutant load in cells with the mtDNA mutation (Kandul et al., 2016; Suen et al., 2010). Indeed, long-
389 term treatment with either RP or LY significantly increased the conversion and accumulation of LC3BII
390 (autophagosome) in the presence of CQ compared to untreated cells (Fig. 6A and Fig. S7B). Notably,
391 the autophagic flux, evident by a high LC3BII/LC3BI ratio in the presence of CQ, increased progressively
392 with time closely mirroring the rate of decrease in mutant load (see Fig. 4B). Measurement of
393 autophagic flux using the mCherry-GFP-LC3 probe (Fig. 6B and Fig. S7C) showed a significant increase
394 in the formation of autolysosomes (red puncta) as early as 24 h of drug treatment and increased upon
395 long-term treatment in patient fibroblasts. Moreover, the ratio of green/red signal as well as the
396 average puncta size decreased significantly, suggesting the restoration of autophagy flux in the
397 m.3243A>G mutant cells after drug treatment.

398 To evaluate how the increased efficacy of autophagy affects mitophagy status, immunostaining of LC3
399 and cytochrome c was performed in the cybrid cells (Fig. S7D). The long-term drug treatment with RP
400 and LY dramatically increased the association between mitochondria and autophagosomes,
401 suggesting the restoration of mitophagy flux. To quantify mitochondrial degradation, we transfected
402 the cells with mitochondrial-targeted mKeima (mt-Keima, Addgene plasmid #56018), which
403 undergoes a spectral shift within acidic lysosomes. In control cells, the ratio of excitation (F_{543}/F_{458})
404 was high, demonstrating a differential distribution of intact (green) and degraded (red) mitochondria
405 (Fig. S7E), while in untreated patient fibroblasts, the fragmented mitochondrial network was evident,
406 and the proportion of high ratio (F_{543}/F_{458}) signal area to the total mitochondrial area was significantly
407 decreased, consistent with impaired mitophagic flux (Fig. 6C). However, after 24 h of drug treatments,
408 the (F_{543}/F_{458}) ratio increased with a concomitant increase in red puncta (degraded mitochondria) in
409 drug-treated patient fibroblasts. Altogether, these findings confirm that inhibition of PI3K-Akt-
410 mTORC1 signalling restores autophagy and promotes mitophagic flux in the m.3243A>G mutant cells

411 The progressive decrease in mutant load and increase in autophagic flux with time following PI3K-Akt-
412 mTORC1 inhibition in the m.3243A>G mutant cells strengthened the idea that upregulated mitophagic
413 flux drives selection against the mutant mtDNA and decreases the mutant load. To explore this further,
414 we quantified mitophagy in patient fibroblasts expressing mtKeima, cotreated with CQ in combination

415 with RP or LY. The cotreatment with CQ decreased the high ratio (F_{543}/F_{458}) signal to levels comparable
416 to untreated patient fibroblasts, indicating that the CQ treatment reversed the effect of LY and RP on
417 mitophagy (Fig. 6C). Remarkably, CQ treatment over 6 weeks in the patient fibroblasts and cybrid cells
418 also prevented the decrease of mutant load by PI3K-Akt-mTORC1 inhibition (Fig. 6D-E), strongly
419 suggesting that increased mitophagy is necessary to reduce the burden of mutant mtDNA. This also
420 argues strongly that the reduction in mutant load must be a cell-autonomous effect and cannot be
421 attributed to the selective growth of subpopulations of the cells. Together, effective
422 autophagy/mitophagy triggered by inhibition of the PI3K-Akt-mTORC1 axis is necessary to eliminate
423 the mutant m.3243A>G mtDNA.

424 **DISCUSSION**

425 The clinical presentation of disease caused by pathogenic mtDNA mutations is highly heterogeneous
426 (Schon et al., 2012; Stewart and Chinnery, 2015; Szczepanowska et al., 2012). The association between
427 specific mtDNA mutations, heteroplasmic mutant load, disease manifestation and severity are poorly
428 understood. In the present study, we have systematically characterised the metabolic and cell
429 signalling phenotype of cells bearing the m.3243A>G mutation, the most prevalent mtDNA mutation
430 which is responsible for mitochondrial encephalomyopathy, lactic acidosis and stroke like episodes
431 (MELAS) or Maternally inherited Diabetes and Deafness (MIDD) and related disorders. We found that
432 the changes in metabolism were associated with the constitutive hyperactivation of the PI3K-Akt-
433 mTORC1 pathway specifically associated with the m.3243A>G mtDNA mutation. Most notably,
434 pharmacological inhibition of PI3K, Akt, or mTORC1 in the patient-derived cells reduced mutant load
435 and rescued mitochondrial bioenergetic function. These inhibitors promoted the upregulation of
436 mitophagy, which was absolutely required to mediate the effects of these treatments (Fig. 6F). In
437 contrast to the m.3243A>G mtDNA variant, previous studies have reported downregulation of Akt
438 activity in cells carrying the m.8993T>G mutation (Wojewoda et al., 2011), in which inhibition of the
439 PI3K-Akt-mTORC1 pathway had no impact on mutant load or mitochondrial function (Fig. S5J). These
440 findings suggest that the changes in signalling pathways are disease specific and may represent a link
441 between genotype and phenotype.

442 Metabolic features of the patient fibroblasts and cybrid cells are consistent with most of the previous
443 studies of the m.3243A>G mutation, including mitochondrial dysfunction, upregulated glycolysis,
444 increased ROS production, and redox imbalance (de Andrade et al., 2006; Cotán et al., 2011; El-Hattab
445 et al., 2015; Garrido-Maraver et al., 2015; Janssen et al., 2007; Szczepanowska et al., 2012). However,
446 metabolic profiling of cells bearing the mutation is limited in the literature. Metabolomics data
447 showed that reductive carboxylation of glutamine is a major mechanism to support cell survival and
448 maintain redox balance in the m.8993T>G mutation cell models (Chen et al., 2018; Gaude et al., 2018).
449 In contrast, using a similar approach, we found that glucose anabolism (i.e. upregulated upper
450 glycolysis, PPP, and lipid synthesis) is increased in the m.3243A>G mutant cells and these cells are
451 dependent on glucose for cell survival and proliferation. Also, increased TCA cycle entry of pyruvate
452 through PC, which, combined with the prediction of enriched malate-aspartate shuttle pathway (Fig.
453 2A) may serve as a mechanism to maintain cellular $NADH/NAD^+$ balance to support glycolytic flux and
454 promote antioxidant capacity (Cappel et al., 2019; Gaude et al., 2018). This difference in metabolism
455 between the m.8993T>G and m.3243A>G mutations argues that the mtDNA mutations cannot be seen
456 as one disease (Mick et al., 2020; Raimundo et al., 2012). Thus, the rewired metabolism specific to the
457 m.3243A>G mutation drew our attention to the corresponding changes in cell signalling.

458 The alterations of metabolism in the m.3243A>G mutant cells strongly imply a perturbation in cell
459 signalling, especially implicating the PI3K-Akt-mTORC1 pathway, which has been widely studied in
460 cancer signalling and metabolism (Hoxhaj and Manning, 2020). For example, oxidative stress and
461 redox imbalance may activate PI3K-Akt, the increased glycolytic flux and PPP implies an activated Akt-
462 NRF2 signalling, the increased PC expression and p-PDH suggests an accumulation of acetyl-CoA
463 associated with Akt-mTORC1 activity, and the accumulation of cholesteryl ester can result from
464 excessive lysosomal free cholesterol, which also activates mTORC1 (Castellano et al., 2017; Hoxhaj and
465 Manning, 2020). Metabolic pathway analysis using RNA-seq data recapitulated these metabolic
466 changes in the patient fibroblasts. Moreover, network analysis using the RNA-seq data further
467 validated the link between the metabolic changes and altered cell signalling in cells carrying the
468 m.3243A>G mutation. In addition, defective autophagy, because of chronic activation of the PI3K-Akt-
469 mTORC1 pathway, may impair the selective degradation of lipid droplets (lipophagy) and contribute
470 to the accumulation of lipid droplets in the m.3243A>G mutant cells. Sphingomyelin accumulation, as
471 one of the features of the lipidomic data, may damage lysosomes, also contributing to impaired
472 autophagy (Deus et al., 2020; Yambire et al., 2019).

473 Although the mechanisms of crosstalk between PI3K-Akt-mTORC1 and EIF2 pathways are still unclear,
474 these two pathways seem to communicate and determine cell fate under stress (Koromilas and
475 Mounir, 2013; Suomalainen and Battersby, 2018). Of note, the ISR/UPR^{mt} mediated by the EIF2
476 signalling was also downregulated by pharmacological inhibition of the PI3K-Akt-mTORC1 axis in the
477 mutant cells. Given that the UPR^{mt} maintains mutant mtDNA in a *C. elegans* mtDNA disease model (Lin
478 et al., 2016) and recent studies reported that OMA1 is responsible for eIF2α phosphorylation under
479 acute mitochondrial stress (Fessler et al., 2020; Guo et al., 2020), exploring the role of ISR/UPR^{mt} in
480 the maintenance of the m.3243A>G mutation and disease progression by suppressing eIF2α
481 phosphorylation will be interesting. Furthermore, in a published RNA-seq data set of muscle biopsies
482 from patients with MELAS (Deng et al., 2020), FGF21 (~48 fold) and GDF15 (~9 fold) were upregulated,
483 matching previous findings reported from muscle tissue of 'Deletor' mice (Khan et al., 2017). In
484 contrast, in the present study, while we did not find changes in these two genes in the patient
485 fibroblasts, we did find upregulation of FGF16 (~33 fold), suggesting that changes in FGF pathways in
486 response to mitochondrial dysfunction might be tissue specific.

487 Previous studies have suggested that different levels of heteroplasmy of the m.3243A>G mutation in
488 cybrid cells result in different gene expression patterns and even in discrete changes in metabolism
489 (McMillan et al., 2019; Picard et al., 2014). Another study showed that JNK was activated by ROS in
490 cybrid m.3243A>G cells, further reducing RXRA expression (Chae et al., 2013). In contrast, our data did
491 not show inhibition of the RXRA pathway and suggest that chronic activation of the PI3K-Akt-mTORC1

492 pathway is a general response in cells with the m.3243A>G mutation despite very different levels of
493 mutant load. Remarkably, we found that prolonged treatment with inhibitors of each component of
494 the PI3K-Akt-mTORC1 axis reliably and reproducibly reduced mutant burden and rescued
495 mitochondrial function in the mutant cells. Although inhibition of PI3K-Akt-mTORC1 axis has been
496 shown to be beneficial in several mitochondrial and neurological disease models, the underlying
497 mechanisms remain elusive (Civiletto et al., 2018; Deus et al., 2020; Haroon et al., 2018; Manning and
498 Toker, 2017; Zheng et al., 2016). As a result, the therapeutic efficacy of the inhibition may be distinct
499 and limited in different models. A study of a mouse model of Leigh syndrome showed that rapamycin,
500 while delaying the progression of the disease, failed to improve OxPhos (Johnson et al., 2013).
501 Similarly, another study showed that mTORC1 inhibition failed to improve either mitochondrial
502 bioenergetics or survival in a mouse model of mitochondrial encephalomyopathy ($Coq9^{R239X}$)
503 (Barriocanal-Casado et al., 2019). Our data from cells with the m.8993T>G mutation suggest that
504 changes in signalling pathways may differ between mtDNA diseases, perhaps pointing towards the
505 mechanisms that define differences in disease phenotype between different mitochondrial diseases,
506 and emphasising that therapeutic options should be considered separately for each disease related to
507 mtDNA mutations. However, since both the PI3K-Akt-mTORC1 axis and the accumulation of mtDNA
508 mutations have been associated with neurodegeneration, ageing and cancers, our study may
509 implicate in a broader biomedical context (Hoxhaj and Manning, 2020; Kotiadis et al., 2014; Manning
510 and Toker, 2017; Schon et al., 2012; Stewart and Chinnery, 2015).

511 Overall, the m.3243A>G mutation causes a profound cell metabolic and signalling remodelling,
512 although the causality between the observed alterations in metabolism and ell signalling of the
513 m.3243A>G mutant cells is not yet conclusive. Our working model is that activation of the PI3K-Akt-
514 mTORC1 pathway drives a metabolic rewiring of the cell, redirecting glycolytic metabolism and
515 promoting lactate production. Activating mTORC1 suppresses mitophagy, allowing the mutation to
516 propagate and thus maintaining the mutant load. Inhibition of the PI3K-Akt-mTORC1 axis promotes
517 mitophagy, reduces mutant load and improves bioenergetic competence in a cell-autonomous way.
518 Thus, we propose that nutrient-sensing pathways that may have evolved as adaptive responses to
519 altered cellular metabolism prove to be maladaptive, driving a positive feedback cycle that may shape
520 the phenotype of the disease and determine disease progression. In conclusion, our results suggest
521 that activation of the PI3K-Akt-mTORC1 axis by changes in intermediary metabolism controls the
522 heteroplasmic burden of the m.3243A>G mutation and may define disease progression and severity
523 in a cell-autonomous manner. These data strongly suggest that cell signalling pathways activated by
524 altered metabolism represent potential therapeutic targets that may benefit people suffering from
525 diseases caused by mtDNA mutations.

Figure 1

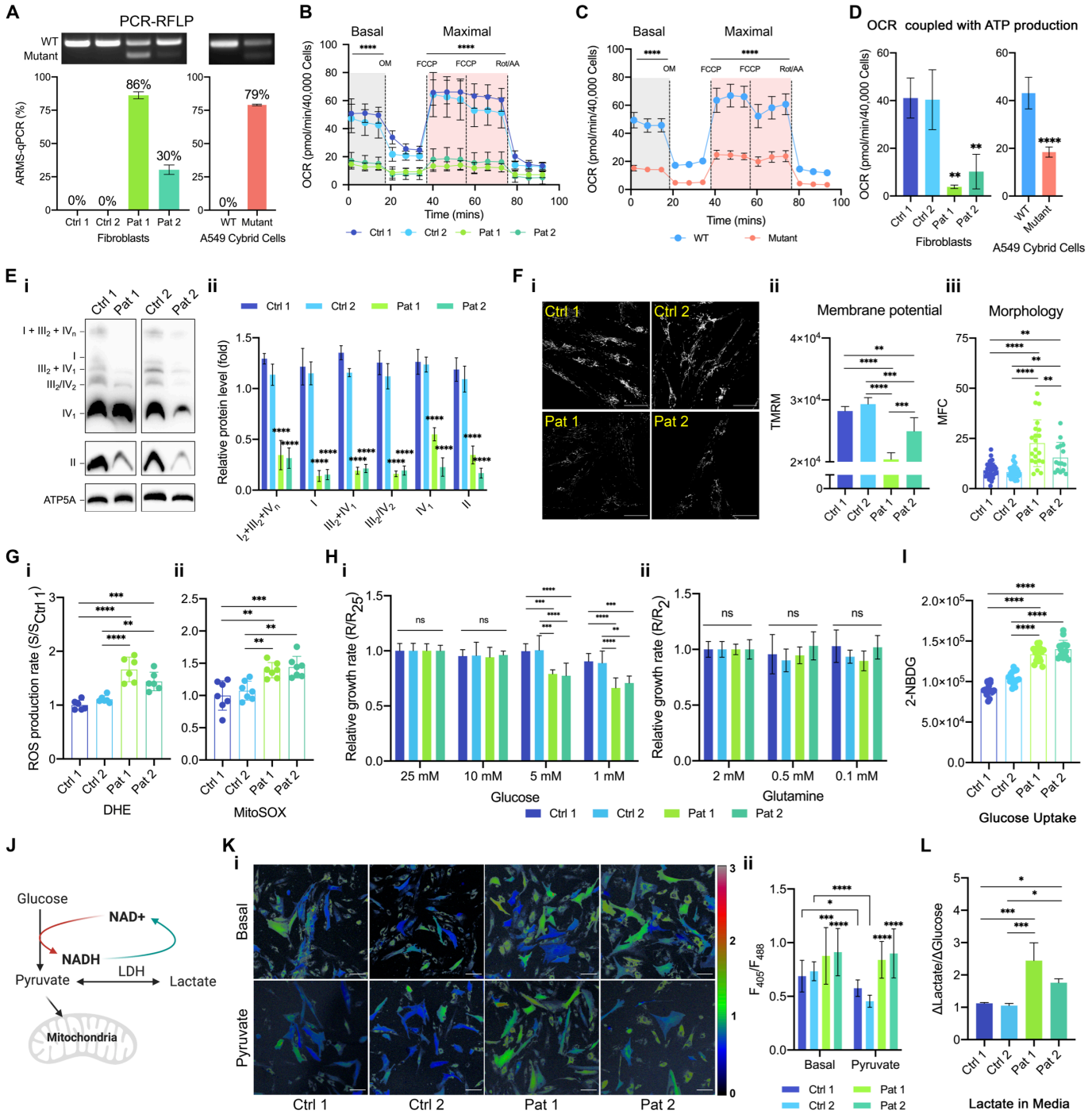
A
PCR-RFLP
WT
Mutant
ARMS-qPCR (%)
86%
30%
79%
0%
Ctrl 1
Ctrl 2
Pat 1
Pat 2
Fibroblasts
WT
Mutant
A549 Cybrid Cells
B
Basal
Maximal
OM
FCCP
Rot/AA
OCR (pmol/min/40,000 Cells)
Time (mins)
C
D
OCR coupled with ATP production
E
i
ii
Relative protein level (fold)
ATP5A
F
Membrane potential
Morphology
TMRM
MFC
G
ROS production rate (S/S$_{Ctrl 1}$)
DHE
MitoSOX
H
Relative growth rate (R/R$_{25}$)
Relative growth rate (R/R$_2$)
25 mM
10 mM
5 mM
1 mM
Glucose
2 mM
0.5 mM
0.1 mM
Glutamine
ns
I
2-NBDG
Glucose Uptake
J
Glucose
NAD+
NADH
LDH
Pyruvate
Lactate
Mitochondria
K
Basal
Pyruvate
F$_{405}$/F$_{488}$
L
ΔLactate/ΔGlucose
Lactate in Media

Figure S1

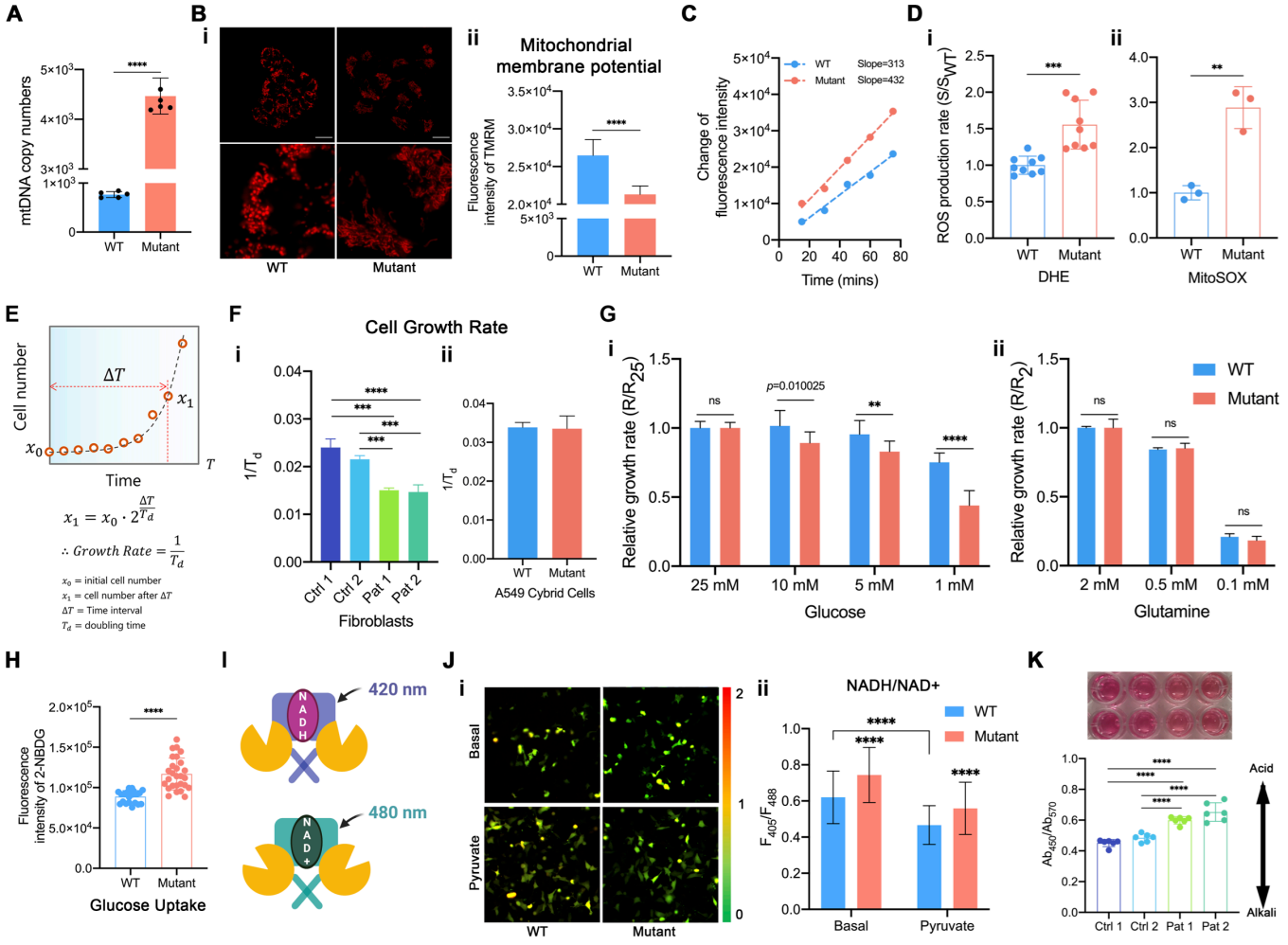
A
mtDNA copy numbers
WT
Mutant
B
i
WT
Mutant
ii
Mitochondrial membrane potential
Fluorescence intensity of TMRM
C
Change of fluorescence intensity
WT Slope=313
Mutant Slope=432
Time (mins)
D
i
ROS production rate (S/S_WT)
DHE
ii
MitoSOX
E
Cell number
Time
ΔT
x_0
x_1
T
x_1 = x_0 · 2^(ΔT/T_d)
∴ Growth Rate = 1/T_d
x_0 = initial cell number
x_1 = cell number after ΔT
ΔT = Time interval
T_d = doubling time
F
Cell Growth Rate
i
1/T_d
Ctrl 1
Ctrl 2
Pat 1
Pat 2
Fibroblasts
ii
A549 Cybrid Cells
G
i
Relative growth rate (R/R_25)
p=0.010025
25 mM
10 mM
5 mM
1 mM
Glucose
ii
Relative growth rate (R/R_2)
WT
Mutant
2 mM
0.5 mM
0.1 mM
Glutamine
H
Fluorescence intensity of 2-NBDG
Glucose Uptake
I
420 nm
480 nm
NADH
NAD+
J
i
Basal
Pyruvate
WT
Mutant
ii
NADH/NAD+
F_405/F_488
K
Acid
Alkali
Ab_450/Ab_570
Ctrl 1
Ctrl 2
Pat 1
Pat 2

Figure 2

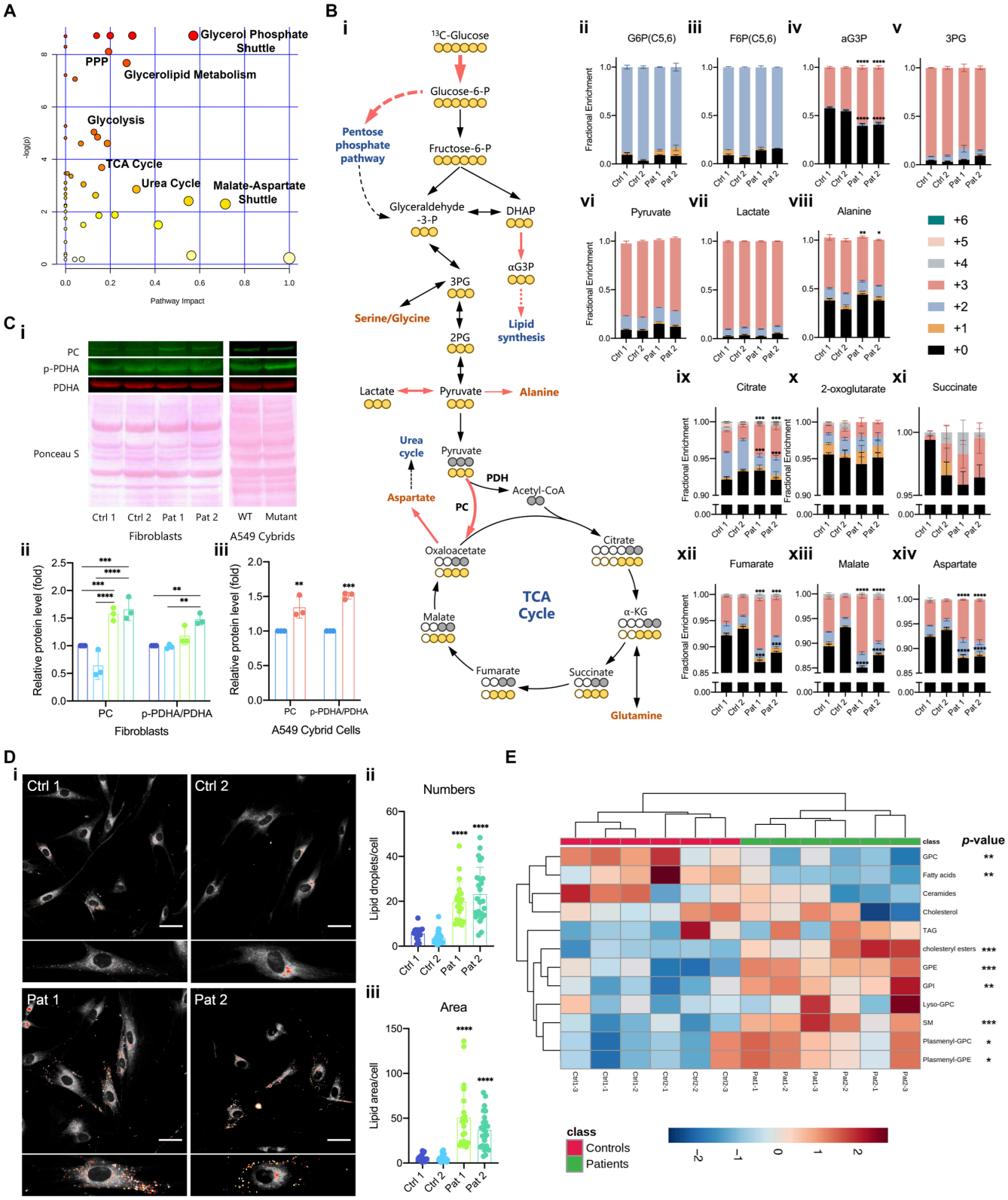
A
Glycerol Phosphate Shuttle
PPP
Glycerolipid Metabolism
Glycolysis
TCA Cycle
Urea Cycle
Malate-Aspartate Shuttle
-log(p)
Pathway Impact
B
i
13C-Glucose
Glucose-6-P
Pentose phosphate pathway
Fructose-6-P
Glyceraldehyde -3-P
DHAP
αG3P
3PG
Serine/Glycine
Lipid synthesis
2PG
Lactate
Pyruvate
Alanine
Urea cycle
Pyruvate
PDH
Acetyl-CoA
Aspartate
PC
Oxaloacetate
Citrate
TCA Cycle
Malate
α-KG
Fumarate
Succinate
Glutamine
ii G6P(C5,6)
iii F6P(C5,6)
iv aG3P
v 3PG
vi Pyruvate
vii Lactate
viii Alanine
ix Citrate
x 2-oxoglutarate
xi Succinate
xii Fumarate
xiii Malate
xiv Aspartate
Fractional Enrichment
Ctrl 1
Ctrl 2
Pat 1
Pat 2
+6
+5
+4
+3
+2
+1
+0
C
i
PC
p-PDHA
PDHA
Ponceau S
Ctrl 1
Ctrl 2
Pat 1
Pat 2
WT
Mutant
Fibroblasts
A549 Cybrids
ii
Relative protein level (fold)
PC
p-PDHA/PDHA
Fibroblasts
iii
Relative protein level (fold)
PC
p-PDHA/PDHA
A549 Cybrid Cells
D
i
Ctrl 1
Ctrl 2
Pat 1
Pat 2
ii
Numbers
Lipid droplets/cell
iii
Area
Lipid area/cell
E
class
p-value
GPC
Fatty acids
Ceramides
Cholesterol
TAG
cholesteryl esters
GPE
GPI
Lyso-GPC
SM
Plasmenyl-GPC
Plasmenyl-GPE
Ctrl-3
Ctrl-1
Ctrl-2
Ctrl2-1
Ctrl2-2
Ctrl2-3
Pat1-1
Pat1-2
Pat1-3
Pat2-2
Pat2-1
Pat2-3
class
Controls
Patients

Figure S2

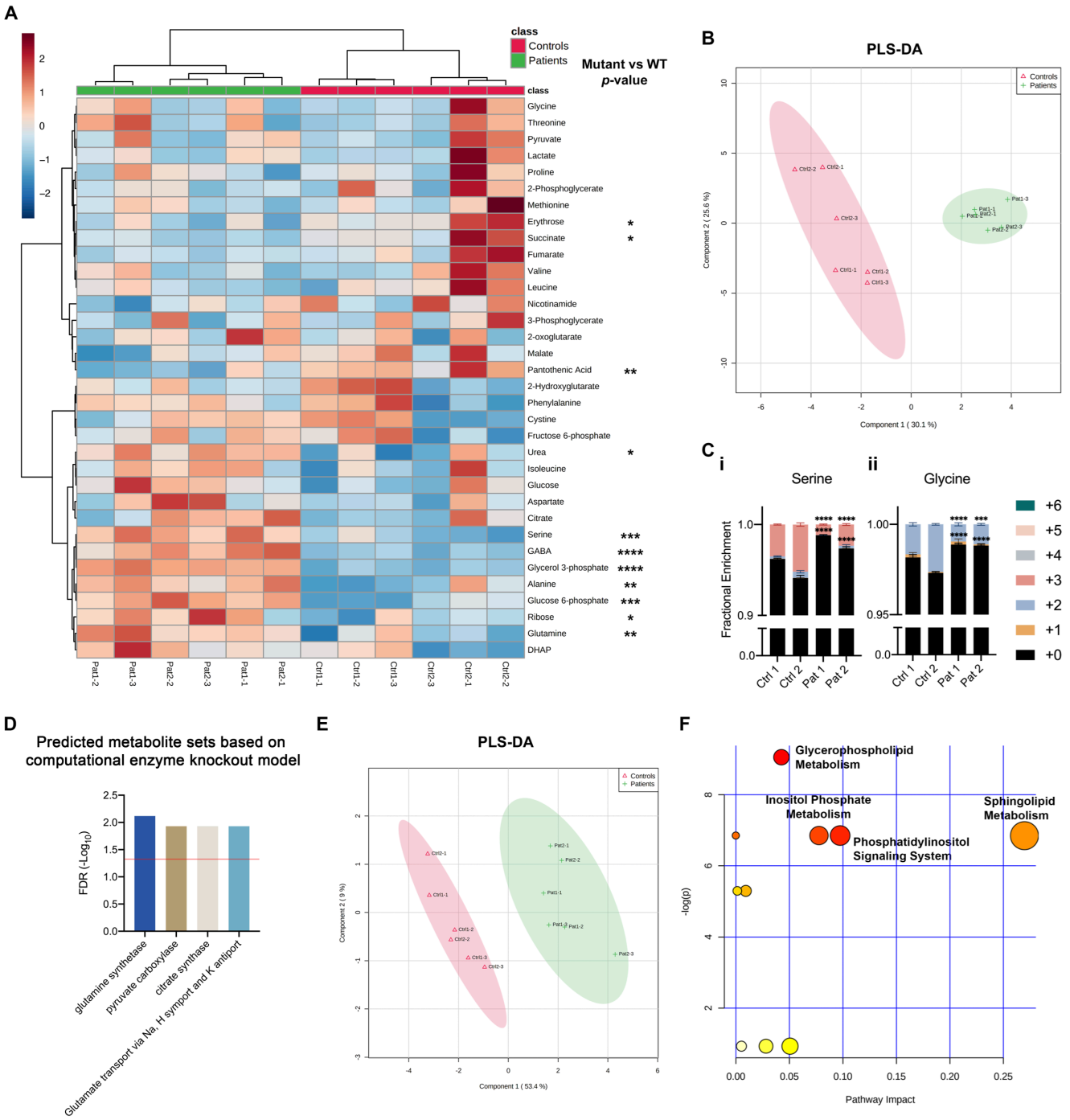
A
class
Controls
Patients
Mutant vs WT
p-value
Glycine
Threonine
Pyruvate
Lactate
Proline
2-Phosphoglycerate
Methionine
Erythrose *
Succinate *
Fumarate
Valine
Leucine
Nicotinamide
3-Phosphoglycerate
2-oxoglutarate
Malate
Pantothenic Acid **
2-Hydroxyglutarate
Phenylalanine
Cystine
Fructose 6-phosphate
Urea *
Isoleucine
Glucose
Aspartate
Citrate
Serine ***
GABA ****
Glycerol 3-phosphate ****
Alanine **
Glucose 6-phosphate ***
Ribose *
Glutamine **
DHAP
Pat1-2
Pat1-3
Pat2-2
Pat2-3
Pat1-1
Pat2-1
Ctrl1-1
Ctrl1-2
Ctrl1-3
Ctrl2-3
Ctrl2-1
Ctrl2-2
B
PLS-DA
Controls
Patients
Component 1 (30.1 %)
Component 2 (25.6 %)
C
i
Serine
ii
Glycine
Fractional Enrichment
Ctrl 1
Ctrl 2
Pat 1
Pat 2
+6
+5
+4
+3
+2
+1
+0
D
Predicted metabolite sets based on computational enzyme knockout model
FDR (-Log10)
glutamine synthetase
pyruvate carboxylase
citrate synthase
Glutamate transport via Na, H symport and K antiport
E
PLS-DA
Controls
Patients
Component 1 (53.4 %)
Component 2 (9 %)
F
Glycerophospholipid Metabolism
Inositol Phosphate Metabolism
Sphingolipid Metabolism
Phosphatidylinositol Signaling System
-log(p)
Pathway Impact

Figure 3

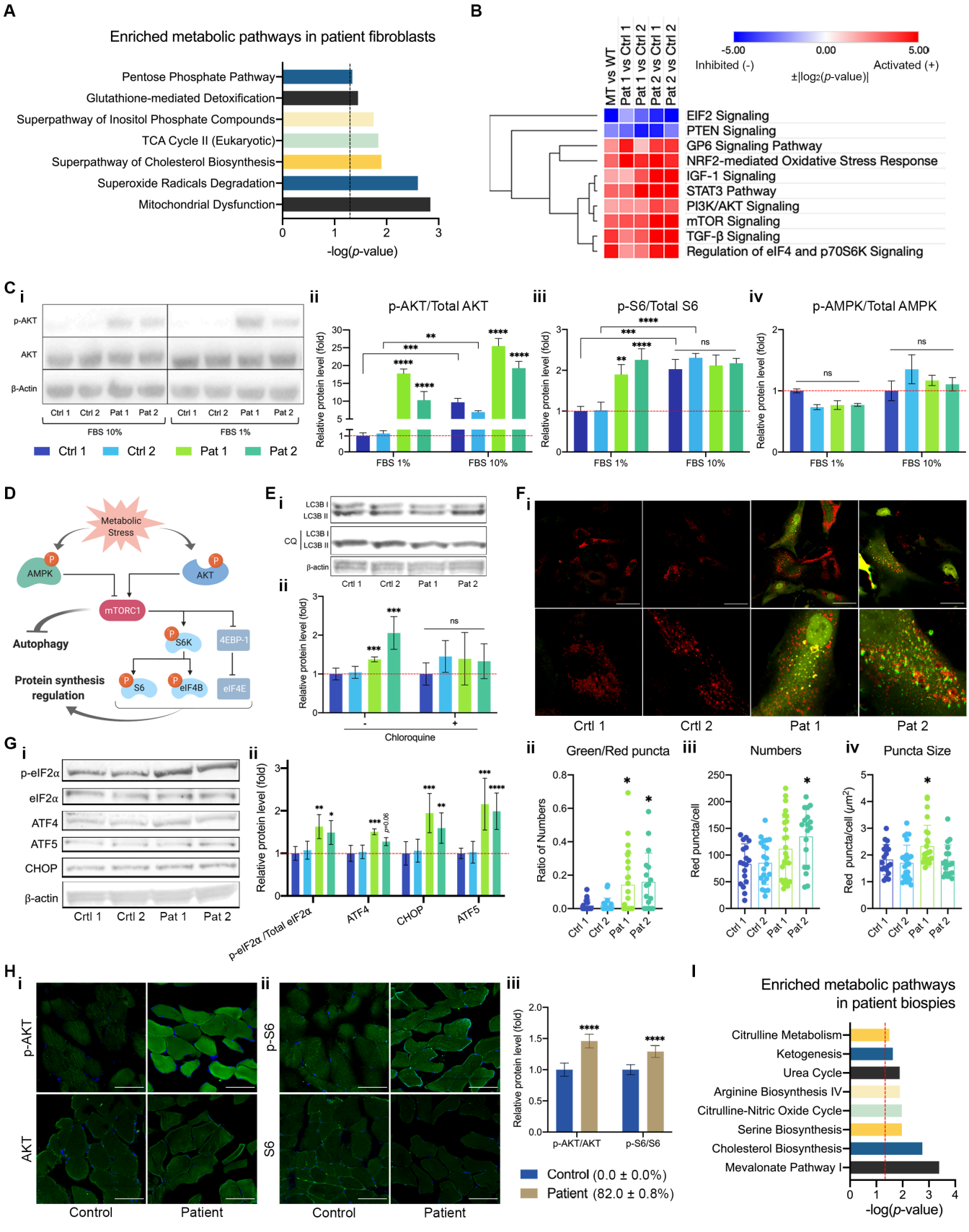
A
Enriched metabolic pathways in patient fibroblasts
Pentose Phosphate Pathway
Glutathione-mediated Detoxification
Superpathway of Inositol Phosphate Compounds
TCA Cycle II (Eukaryotic)
Superpathway of Cholesterol Biosynthesis
Superoxide Radicals Degradation
Mitochondrial Dysfunction
-log(p-value)
B
MT vs WT
Pat 1 vs Ctrl 1
Pat 1 vs Ctrl 2
Pat 2 vs Ctrl 1
Pat 2 vs Ctrl 2
-5.00
0.00
5.00
Inhibited (-)
Activated (+)
±|log2(p-value)|
EIF2 Signaling
PTEN Signaling
GP6 Signaling Pathway
NRF2-mediated Oxidative Stress Response
IGF-1 Signaling
STAT3 Pathway
PI3K/AKT Signaling
mTOR Signaling
TGF-β Signaling
Regulation of eIF4 and p70S6K Signaling
C
p-AKT
AKT
β-Actin
Ctrl 1
Ctrl 2
Pat 1
Pat 2
FBS 10%
FBS 1%
p-AKT/Total AKT
p-S6/Total S6
p-AMPK/Total AMPK
Relative protein level (fold)
ns
D
Metabolic Stress
AMPK
AKT
mTORC1
Autophagy
S6K
4EBP-1
Protein synthesis regulation
S6
eIF4B
eIF4E
E
LC3B I
LC3B II
CQ
β-actin
Chloroquine
F
Green/Red puncta
Numbers
Puncta Size
Ratio of Numbers
Red puncta/cell
Red puncta/cell (μm²)
G
p-eIF2α
eIF2α
ATF4
ATF5
CHOP
p-eIF2α /Total eIF2α
H
p-AKT
AKT
p-S6
S6
Control
Patient
p-AKT/AKT
p-S6/S6
Control (0.0 ± 0.0%)
Patient (82.0 ± 0.8%)
I
Enriched metabolic pathways in patient biospies
Citrulline Metabolism
Ketogenesis
Urea Cycle
Arginine Biosynthesis IV
Citrulline-Nitric Oxide Cycle
Serine Biosynthesis
Cholesterol Biosynthesis
Mevalonate Pathway I
-log(p-value)

Figure S3

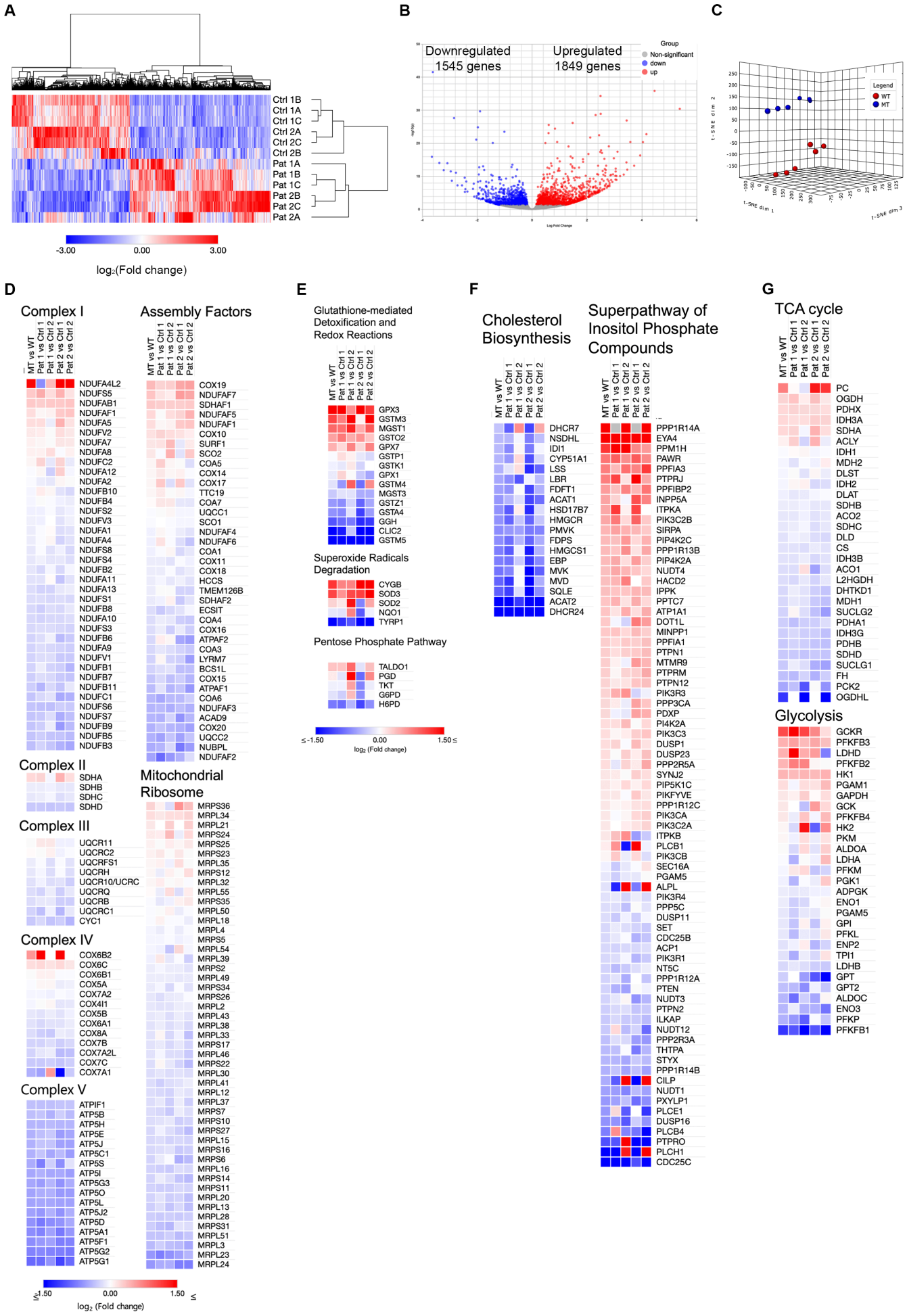
A
Ctrl 1B
Ctrl 1A
Ctrl 1C
Ctrl 2A
Ctrl 2C
Ctrl 2B
Pat 1A
Pat 1B
Pat 1C
Pat 2B
Pat 2C
Pat 2A
-3.00
0.00
3.00
log2(Fold change)
B
Downregulated
1545 genes
Upregulated
1849 genes
Group
Non-significant
down
up
C
Legend
WT
MT
D
Complex I
Assembly Factors
MT vs WT
Pat 1 vs Ctrl 1
Pat 1 vs Ctrl 2
Pat 2 vs Ctrl 1
Pat 2 vs Ctrl 2
NDUFA4L2
NDUFS5
NDUFAB1
NDUFAF1
NDUFA5
NDUFV2
NDUFA7
NDUFA8
NDUFC2
NDUFA12
NDUFA2
NDUFB10
NDUFB4
NDUFS2
NDUFV3
NDUFA1
NDUFA4
NDUFS8
NDUFS4
NDUFB2
NDUFA11
NDUFA13
NDUFS1
NDUFB8
NDUFA10
NDUFS3
NDUFB6
NDUFA9
NDUFV1
NDUFB1
NDUFB7
NDUFB11
NDUFC1
NDUFS6
NDUFS7
NDUFB9
NDUFB5
NDUFB3
COX19
NDUFAF7
SDHAF1
NDUFAF5
NDUFAF1
COX10
SURF1
SCO2
COA5
COX14
COX17
TTC19
COA7
UQCC1
SCO1
NDUFAF4
NDUFAF6
COA1
COX11
COX18
HCCS
TMEM126B
SDHAF2
ECSIT
COA4
COX16
ATPAF2
COA3
LYRM7
BCS1L
COX15
ATPAF1
COA6
NDUFAF3
ACAD9
COX20
UQCC2
NUBPL
NDUFAF2
Complex II
SDHA
SDHB
SDHC
SDHD
Mitochondrial Ribosome
MRPS36
MRPL34
MRPL21
MRPS24
MRPS25
MRPS23
MRPL35
MRPS12
MRPL32
MRPL55
MRPS35
MRPL50
MRPL18
MRPL4
MRPS5
MRPL54
MRPL39
MRPS2
MRPL49
MRPS34
MRPS26
MRPL2
MRPL43
MRPL38
MRPL33
MRPS17
MRPL46
MRPS22
MRPL30
MRPL41
MRPL12
MRPL37
MRPS7
MRPS10
MRPS27
MRPL15
MRPS16
MRPS6
MRPL16
MRPS14
MRPS11
MRPL20
MRPL13
MRPL28
MRPS31
MRPL51
MRPL3
MRPL23
MRPL24
Complex III
UQCR11
UQCRC2
UQCRFS1
UQCRH
UQCR10/UCRC
UQCRQ
UQCRB
UQCRC1
CYC1
Complex IV
COX6B2
COX6C
COX6B1
COX5A
COX7A2
COX4I1
COX5B
COX6A1
COX8A
COX7B
COX7A2L
COX7C
COX7A1
Complex V
ATPIF1
ATP5B
ATP5H
ATP5E
ATP5J
ATP5C1
ATP5S
ATP5I
ATP5G3
ATP5O
ATP5L
ATP5J2
ATP5D
ATP5A1
ATP5F1
ATP5G2
ATP5G1
≤-1.50
0.00
1.50 ≤
log2 (Fold change)
E
Glutathione-mediated Detoxification and Redox Reactions
GPX3
GSTM3
MGST1
GSTO2
GPX7
GSTP1
GSTK1
GPX1
GSTM4
MGST3
GSTZ1
GSTA4
GGH
CLIC2
GSTM5
Superoxide Radicals Degradation
CYGB
SOD3
SOD2
NQO1
TYRP1
Pentose Phosphate Pathway
TALDO1
PGD
TKT
G6PD
H6PD
≤-1.50
0.00
1.50 ≤
log2 (Fold change)
F
Cholesterol Biosynthesis
DHCR7
NSDHL
IDI1
CYP51A1
LSS
LBR
FDFT1
ACAT1
HSD17B7
HMGCR
PMVK
FDPS
HMGCS1
EBP
MVK
MVD
SQLE
ACAT2
DHCR24
Superpathway of Inositol Phosphate Compounds
PPP1R14A
EYA4
PPM1H
PAWR
PPFIA3
PTPRJ
PPFIBP2
INPP5A
ITPKA
PIK3C2B
SIRPA
PIP4K2C
PPP1R13B
PIP4K2A
NUDT4
HACD2
IPPK
PPTC7
ATP1A1
DOT1L
MINPP1
PPFIA1
PTPN1
MTMR9
PTPRM
PTPN12
PIK3R3
PPP3CA
PDXP
PI4K2A
PIK3C3
DUSP1
DUSP23
PPP2R5A
SYNJ2
PIP5K1C
PIKFYVE
PPP1R12C
PIK3CA
PIK3C2A
ITPKB
PLCB1
PIK3CB
SEC16A
PGAM5
ALPL
PIK3R4
PPP5C
DUSP11
SET
CDC25B
ACP1
PIK3R1
NT5C
PPP1R12A
PTEN
NUDT3
PTPN2
ILKAP
NUDT12
PPP2R3A
THTPA
STYX
PPP1R14B
CILP
NUDT1
PXYLP1
PLCE1
DUSP16
PLCB4
PTPRO
PLCH1
CDC25C
G
TCA cycle
PC
OGDH
PDHX
IDH3A
SDHA
ACLY
IDH1
MDH2
DLST
IDH2
DLAT
SDHB
ACO2
SDHC
DLD
CS
IDH3B
ACO1
L2HGDH
DHTKD1
MDH1
SUCLG2
PDHA1
IDH3G
PDHB
SDHD
SUCLG1
FH
PCK2
OGDHL
Glycolysis
GCKR
PFKFB3
LDHD
PFKFB2
HK1
PGAM1
GAPDH
GCK
PFKFB4
HK2
PKM
ALDOA
LDHA
PFKM
PGK1
ADPGK
ENO1
PGAM5
GPI
PFKL
ENP2
TPI1
LDHB
GPT
GPT2
ALDOC
ENO3
PFKP
PFKFB1

Figure S4

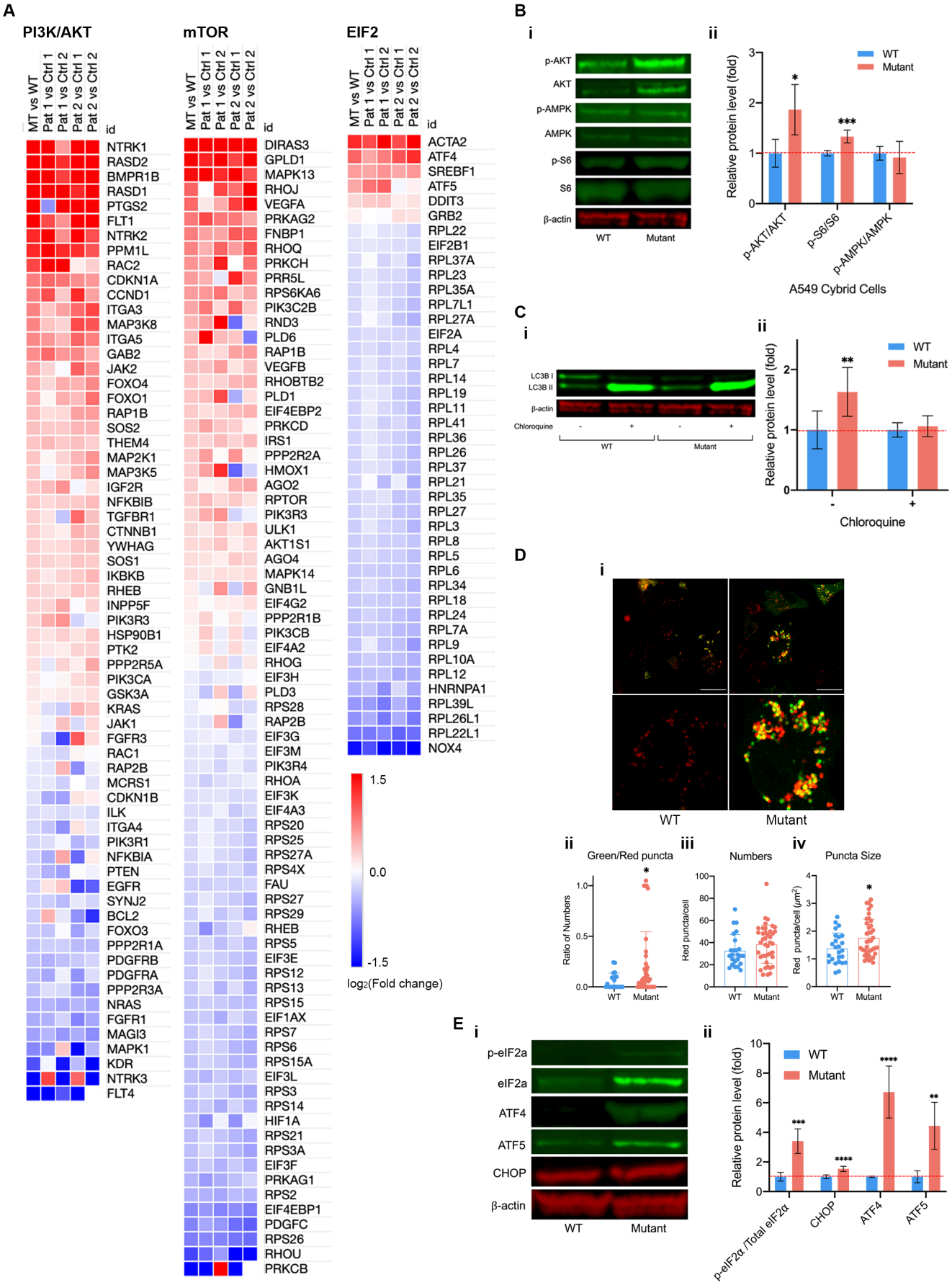
A
PI3K/AKT
mTOR
EIF2
MT vs WT
Pat 1 vs Ctrl 1
Pat 1 vs Ctrl 2
Pat 2 vs Ctrl 1
Pat 2 vs Ctrl 2
id
NTRK1
RASD2
BMPR1B
RASD1
PTGS2
FLT1
NTRK2
PPM1L
RAC2
CDKN1A
CCND1
ITGA3
MAP3K8
ITGA5
GAB2
JAK2
FOXO4
FOXO1
RAP1B
SOS2
THEM4
MAP2K1
MAP3K5
IGF2R
NFKBIB
TGFBR1
CTNNB1
YWHAG
SOS1
IKBKB
RHEB
INPP5F
PIK3R3
HSP90B1
PTK2
PPP2R5A
PIK3CA
GSK3A
KRAS
JAK1
FGFR3
RAC1
RAP2B
MCRS1
CDKN1B
ILK
ITGA4
PIK3R1
NFKBIA
PTEN
EGFR
SYNJ2
BCL2
FOXO3
PPP2R1A
PDGFRB
PDGFRA
PPP2R3A
NRAS
FGFR1
MAGI3
MAPK1
KDR
NTRK3
FLT4
DIRAS3
GPLD1
MAPK13
RHOJ
VEGFA
PRKAG2
FNBP1
RHOQ
PRKCH
PRR5L
RPS6KA6
PIK3C2B
RND3
PLD6
RAP1B
VEGFB
RHOBTB2
PLD1
EIF4EBP2
PRKCD
IRS1
PPP2R2A
HMOX1
AGO2
RPTOR
PIK3R3
ULK1
AKT1S1
AGO4
MAPK14
GNB1L
EIF4G2
PPP2R1B
PIK3CB
EIF4A2
RHOG
EIF3H
PLD3
RPS28
RAP2B
EIF3G
EIF3M
PIK3R4
RHOA
EIF3K
EIF4A3
RPS20
RPS25
RPS27A
RPS4X
FAU
RPS27
RPS29
RHEB
RPS5
EIF3E
RPS12
RPS13
RPS15
EIF1AX
RPS7
RPS6
RPS15A
EIF3L
RPS3
RPS14
HIF1A
RPS21
RPS3A
EIF3F
PRKAG1
RPS2
EIF4EBP1
PDGFC
RPS26
RHOU
PRKCB
ACTA2
ATF4
SREBF1
ATF5
DDIT3
GRB2
RPL22
EIF2B1
RPL37A
RPL23
RPL35A
RPL7L1
RPL27A
EIF2A
RPL4
RPL7
RPL14
RPL19
RPL11
RPL41
RPL36
RPL26
RPL37
RPL21
RPL35
RPL27
RPL3
RPL8
RPL5
RPL6
RPL34
RPL18
RPL24
RPL7A
RPL9
RPL10A
RPL12
HNRNPA1
RPL39L
RPL26L1
RPL22L1
NOX4
1.5
0.0
-1.5
log2(Fold change)
B
i
p-AKT
AKT
p-AMPK
AMPK
p-S6
S6
β-actin
WT
Mutant
ii
WT
Mutant
Relative protein level (fold)
p-AKT/AKT
p-S6/S6
p-AMPK/AMPK
A549 Cybrid Cells
C
i
LC3B I
LC3B II
β-actin
Chloroquine
WT
Mutant
ii
WT
Mutant
Relative protein level (fold)
Chloroquine
D
i
WT
Mutant
ii
Green/Red puncta
Ratio of Numbers
iii
Numbers
Red puncta/cell
iv
Puncta Size
Red puncta/cell (μm²)
E
i
p-eIF2a
eIF2a
ATF4
ATF5
CHOP
β-actin
WT
Mutant
ii
WT
Mutant
Relative protein level (fold)
p-eIF2α /Total eIF2α
CHOP
ATF4
ATF5

Table S1-4

Table S1. Upstream analysis for Kinase in patient fibroblasts by IPA.

Kinase	Prediction	Z-score	*p*-value
CDKN1A	Activated	3.084	1.12E-08
IKBKB		3.244	0.000377
AKT1		2.47	0.00201
MAPK13		2.079	0.00245
TGFBR2		2.747	0.00255
PTK2		2.48	0.00302
CHUK		4.427	0.00929
STK11	Inhibited	-2.494	0.00000766
INSR		-2.032	0.000675
CCNK		-2.399	0.000866
AURKB		-2.772	0.005

Table S2. Upstream analysis for translation regulator in patient fibroblasts by IPA.

Translation regulator	Prediction	Z-score	*p*-value
EIF4E	Inhibited	-2.169	0.000541
EIF4G1		-2.333	0.00245

Table S3. Upstream analysis for transcription regulators in patient fibroblasts by IPA.

Transcription regulator	Prediction	Z-score	*p*-value
TP53	Activated	3.282	2.79E-21
NUPR1		4.066	5.29E-11
KDM5B		3.627	0.00000101
CTNNB1		2.96	0.00000321
NFKBIA		2.632	0.0000157
GLI1		2.971	0.0000256
TCF4		2.225	0.0000457
SMARCA4		3.609	0.000108
KLF4		2.946	0.000627
PTTG1		2.302	0.000791
TFEB		3.273	0.0008
CDKN2A		4.62	0.000838
TCF7L2		4.059	0.000841
TCF3		3.926	0.00118
HIF1A		2.117	0.00224
CREB1		3.164	0.00238
HDAC1		2.228	0.00248
RBCK1		2.236	0.00252
E2F6		2.53	0.00259
ATF4		2.495	0.00296
SMARCD3		2.813	0.005
HDAC2		2.468	0.00621
ERG		2.557	0.00988
EP300		2.298	0.00994
TBX2	Inhibited	-4.488	2.43E-08
MYC		-4.01	2.46E-07
MYCN		-5.406	0.00000442
GMNN		-2.746	0.0000098
SOX1		-3	0.0000215
HOXA9		-2.01	0.0000273
E2F3		-3.186	0.0000273
SOX3		-3	0.00012
RUNX3		-2.272	0.000213

Table S4. Upstream analysis using published RNA-seq dataset of patient biopsies by IPA.

Upstream Regulator	Molecule Type	*p*-value
TRIB3	Kinase	0.0000295
MTOR		0.00112
TGFBR2		0.0101
GNE		0.0155
PIK3R1		0.0159
TGFBR1		0.0166
CDK19		0.0199
Growth hormone	Group	0.000165
Foxo		0.000504
ADRB		0.00393
Insulin		0.00402
YAP/TAZ		0.0089
Pro-inflammatory Cytokine		0.0101
PI3K (family)		0.026
Rxr		0.0269
ATF4	Transcription Regulator	0.00048
MLX		0.000905
PPARGC1A		0.00115
EP300		0.0029
FOXO1		0.00299
MLXIPL		0.00326
MLXIP		0.00446
ZNF282		0.0089
MYRF		0.0104
HDAC5		0.0122
NKX2-3		0.0127
MYC		0.0131
STAT6		0.0149
ZNF100		0.0155
ZNF85		0.0155
ZNF254		0.0155
ZNF431		0.0155
ZNF43		0.0155
ZNF429		0.0155
HDAC10		0.0177
ZNF91		0.0177
ATF5		0.0221
PA2G4		0.0221
KAT5		0.0231
STAT5B		0.026
AJUBA		0.0265
DDIT3		0.0282
BHLHE41		0.0287
ARNT		0.0304
PIAS4		0.0308
THRAP3		0.033
PLAGL1		0.033
KLF11		0.0337
CREBZF		0.0352
CBX4		0.0352
TCF7L2		0.0374
MNT		0.0416
ACTN4		0.0416
CREB3L3		0.0438
NONO		0.0438
MED12		0.0459
SIN3B		0.0459
PBX3		0.048
HNF4A		0.048
MED1		0.0492

Figure 4

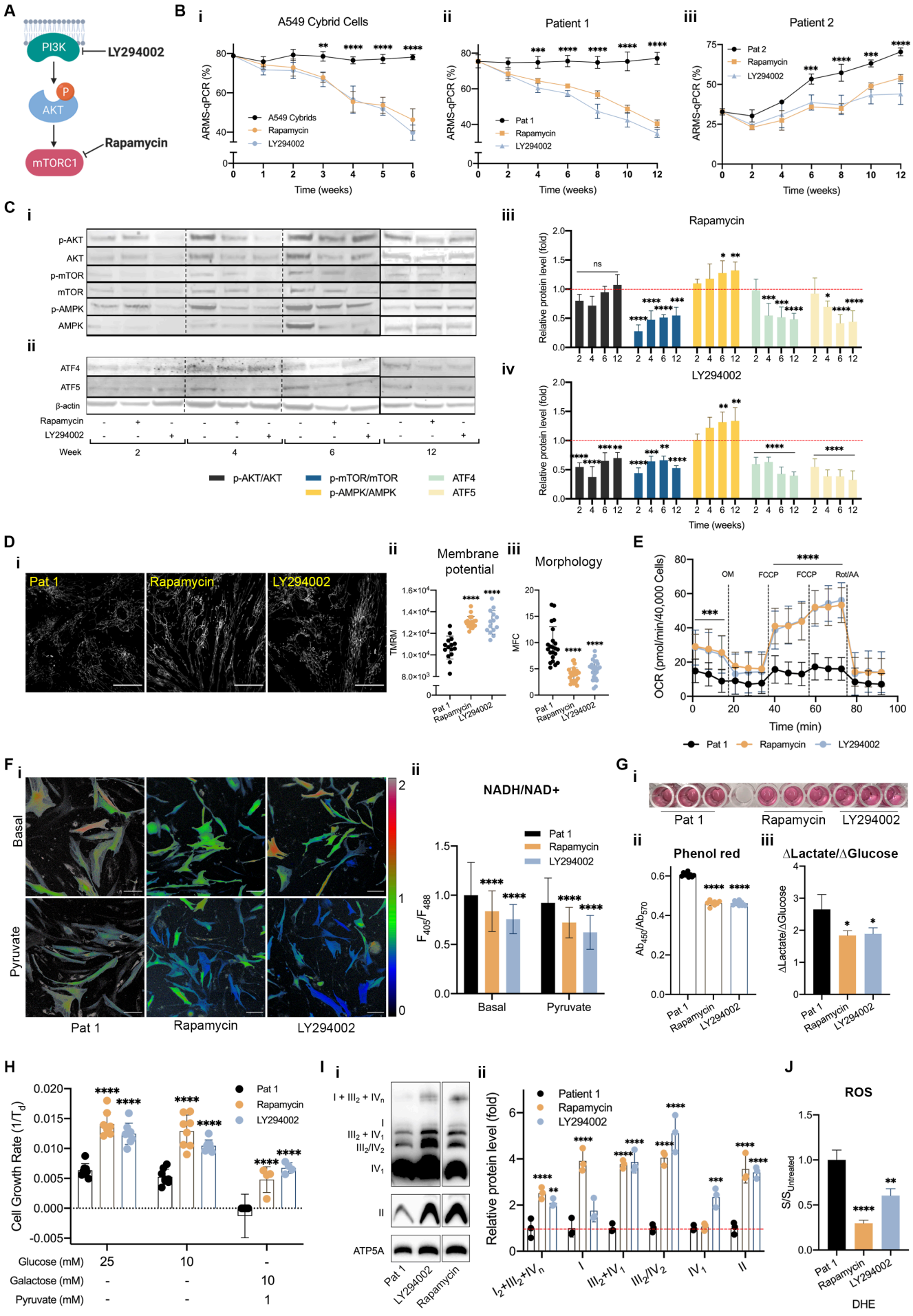
A
PI3K
LY294002
P
AKT
Rapamycin
mTORC1
B
i
A549 Cybrid Cells
ARMS-qPCR (%)
A549 Cybrids
Rapamycin
LY294002
Time (weeks)
ii
Patient 1
Pat 1
iii
Patient 2
Pat 2
C
i
p-AKT
AKT
p-mTOR
mTOR
p-AMPK
AMPK
ii
ATF4
ATF5
β-actin
Rapamycin
LY294002
Week
p-AKT/AKT
p-mTOR/mTOR
p-AMPK/AMPK
ATF4
ATF5
iii
Rapamycin
Relative protein level (fold)
ns
iv
LY294002
Time (weeks)
D
i
Pat 1
Rapamycin
LY294002
ii
Membrane potential
TMRM
iii
Morphology
MFC
E
OCR (pmol/min/40,000 Cells)
OM
FCCP
FCCP
Rot/AA
Time (min)
Pat 1
Rapamycin
LY294002
F
i
Basal
Pyruvate
Pat 1
Rapamycin
LY294002
ii
NADH/NAD+
Pat 1
Rapamycin
LY294002
Basal
Pyruvate
G
i
Pat 1
Rapamycin
LY294002
ii
Phenol red
iii
ΔLactate/ΔGlucose
H
Cell Growth Rate (1/T_d)
Pat 1
Rapamycin
LY294002
Glucose (mM)
Galactose (mM)
Pyruvate (mM)
I
i
I + III2 + IVn
I
III2 + IV1
III2/IV2
IV1
II
ATP5A
Pat 1
LY294002
Rapamycin
ii
Patient 1
Rapamycin
LY294002
Relative protein level (fold)
J
ROS
S/S_Untreated
Pat 1
Rapamycin
LY294002
DHE

Figure S5

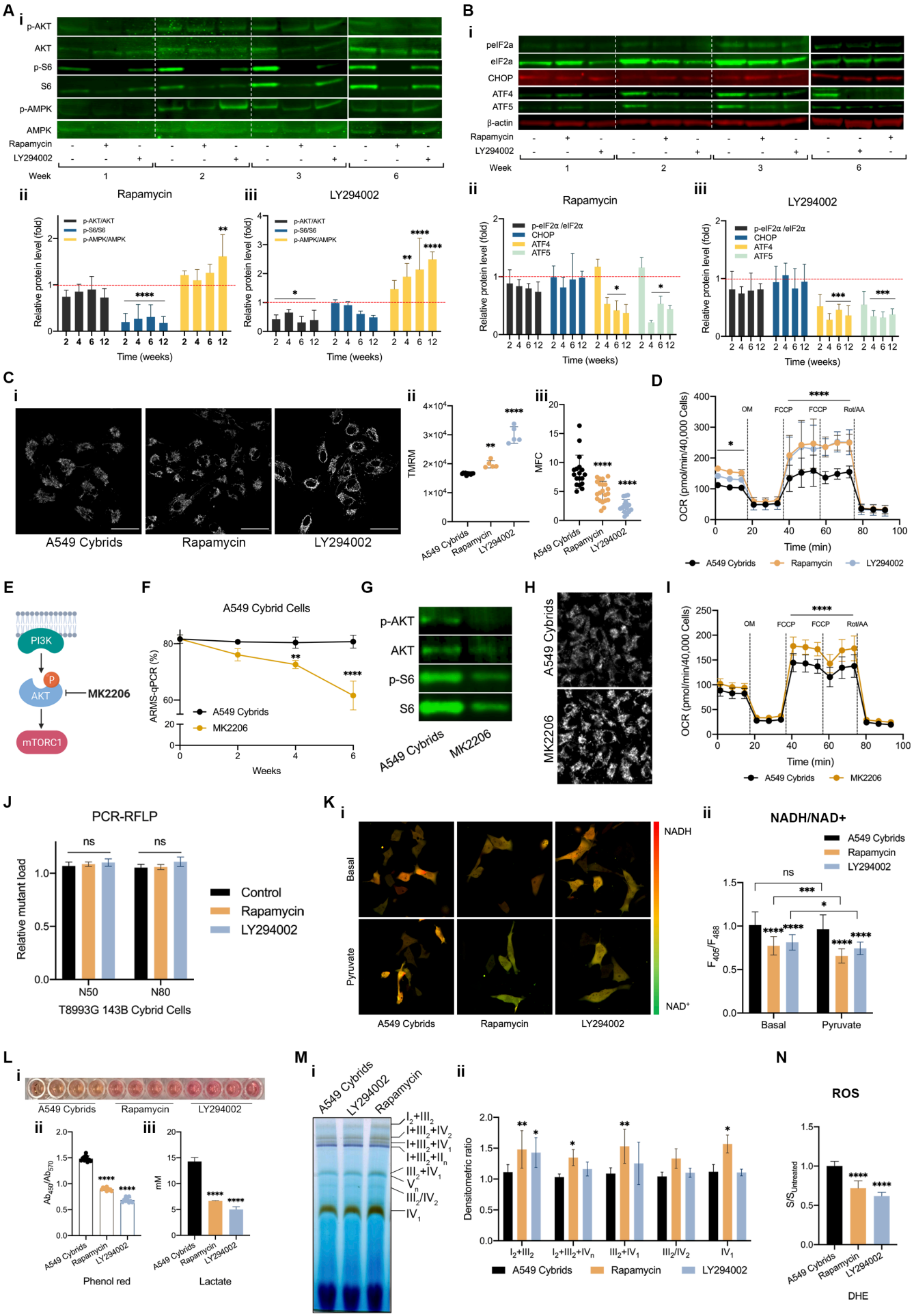
A
i
p-AKT
AKT
p-S6
S6
p-AMPK
AMPK
Rapamycin
LY294002
Week
1
2
3
6
ii
Rapamycin
iii
LY294002
p-AKT/AKT
p-S6/S6
p-AMPK/AMPK
Relative protein level (fold)
Time (weeks)
B
i
peIF2a
eIF2a
CHOP
ATF4
ATF5
β-actin
p-eIF2α /eIF2α
C
A549 Cybrids
Rapamycin
LY294002
TMRM
MFC
D
OCR (pmol/min/40,000 Cells)
OM
FCCP
Rot/AA
Time (min)
E
PI3K
AKT
mTORC1
MK2206
F
A549 Cybrid Cells
ARMS-qPCR (%)
Weeks
MK2206
G
p-AKT
AKT
p-S6
S6
H
I
J
PCR-RFLP
Relative mutant load
Control
N50
N80
T8993G 143B Cybrid Cells
K
NADH
NAD+
Basal
Pyruvate
NADH/NAD+
L
Phenol red
Lactate
M
I2+III2
I+III2+IV2
I+III2+IV1
I+III2+IIn
III2+IV1
Vn
III2/IV2
IV1
Densitometric ratio
N
ROS
DHE

Figure 5

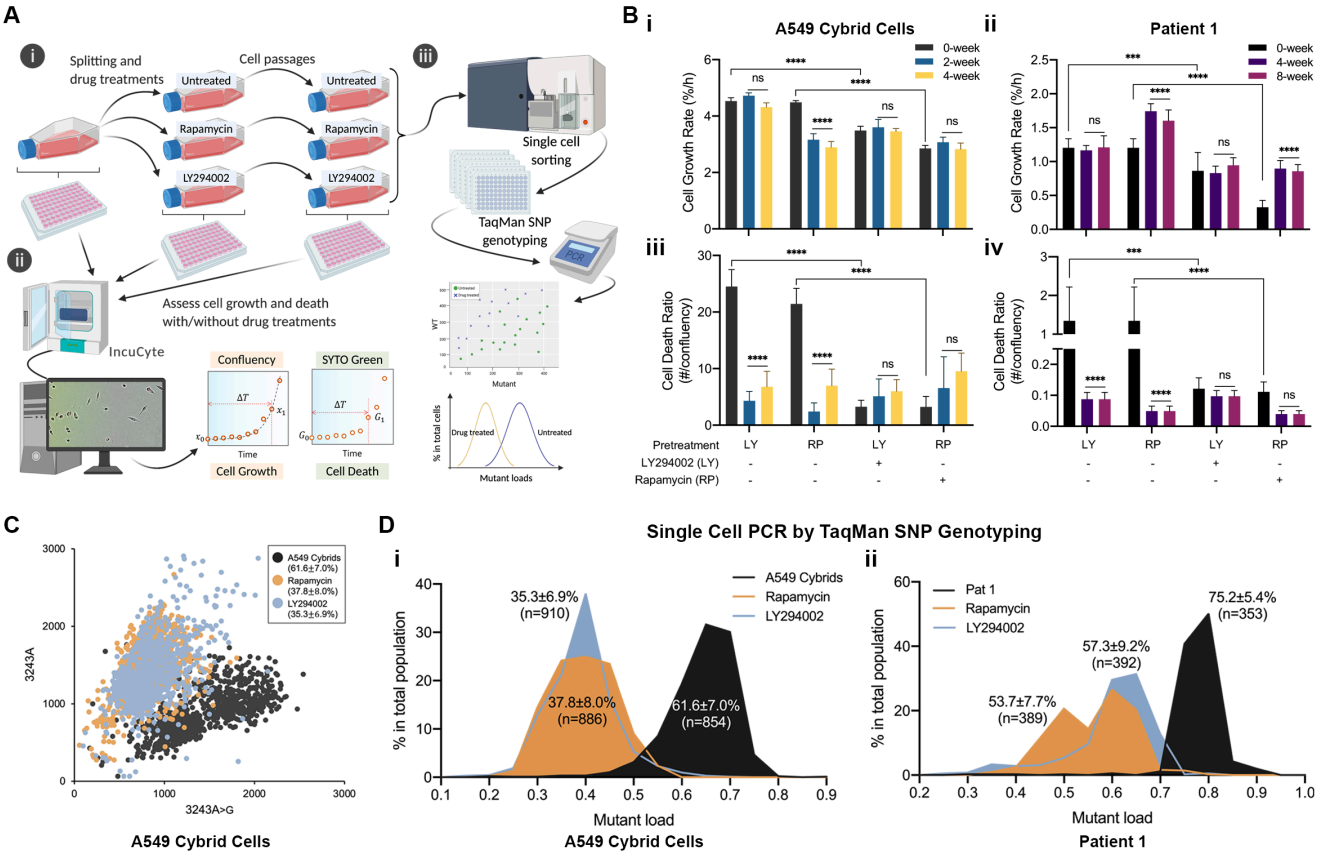
A
i
Splitting and drug treatments
Cell passages
Untreated
Rapamycin
LY294002
iii
Single cell sorting
TaqMan SNP genotyping
ii
Assess cell growth and death with/without drug treatments
IncuCyte
Confluency
SYTO Green
Time
Cell Growth
Cell Death
Mutant
Mutant loads
Drug treated
Untreated
B
i
A549 Cybrid Cells
0-week
2-week
4-week
Cell Growth Rate (%/h)
ii
Patient 1
0-week
4-week
8-week
iii
Cell Death Ratio (#/confluency)
iv
Pretreatment
LY294002 (LY)
Rapamycin (RP)
LY
RP
C
A549 Cybrids (61.6±7.0%)
Rapamycin (37.8±8.0%)
LY294002 (35.3±6.9%)
3243A
3243A>G
A549 Cybrid Cells
D
Single Cell PCR by TaqMan SNP Genotyping
i
A549 Cybrids
Rapamycin
LY294002
35.3±6.9% (n=910)
37.8±8.0% (n=886)
61.6±7.0% (n=854)
% in total population
Mutant load
A549 Cybrid Cells
ii
Pat 1
Rapamycin
LY294002
75.2±5.4% (n=353)
57.3±9.2% (n=392)
53.7±7.7% (n=389)
Patient 1

Figure S6

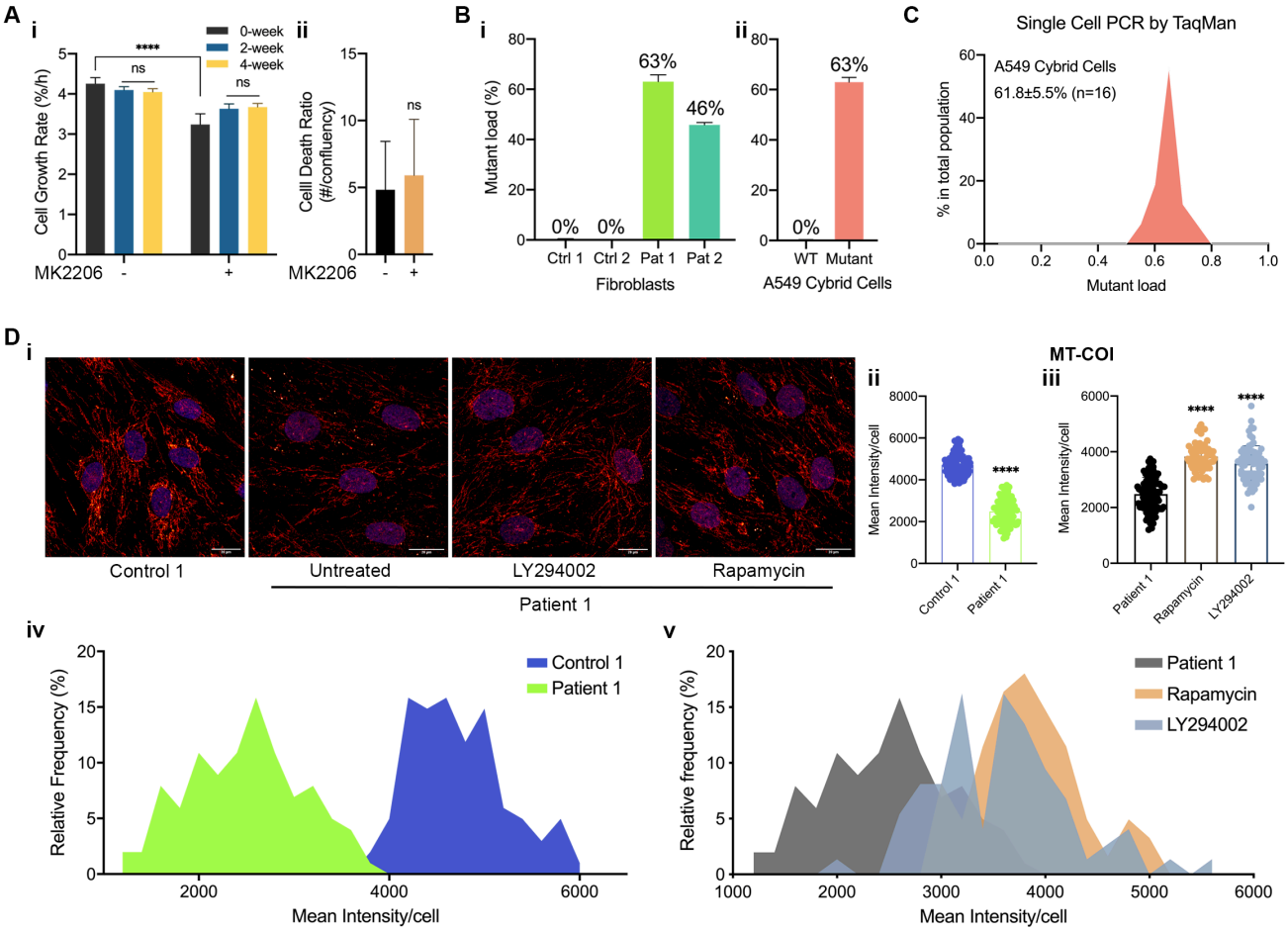
A
i
0-week
2-week
4-week
****
ns
ns
Cell Growth Rate (%/h)
MK2206
-
+
ii
Celll Death Ratio (#/confluency)
ns
MK2206
-
+
B
i
Mutant load (%)
0%
0%
63%
46%
Ctrl 1
Ctrl 2
Pat 1
Pat 2
Fibroblasts
ii
63%
0%
WT
Mutant
A549 Cybrid Cells
C
Single Cell PCR by TaqMan
A549 Cybrid Cells
61.8±5.5% (n=16)
% in total population
Mutant load
D
i
Control 1
Untreated
LY294002
Rapamycin
Patient 1
ii
Mean Intensity/cell
****
Control 1
Patient 1
MT-COI
iii
Mean Intensity/cell
****
****
Patient 1
Rapamycin
LY294002
iv
Relative Frequency (%)
Control 1
Patient 1
Mean Intensity/cell
v
Relative frequency (%)
Patient 1
Rapamycin
LY294002
Mean Intensity/cell

Figure 6

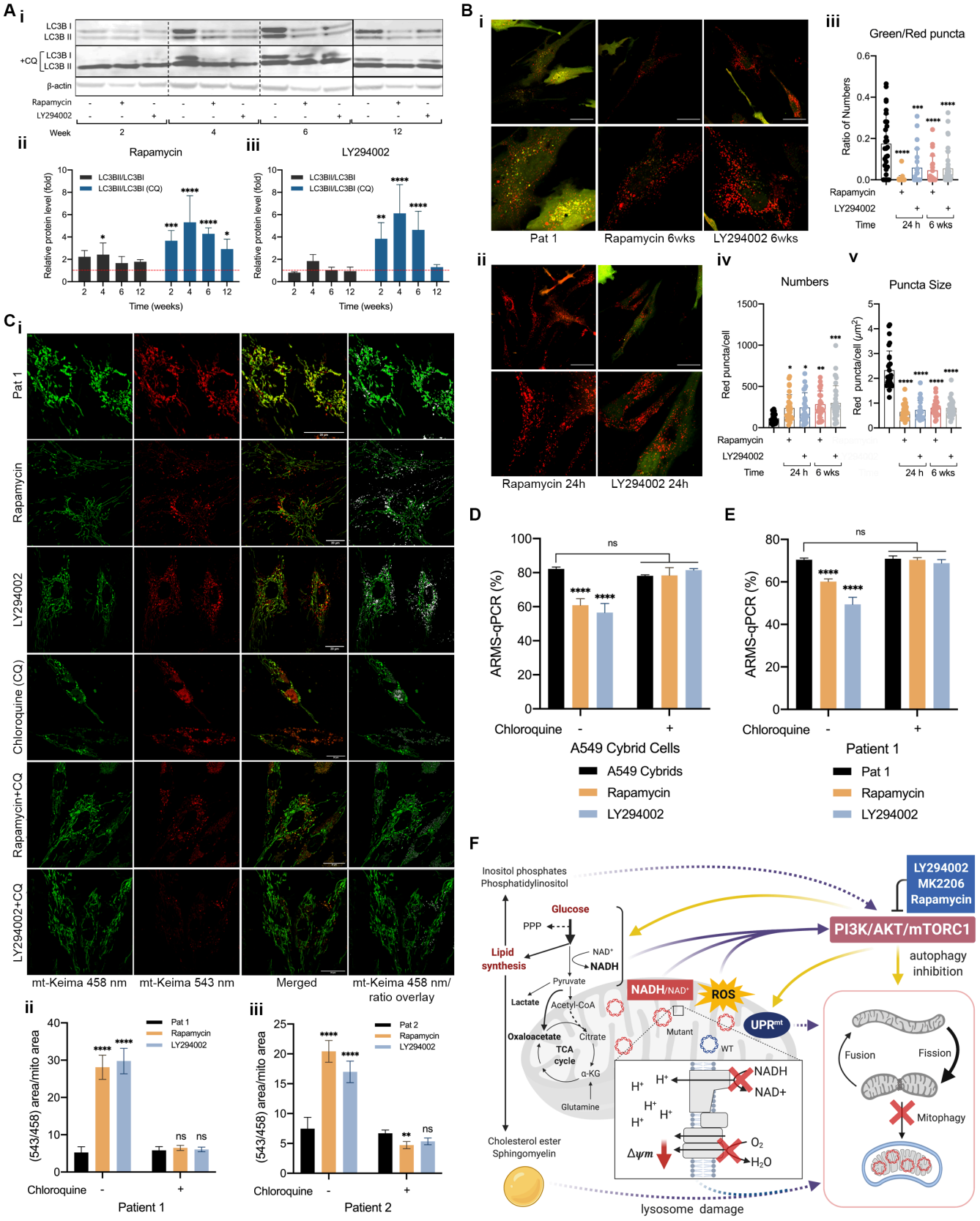
A
i
LC3B I
LC3B II
+CQ
β-actin
Rapamycin
LY294002
Week
ii
Rapamycin
iii
LY294002
LC3BII/LC3BI
LC3BII/LC3BI (CQ)
Relative protein level (fold)
Time (weeks)
B
i
Pat 1
Rapamycin 6wks
LY294002 6wks
ii
Rapamycin 24h
LY294002 24h
iii
Green/Red puncta
Ratio of Numbers
Time
24 h
6 wks
iv
Numbers
Red puncta/cell
v
Puncta Size
Red puncta/cell (μm²)
C
i
Pat 1
Rapamycin
LY294002
Chloroquine (CQ)
Rapamycin+CQ
LY294002+CQ
mt-Keima 458 nm
mt-Keima 543 nm
Merged
mt-Keima 458 nm/ ratio overlay
ii
Pat 1
Rapamycin
LY294002
(543/458) area/mito area
Chloroquine
Patient 1
iii
Pat 2
Rapamycin
LY294002
Patient 2
D
ARMS-qPCR (%)
ns
Chloroquine
A549 Cybrid Cells
A549 Cybrids
Rapamycin
LY294002
E
Patient 1
Pat 1
F
Inositol phosphates
Phosphatidylinositol
Glucose
PPP
Lipid synthesis
NAD+
NADH
Pyruvate
Lactate
Acetyl-CoA
Oxaloacetate
Citrate
TCA cycle
α-KG
Glutamine
Cholesterol ester
Sphingomyelin
NADH/NAD+
ROS
Mutant
WT
UPRmt
LY294002
MK2206
Rapamycin
PI3K/AKT/mTORC1
autophagy inhibition
Fusion
Fission
Mitophagy
NADH
NAD+
O2
H2O
Δψm
lysosome damage

Figure S7

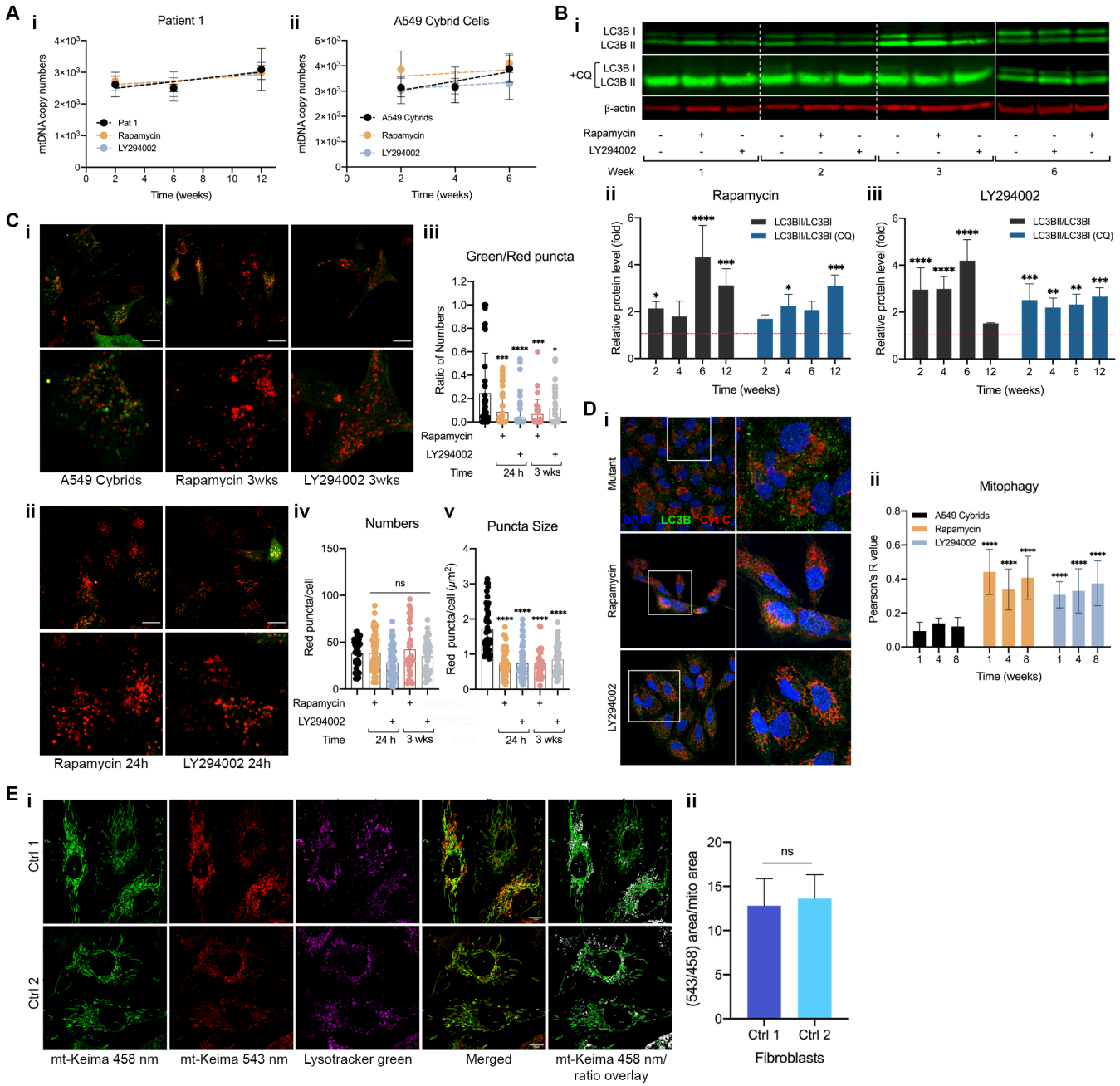
A
i
Patient 1
mtDNA copy numbers
Pat 1
Rapamycin
LY294002
Time (weeks)
ii
A549 Cybrid Cells
A549 Cybrids
Rapamycin
LY294002
Time (weeks)
B
i
LC3B I
LC3B II
+CQ
β-actin
Rapamycin
LY294002
Week
ii
Rapamycin
iii
LY294002
Relative protein level (fold)
LC3BII/LC3BI
LC3BII/LC3BI (CQ)
Time (weeks)
C
i
A549 Cybrids
Rapamycin 3wks
LY294002 3wks
iii
Green/Red puncta
Ratio of Numbers
Time
24 h
3 wks
ii
Rapamycin 24h
LY294002 24h
iv
Numbers
Red puncta/cell
ns
v
Puncta Size
Red puncta/cell (μm²)
D
i
Mutant
Rapamycin
LY294002
DAPI
LC3B
Cyt C
ii
Mitophagy
A549 Cybrids
Rapamycin
LY294002
Pearson's R value
Time (weeks)
E
i
Ctrl 1
Ctrl 2
mt-Keima 458 nm
mt-Keima 543 nm
Lysotracker green
Merged
mt-Keima 458 nm/
ratio overlay
ii
(543/458) area/mito area
ns
Ctrl 1
Ctrl 2
Fibroblasts

526 **FIGURE LEGENDS**

527 **Figure 1. The m.3243A>G mtDNA mutation causes mitochondrial dysfunction and switches cell**
528 **metabolism to a more glycolytic phenotype, resulting in redox imbalance and oxidative stress.**

529 (A) PCR-RFLP and ARM-qPCR were used to quantify the mutation load for patient-derived fibroblasts
530 (n = 3 independent biological samples) and A549 cybrid cells (n = 5 independent biological samples).

531 (B-D) Cell respiratory capacity was measured using the Seahorse XFe96 extracellular flux analyser in
532 patient fibroblasts (B, n = 6 culture wells) and A549 cybrid cells (C, n = 9 culture wells, further
533 normalised to mtDNA copy number), showing a major decrease in oxygen consumption under all
534 conditions. (D) oxygen consumption dependent on ATP production– the response to oligomycin – is
535 plotted.

536 (E) The expression of respiratory chain proteins and supercomplex assembly in patient fibroblasts
537 assessed using blue native gels electrophoresis (BNGE, i) and quantified (ii), showing a major decrease
538 in the assembly of all supercomplexes from the patient-derived cells (n = 3 independent experiments)

539 (F) The mitochondrial membrane potential of fibroblasts was measured using TMRM with confocal
540 microscopy (i) and quantified (ii), showing a significant decrease in potential (n = 5 independent
541 experiments). The images were further analysed using the mitochondrial fragmentation count (MFC)
542 for mitochondrial morphology (iii), confirming the impression of a fragmented phenotype (n=25 cells).
543 Scale bar = 50 μm.

544 (G) ROS production rates of patient fibroblasts were measured using the reporters, DHE (i) and
545 MitoSOX (ii). Rates of production were significantly increased in patient-derived cells (n = 6
546 independent biological samples).

547 (H) The growth rates of patient fibroblasts were measured under a range of different nutrient
548 conditions (normalised to the growth rate of each cell line in regular cell media), showing a decrease
549 of growth rate compared to controls at glucose concentrations of 5 and 1 mM (i) but not at low
550 glutamine (ii) concentrations (n = 6 culture wells for all conditions, 3 independent experiments).

551 (I) Glucose uptake in patient fibroblasts was measured using the fluorescent glucose analogue, 2-
552 NBDG, showing a significantly increased rate of glucose uptake in the patient fibroblasts (n = 15 culture
553 wells).

554 (J) Schematic depicting the simplified mechanism that maintains cytosolic NADH:NAD^+ balance.

555 (K) NADH:NAD^+ ratio of fibroblasts was measured using the reporter, SoNar, under basal conditions
556 and after addition of pyruvate (200 μM, 30 min; i) and quantified (ii; n = 50±10 cells). Scale bar=100
557 μm.

558 (L) Lactate production (normalized to glucose consumption) was measured in the media of fibroblasts
559 using CuBiAn and showed a significant increase in lactate release in the media of patient-derived cells
560 (n = 4 independent biological samples).

561 All data are represented as mean ± s.d. and data were analysed by one/two-way ANOVA with Tukey's
562 multiple comparisons test for fibroblasts and by unpaired t test for cybrid cells (* $p < 0.05$, ** $p < 0.01$,
563 *** $p < 0.001$, **** $p < 0.0001$).

564

565 **Figure S1. The metabolic phenotype of A549 cybrid cells recapitulates the metabolic features of**
566 **patient fibroblasts.**

567 (A) Mitochondrial DNA copy number (ii, n = 5 independent biological samples) of A549 cybrid cells.

568 (B) The mitochondrial membrane potential of A549 cybrid cells measured using TMRM with confocal
569 imaging (scale bar=20 μm, n = 7 independent biological samples).

570 (C-D) Rates of ROS production in A549 cybrid cells and the parental cells were measured using
571 dihydroethidium (DHE), as the rate of increase in red fluorescence intensity over 80 min incubation
572 with DHE. (D) ROS production rates of A549 cybrid cells reported by DHE (i, n = 9 independent
573 biological samples) and MitoSOX (ii, n = 3 independent biological samples).

574 (E-G) A scheme describing how growth rates were obtained by fitting growth curves with an
575 exponential cell growth model (E). Based on the model, growth rate of fibroblasts (n = 3 culture wells)
576 and A549 cybrid cells cultured with regular medium were obtained (n = 5 culture wells, $p = 0.84$; F).
577 (G) Cell growth rates of A549 cybrid cells were measured under a range of different nutrient conditions
578 (normalised to the growth rate of each cell line in regular cell media), showing a decreased rate of
579 growth of A549 cybrid cells compared to controls at glucose concentrations of 5 and 1 mM (i; n = 10
580 culture wells) but not at low glutamine (ii) concentrations (n = 6 culture wells).

581 (H) Glucose uptake in A549 cybrid cells was measured by 2-NBDG, showing a significantly increased
582 rate of glucose uptake in the cybrid cells compared to A549 controls (n=21 culture wells).

583 (I) Schematic depicting the ratiometric probe for NADH:NAD^+, SoNar.

584 (J) NADH:NAD^+ ratio of A549 cybrid cells under basal condition and after addition of pyruvate (200
585 μM, 30 min; i) was measured by the probe and quantified (ii; n = 180 cells).

586 (K) pH in the media from patient fibroblasts cultured for 2 days was measured based on the ratiometric
587 property of the pH indicator in media, phenol red, and showing a lower pH in the media of patient
588 fibroblasts than that of controls (n = 6 independent biological samples).

589 All data are represented as mean ± s.d. and were analysed by one/two-way ANOVA with Tukey's
590 multiple comparisons test for fibroblasts and by unpaired t test for cybrid cells (* $p < 0.05$, ** $p < 0.01$,
591 *** $p < 0.001$, **** $p < 0.0001$).

592

593 **Figure 2. The m.3243A>G mutation rewires glucose and lipid metabolism towards increased**
594 **anabolic biosynthesis and lipid accumulation.**

595 (A) The concentration of metabolites obtained by GC-MS was used to determine the enriched
596 metabolic pathways in patient fibroblasts by MetaboAnalyst 4.0., suggesting that phospholipid
597 biosynthesis, PPP, glycolysis, TCA cycle, etc. were enriched (n = 6 technical replicates.).

598 (B) Schematic of simplified glucose metabolism of the cells (i) Red arrows, upregulated pathways or
599 reactions; three yellow circles of pyruvate and beyond, pyruvate is converted to OAA by pyruvate
600 carboxylase; three or two grey circles of pyruvate and beyond, pyruvate is converted to acetyl-CoA by
601 PDH. Tracing the distribution and abundance of ^{13}C enrichment in the intermediates of glycolysis (ii-
602 viii) and the TCA cycle (ix-xiv) combined with Fig S2A revealed an increase in lipid synthesis and PC
603 activity (n = 4 independent biological samples).

604 (C) Immunoblotting (i) of the expression of pyruvate carboxylase and phosphorylation state of PDH
605 showed an increase of pyruvate carboxylase expression and increased phosphorylation of PDH (which
606 reduces its activity) in patient fibroblasts (ii) and A549 cybrid cells (iii) (n = 3 independent experiments
607 for all cell lines).

608 (D) Nile Red O staining (i) showing the numbers (ii) and area (iii) of lipid droplets in patient fibroblast
609 (n = 20 cells). Scale bar = 50 μm.

610 (E) Lipid profiles of patient fibroblasts acquired by LC-MS were analysed by MetaboAnalyst 4.0.,
611 showing a strikingly increased content of Inositol phosphate, cholesterol esters and sphingomyelin (n
612 = 6 independent biological samples). GPC, glycerophosphatidylcholines. TAG, triacylglycerols. GPE,
613 glycerophosphatidylethanolamines. GPI, glycerophosphatidylinositols. SM, sphingomyelins.

614 All data, except Figs. 2A and 2E, are represented as mean ± s.d. and were analysed by one/two-way
615 ANOVA with Tukey's multiple comparisons test for fibroblasts and by unpaired t test for cybrid cells
616 (* $p < 0.05$, ** $p < 0.01$, *** $p < 0.001$, **** $p < 0.0001$).

617

618 **Figure S2. The metabolomic and lipidomic profiles of fibroblasts carrying the m.3243A>G mutation**
619 **are distinct from that of their matched controls.**

620 (A) The heatmap of metabolite concentrations obtained by GC-MS was generated by MetaboAnalyst
621 4.0 (n = 3 technical replicates), revealing significant differences in the concentrations of several
622 metabolites between controls and patient fibroblasts.

623 (B) PLS-DA for the dataset of Fig. S2A showed that the metabolic profiles of patient fibroblasts were
624 distinct from that of controls.

625 (C) A reduced incorporation of ^{13}C into serine (i) and glycine (ii) and an increase of serine concentration
626 (Fig S2A) in the patient cells (mean ± s.d, of n = 4 independent biological samples).

627 (D) Metabolite set enrichment analysis based on computational enzyme knockout model predicted
628 that pyruvate carboxylase was affected ($p < 0.05$).

629 (E-F) PLS-DA (E) and enriched metabolic pathways (F) for the dataset of Fig. 2E.

630 All data were analysed as stated above (* $p < 0.05$, ** $p < 0.01$, *** $p < 0.001$, **** $p < 0.0001$)

631

632 **Figure 3. The PI3K-Akt-mTORC1 axis is upregulated in the m.3243A>G mutant cells, prompting**
633 **ISR/UPR^{mt} response and perturbing autophagy.**

634 (A) Analysis of RNA-seq data from the patient fibroblasts by QIAGEN Ingenuity Pathway Analysis (IPA)
635 showed the enriched metabolic pathways ($p < 0.05$), matching the findings shown in Figs. 1 and 2.

636 (B) RNA-seq of patient fibroblasts analysed by IPA showed cell signalling pathways which are enriched
637 in cells carrying the m.3243A>G mutation. These include striking and significant increases in
638 expression of pathways involving PI3K-Akt, mTOR, EIF2, and NRF2. It is notable also that PTEN
639 expression, a negative regulator of PI3K-Akt-mTOR signalling was downregulated ($p < 0.05$, Z-score >
640 1; Blue, inhibited; Red, activated).

641 (C) Immunoblotting of p-Akt/Akt (i-ii), p-S6/S6 (iii) and p-AMPK/AMPK (iv) in patient fibroblasts grown
642 in the presence of 10% or 1% FBS media, showing a major increase in p-Akt/Akt and p-S6/S6 in the
643 presence of 1% FBS media in the mutant cells (mean ± s.d. of n = 3 independent experiments).

644 (D) A simple scheme showing the regulation of autophagy and protein translation by the PI3K-Akt-
645 mTORC1 pathway.

646 (E) Immunoblotting of LC3B with chloroquine (CQ, 50 μM for 5 h; n = 4 independent biological samples)
647 or without CQ (n = 7 independent biological samples) in patient fibroblasts (i) and quantified in (ii)
648 suggests an accumulation of LC3BII in the patient cells without an increase in autophagic flux.

649 (F) confocal imaging of live cells transfected with the autophagy reporter, mCherry-GFP-LC3 in patient
650 fibroblasts (i, n=20 cells). The ratio of green/red puncta (ii), autophagosome numbers (iii) and puncta
651 size (iv) were further quantified, showing an increase of these indices. Scale bar = 50 μm.

652 (G) Immunoblotting of p-eIF2α/eIF2α, ATF4, ATF5 and CHOP in patient fibroblasts (i) showed an
653 increase of expression or phosphorylation of these proteins (ii) (n = 3-8 independent experiment).

654 (H) Immunofluorescence staining for p-AKT/AKT (i, n > 60 muscle fibres) and p-S6/s6 (ii, n > 25 muscle
655 fibres) in patient muscle biopsies confirmed the increased phosphorylation of Akt and S6 in the
656 patients (iii). The mutant loads of the m.3243A>G mutation in biopsies were quantified by ARMS-
657 qPCR. Scale bar = 100 μm.

658 (I) Re-analysis of a published RNA-seq data set of patient biopsies collected by Deng *et al.* using IPA
659 confirmed the enrichment of metabolic pathways identified in patient-derived fibroblasts ($p < 0.05$).

660 All data, except Figs. 3A-B and 3I, are represented as mean ± s.d. and were analysed by one/two-way
661 ANOVA with Tukey's multiple comparisons test for fibroblasts and by unpaired t test for biopsies (* p
662 < 0.05, ** $p < 0.01$, *** $p < 0.001$, **** $p < 0.0001$).

663

664 **Figure S3. Analysis for RNA-seq of patient fibroblasts and the enriched metabolic pathways**
665 **recapitulates the metabolic phenotype of patient fibroblasts.**

666 (A-C) RNA-seq showed by a heatmap (A), a volcano plot (B) and 3D-PCA (C). Gene expression in the
667 mutant cells was significantly distinct from both of the controls: 3394 genes were differentially
668 expressed (FDR < 0.05, with 1849 up-regulated and 1545 down-regulated)

669 (D) Analysis of the RNA seq data showing a general decrease in mRNA expression of OxPhos-related
670 genes in patient fibroblasts.

671 (E-F) Analysis of the RNA-seq data showing an altered mRNA expression in antioxidant defence-related
672 genes (E), a reduced mRNA expression of genes involving in the cholesterol synthesis and an altered
673 inositol phosphate metabolism in patient fibroblasts (F).

674 (G) The mRNA expression of TCA cycle and glycolysis genes in patient fibroblasts confirmed our
675 findings in Fig 2, such as increased pyruvate carboxylase and HK1 expression.

676

677 **Figure S4. RNA-seq details of patient fibroblasts and supporting results from A549 cybrid cells.**

678 (A) Detailed analysis of the mRNA expression of multiple genes involved in the PI3K-Akt, mTOR and
679 EIF2 pathways in patient fibroblasts, showing consistent differences in a wide array of genes involved
680 in these pathways.

681 (B) Immunoblotting of p-Akt/Akt, p-S6/S6 and p-AMPK/AMPK in A549 cybrid cells shows increased
682 phosphorylation of Akt and S6 but not of AMPK, consistent with the results of fibroblasts (mean ± s.d.
683 of n = 4-5 independent experiments, two-way ANOVA with Tukey's multiple comparisons test).

684 (C) Immunoblotting of LC3B with CQ (50 µM for 5 h; n = 4 independent biological samples) or without
685 CQ (n = 10 independent biological samples) in A549 cybrid cells (ii) suggests an accumulation of LC3BII
686 without an increase in autophagic flux (iii) as seen in the patient fibroblasts (mean ± s.d., two-way
687 ANOVA with Tukey's multiple comparisons test)

688 (D) Imaging of mCherry-GFP-LC3 (n>20 cells) in A549 cybrid cells (i). The ratio of green/red puncta (ii,
689 p = 0.0375), autophagosome numbers (iii, p = 0.1640) and puncta size (iv, p = 0.0219) were further
690 quantified, showing an increase of green/red puncta and puncta size in the patient cells (mean ± s.d.,
691 unpaired t test for all analyses). Scale bar = 30 µm.

692 (E) Immunoblotting of p-eIF2α/eIF2α, ATF4, ATF5 and CHOP in A549 cybrid cells showed increased
693 expression of all of these proteins, consistent with the results from the patient fibroblasts (mean ± s.d.
694 of n = 5-8 independent experiments, two-way ANOVA with Tukey's multiple comparisons test).

695 All data were analysed as stated above (* p<0.05, ** p<0.01, *** p<0.001, **** p<0.0001).

696

697 **Figure 4. Inhibitors of PI3K, Akt, and mTORC1 reduce mutation load, rescue mitochondrial function**
698 **and reduce glucose dependence.**

699 (A-B) Schematic depicting pharmacological inhibition of the PI3k-Akt-mTORC1 pathway by rapamycin
700 (RP) or LY290042 (LY) (A). (B) Sustained treatment of cells over 6 or 12 weeks with rapamycin (5 µM)
701 or LY290042 (5 µM) caused a progressive decrease in mutant mtDNA load in A549 cybrid cells (i) and
702 fibroblasts of patient 1 (ii) and suppressed the progressive increase of mutant load with time in culture
703 seen in patient 2 fibroblasts (iii) (n = 3 independent experiments). The concentrations of RP and LY
704 here refer to all subsequent treatments.

705 (C) Immunoblotting of the phosphoproteins (p-Akt/Akt, p-mTOR/mTOR and p-AMPK/AMPK; i) and
706 ISR/UPR^{mt} proteins (ii) in patient 1 fibroblasts treated with RP (iiI) or LY (iv) over 12 weeks

707 demonstrated the effective inhibition of Akt or mTORC1 and an amelioration of the integrated stress
708 response (ISR) in the drug-treated cells (n = 3-4 independent experiments).

709 (D) The mitochondrial membrane potential of patient 1 fibroblasts treated with LY or RP for 12 weeks
710 were significantly increased (ii) and mitochondrial fragmentation counts (MFC, iiI) were also
711 significantly reduced (n = 15 independent biological samples). Scale bar = 50 μm.

712 (E) The respiratory capacity of patient 1 fibroblasts treated with LY or RP for 12 weeks was measured
713 using the Seahorse XFe96 extracellular flux analyser and showed a major increase in oxygen
714 consumption under all conditions for the drug-treated cells (n = 15 of culture wells).

715 (F) The $NADH/NAD^+$ ratio of patient 1 fibroblasts treated with LY or RP for 12 weeks was measured
716 under basal condition and pyruvate (i, 200 μM, 30 min) and quantified (ii; n > 180 cells). The result
717 showed a significant decrease compared to pre-treatment levels. Scale bar = 100 μm.

718 (G) Acidification of the growth medium revealed by the absorption ratio of phenol red was significantly
719 reduced after chronic drug treatments with RP and LY (i and ii; n = 9 culture wells). Lactate production
720 normalised to glucose consumption (iii, n = 4 culture wells) was also significantly reduced. In each
721 case, media were collected after 2 days culture of patient 1 fibroblasts treated with LY or RP for 12
722 weeks.

723 (H) Fibroblasts of patient 1 treated with LY or RP for 12 weeks were also cultured in media with a
724 variety of glucose/galactose concentrations to further assess the glucose dependence, displayed a
725 significant improvement of cell growth in all conditions from the drug-treated cells (n = 4-8 culture
726 wells).

727 (I) BNGE were used to assess the expression of respiratory chain proteins and supercomplex assembly
728 of patient 1 fibroblasts treated with LY or RP, showing a major increase in the assembly of almost all
729 supercomplexes from the drug-treated cells (n = 3 independent experiments).

730 (J) Rates of ROS production of patient 1 fibroblasts treated with LY or RP for 12 weeks were
731 significantly reduced to the level that no longer significantly different from controls, which was shown
732 in Fig. 1G (n = 3 independent experiments).

733 All data represented as mean ± s.d. and were analysed by one/two-way ANOVA with Tukey's multiple
734 comparisons test (* $p < 0.05$, ** $p < 0.01$, *** $p < 0.001$, **** $p < 0.0001$).

735

736 **Figure S5. Inhibition of PI3K, Akt, and mTORC1 also reduced mutant load and rescued mitochondrial**
737 **function in A549 cybrid cells.**

738 (A-B) Immunoblotting (i) of the phosphoproteins (p-Akt/Akt, p-S6/S6 and p-AMPK/AMPK; A) and
739 ISR/UPR^{mt} proteins (B) in A549 cybrid cells treated with RP (ii) or LY (iii) over 6 weeks demonstrate the
740 effective inhibition of Akt or mTORC1 and a decrease of the ISR in the drug-treated cells (n = 3
741 independent experiments).

742 (C) The mitochondrial membrane potential of A549 cybrid cells significantly increased after exposure
743 to LY or RP for 6 weeks (i and ii). Mitochondrial fragmentation counts (MFC, iii) were also reduced
744 following treatment with either compound (n = 5 independent biological samples). Scale bar = 25 μm.

745 (D) Cell respiratory capacity of A549 cybrid cells treated with LY or RP for 6 weeks was measured using
746 the Seahorse XFe96 extracellular flux analyser, and showed a major increase in oxygen consumption
747 under all conditions after treatment (n = 18 culture wells).

748 (E-I) MK2206, an inhibitor of pan-Akt (E), treatment (1 μM) also reduced mutant load in A549 cybrid
749 cells over 6 weeks of treatment (F, n = 3 independent experiments). Immunoblotting of p-Akt/Akt and
750 p-S6/S6 (G) confirmed the effect of MK2206 (n = 3 independent samples). Mitochondrial membrane
751 potential (H) and cell respiratory capacity (I, n = 8 culture wells) of A549 cybrid cells also increased
752 after treatment with MK2206.

753 (J) PCR-RFLP was applied to measure the change in mutant load in 143B cybrid cells carrying the
754 m.8993T>G mutation (N80, with 80% mutant mtDNA; N50, with 50% mutant mtDNA) treated with LY
755 or RP for 8 weeks, showing no significant effect on the mutant load of the m.8993T>G (n = 3
756 independent biological samples).

757 (K) Cytosolic NADH:NAD$^+$ ratio of A549 cybrid cells transfected with the genetically encoded probe
758 SoNar and treated with LY or RP for 6 weeks was measured (i) and quantified (ii) under basal condition
759 and following exposure to pyruvate (200 μm, 30 min; n > 30 cells).

760 (L) The absorption ratio of phenol red was used to measure the pH of the growth media (i and ii, n=10
761 culture wells) and the kit of the CuBiAn instrument was used to measure lactate production (iii, n = 4
762 culture wells). Both acidification of the medium and lactate secretion were reduced after 2 days
763 culture of A549 cybrid cells treated with LY or RP for 6 weeks.

764 (M) BNGE were used to measure supercomplex assembly and In Gel activity of A549 cybrid cells after
765 6 weeks of treatment with LY or RP (n = 3 independent experiments).

766 (N) Rates of ROS production of A549 cybrid cells treated with LY or RP for 6 weeks were reduced to
767 the level that no longer significantly different from WT cells, which was shown in Fig. S1C-D (n = 9
768 culture wells).

769 All data represented as mean ± s.d. and were analysed by one/two-way ANOVA with Tukey's multiple
770 comparisons test (* $p < 0.05$, ** $p < 0.01$, *** $p < 0.001$, **** $p < 0.0001$).

771

772 **Figure 5. Reduction of the m.3243A>G mutant load by inhibition of PI3K-Akt-mTORC1 requires**
773 **neither selective cell death nor clonal expansion and is a cell-autonomous event.**

774 (A) A flow chart describing the cell culture process (i) used to assess cell growth/death (ii) over the 4-
775 or 8-weeks drug treatments and single cell PCR for the m.3243A>G mutant loads using TaqMan SNP
776 genotyping (iii).

777 (B) Cell growth (i and ii) and cell death (iii and iv) over the 4- or 8-weeks drug treatments of A549
778 cybrid cells (i and iii) and patient 1 fibroblasts (ii and iv) were measured using the Incucyte (n=6 culture
779 wells). Although treatment with either LY or RP at 5 µM slowed cell proliferation in both patient 1
780 fibroblasts and cybrid cells (i and ii), the cell death numbers were also lowered by the drug treatments
781 (iii and iv).

782 (C-D) A scatter plot showing the distribution of WT and mutant mtDNA measured in single A549 cybrid
783 cells treated with LY or RP for 4 weeks showed a clear shift of mutant load distribution. (C). Mutant
784 load distributions of single A549 cybrid cells (i, n > 800 cells) and patient 1 fibroblasts (ii n > 500 cells)
785 treated with LY or RP for 4 and 8 weeks, respectively.

786 All data represented as mean ± s.d. and were analysed by one/two-way ANOVA with Tukey's multiple
787 comparisons test (* $p < 0.05$, ** $p < 0.01$, *** $p < 0.001$, **** $p < 0.0001$).

788

789 **Figure S6. TaqMan SNP genotyping can be used at single cell resolution to measure the distribution**
790 **of mutant mtDNA burden in a cell population.**

791 (A) Cell growth and cell death of A549 cybrid cells were measured before and after treatment with MK
792 for 4 weeks (n = 8 culture wells). The drug had no specific effect on the mutant cells.

793 (B-C) TaqMan SNP genotyping was validated by measuring the mutation load in a whole population of
794 cells (B, n = 3 independent biological samples) and then to establish the range of mutant load at the
795 level of single cells in the A549 cybrid cells (C).

796 (D) Immunofluorescence staining for COXIV (i and quantified in ii) showed that the expression of COXIV
797 in patient 1 fibroblasts was significantly lower than that of control 1 (n = 100 cells), while LY or RP
798 treatments restored its expression (iii, n > 60 of cells). The histograms (iv and v) display the

799 heterogeneous distribution of intensities measured at the single cell level in control 1 and patient 1
800 fibroblasts.

801 All data are represented as mean ± s.d. and were analysed by one/two-way ANOVA with Tukey's
802 multiple comparisons test (* $p < 0.05$, ** $p < 0.01$, *** $p < 0.001$, **** $p < 0.0001$).

803

804 **Figure 6. Autophagy/mitophagy is necessary to reduce the m.3243A>G mutant load following**
805 **inhibition of the PI3K-Akt-mTORC1 pathway.**

806 (A) In fibroblasts of patient 1, immunoblotting (i) of LC3B with or without CQ (50 μm for 5 h on the
807 day of experiments) over 12 weeks drug treatments (ii and iii) showed a major increase in autophagic
808 flux in drug-treated cells (n = 3 of independent experiments).

809 (B) Confocal imaging of the autophagy reporter, mCherry-GFP-LC3 (n = 25 cells) in patient 1 fibroblasts
810 treated with LY or RP at the indicated time points (i, 6 weeks, and ii, 24 h). The ratio of green/red
811 puncta (iii), autophagosome numbers (iv) and puncta size (v) were further quantified, showing a major
812 decrease in the ratio of green/red puncta and puncta size in response to the treatments. Scale bar =
813 50 μm.

814 (C) Imaging of the mitophagy reporter (i), mitoKeima, was used to specifically quantify mitophagy in
815 patient fibroblasts treated with LY, RP or CQ (10 μM). Quantification of the mitochondrial area fraction
816 engulfed in autolysosomes in both patient 1 (ii) and 2 (iii) were quantified and showed a dramatic
817 increase in mitophagy in both patient cell lines, which was completely prevented by treatment with
818 chloroquine (n = 7-10 independent biological samples).

819 (D-E) A549 cybrid cells (D) and patient 1 fibroblasts (E) were cultured with the inhibitors RP and LY as
820 in all prior experiments but in combination with CQ (10 μM), showing that CQ completely prevented
821 the decrease of mutant load in response to inhibition of the PI3K-Akt-mTORC1 pathway (n = 3
822 independent experiments).

823 (F) A scheme describing how the m.3243A>G mutation alters cell metabolism, including mitochondrial
824 dysfunction, altered glucose metabolism, redox imbalance and oxidative stress, which leads to the
825 constitutive activation of the PI3K-Akt-mTORC1 pathway and a defect in autophagy/mitophagy.
826 Pharmacological inhibition of this pathway reduces mutant load, rescues mitochondrial function and
827 reduces glucose dependence. These findings suggest that the activation of the PI3K-Akt-mTORC1
828 pathway drives a positive feedback cycle, which maintains/increases mutant mtDNA, augments the
829 metabolic rewiring and thus worsens cell signalling perturbation. This positive feedback loop may
830 shape the phenotype of the disease and determine disease progression.

831 All data are represented as mean ± s.d. and were analysed by one/two-way ANOVA with Tukey's
832 multiple comparisons test (* $p < 0.05$, ** $p < 0.01$, *** $p < 0.001$, **** $p < 0.0001$).

833

834 **Figure S7. Mitochondrial biogenesis and changes in mtDNA copy number do not explain the**
835 **reduction of mutant mtDNA burden, while autophagy/mitophagy is also upregulated by inhibition**
836 **of the PI3K-Akt-mTORC1 pathway in A549 cybrid cells.**

837 (A) Quantitative PCR assessing mtDNA copy numbers of patient 1 fibroblasts (i) and A549 cybrid cells
838 (ii) over the 6- or 12-weeks of treatments (n = 3 independent experiments).

839 (B) In A549 cybrid cells, immunoblotting of LC3B with or without CQ (50 μm for 5 h on the day of
840 experiments) throughout drug treatments (i) showed a major increase in autophagic flux in drug-
841 treated cells (ii and iii, n = 3 independent experiments).

842 (C) Imaging of mCherry-GFP-LC3 (n > 30 cells) in A549 Cybrid cells treated with LY or RP at the indicated
843 time points (i and ii). The ratio of green/red puncta (iii), autophagosome numbers (iv) and puncta size
844 (v) were further quantified, showing a major decrease in the ratio of green/red puncta and puncta
845 size. Scale bar = 20 μm.

846 (D) Immunofluorescence staining for LC3B and cytochrome c (i) indicating that mitophagy of A549
847 cybrid cells was increased by LY or RP treatments (ii, n > 40 cells).

848 (E) Imaging of mtKeima (i) showing that mitophagy of WT fibroblasts (ii) was much higher than patient
849 fibroblasts (compared with Fig. 6C, ii and iii).

850 All data are represented as mean ± s.d. and were analysed by one/two-way ANOVA with Tukey's
851 multiple comparisons test (* $p < 0.05$, ** $p < 0.01$, *** $p < 0.001$, **** $p < 0.0001$).

KEY RESOURCES TABLE

REAGENT or RESOURCE	SOURCE	IDENTIFIER
Antibodies		
Mouse Ab anti-OxPhos(human) cocktail (1:1000)	Invitrogen	Cat#45-8199
Rabbit mAb anti-SDHA (1:1000)	Abcam	Cat#ab137040
Mouse mAb anti-ATP5A [15H4C4] (1:1000)	Abcam	Cat#ab14748
Rabbit pAb anti-PC (1:1000)	Novus Biologicals	Cat#NBP1-49536
Rabbit pAb anti-phospho-PDHA(Ser293) (1:1000)	Millipore	Cat#AP1062
Mouse pAb anti-PDHA (1:1000)	Invitrogen	Cat#45-6600
Rabbit pAb anti-phospho-Akt(Ser473) (1:1000)	Cell Signaling Technology	Cat#9271
Rabbit pAb anti-Akt (1:3000)	Cell Signaling Technology	Cat#9272
Rabbit mAb anti-phospho-S6 ribosomal protein (Ser235/236) (1:3000 IB; 1:200 IHC)	Cell Signaling Technology	Cat#4858
Rabbit mAb anti-S6 ribosomal protein (1:3000 IB; 1:200 IHC)	Cell Signaling Technology	Cat#2217
Rabbit mAb anti-phospho-AMPKα(Thr172) [40H9] (1:1000)	Cell Signaling Technology	Cat#2535
Rabbit pAb anti-AMPKα (1:3000)	Cell Signaling Technology	Cat#2532
Rabbit mAb anti-LC3B [D11] (1:3000 IB; 1:500 IF)	Cell Signaling Technology	Cat#3868
Rabbit pAb anti-phospho-eIF2α(Ser51) (1:1000)	Cell Signaling Technology	Cat#9721
Rabbit pAb anti-eIF2α (1:3000)	Cell Signaling Technology	Cat#9722
Rabbit mAb anti-ATF4 [D4B8] (1:1000)	Cell Signaling Technology	Cat#11815
Rabbit pAb anti-ATF5 (1:1000)	Abcam	Cat#ab60126
Mouse mAb anti-GADD153[B-3] (CHOP; 1:1000)	Santa Cruz Biotechnology	Cat#sc-7351
Mouse mAb anti-β-actin[C4] (1:10000)	Santa Cruz Biotechnology	Cat#sc-47778
Goat anti-Mouse IgG IRDye® 680RD	Li-COR Biosciences	Cat#926-68070
Goat anti-Rabbit IgG IRDye® 800CWV	Li-COR Biosciences	Cat#926-32211
Mouse mAb anti-Akt(pan)[40D4] (1:200)	Cell Signaling Technology	Cat#2920
Rabbit mAb anti-phospho-Akt(Ser473) (1:200)	Abcam	Cat#ab81283
Mouse mAb anti-Cytochrome c (1:200)	BD Pharmingen	Cat#556432
Mouse mAb anti-MTCO1[1D6E1A8] (1:100)	Abcam	Cat#ab14705
Biological Samples		
Human muscle biopsies	Division of Neuropathology, UCL Queen Square Institute of Neurology	https://www.ucl.ac.uk/ion/clinical-divisions/division-neuropathology
Chemicals, Peptides, and Recombinant Proteins		
Rapamycin mTORC1 inhibitor	Cayman Chemical	Cat#13346
LY294002 PI3K inhibitor	Cayman Chemical	Cat#70920
MK-2206 AKT inhibitor	Cayman Chemical	Cat#11593
Chloroquine	Cayman Chemical	Cat#14194
Tetramethylrhodamine methyl ester (TMRM)	Invitrogen	Cat#T668
Dihydroethidium (DHE)	Invitrogen	Cat#D11347
MitoSOX	Invitrogen	Cat#M36008
2-NBDG	Invitrogen	Cat#N13195
SYTOGreen Nucleic Acid Stain	Invitrogen	Cat#S7572
LysoTracker Green DND-26	Invitrogen	Cat#L7526
^{13}C-glucose	Goss Scientific	Cat#CLM-1396-1
Nile red	Sigma-Aldrich	Cat#72485

Critical Commercial Assays		
Seahorse XF Cell Mito Stress Test Kit	Agilent	Cat#103015-100
Seahorse XFe96 FluxPak	Agilent	Cat#102416-100
Glucose Assay (384 tests)	OPTOCELL technology	Cat#200106
Lactate Assay (348 tests)	OPTOCELL technology	Cat#200115
Lipofectamine™ 3000 Transfection Reagent	Invitrogen	Cat#L3000001
Human Dermal Fibroblasts Nucleofector Kit	Lonza	Cat#VPD-1001
The Custom TaqMan SNP Genotyping Kit	Applied Biosystems	Cat#4332073
TaqPath ProAmp Master Mix	Applied Biosystems	Cat#A30866
Deposited Data		
Experimental Models: Cell Lines		
A549 cybrid cells	Ian Holt (MRC National Institute for Medical Research, London)	N/A
143B cybrid cells	Michael Minczuk (MRC Mitochondrial Biology Unit, Cambridge, UK)	N/A
Human fibroblasts (controls and patients)	MRC CNMD Biobank London	https://www.ucl.ac.uk/child-health/mrc-cnmd-biobank-london
Oligonucleotides		
Primers for the m.3243A>G PCR-RFLP: Forward: GCCTACTTCACAAAGCGCCTTC; Reverse: AGAAGAGCGATGGTGAGAGCTAAG	Nigou et al., 1998	Sigma-Aldrich
Primers for the m.3243A>G ARMS-qPCR: Forward (3243A): CAGGGTTTGTTAAGATGGCAtA; Forward (3243G): CAGGGTTTGTTAAGATGGCAtG; Reverse: TGGCCATGGGTATGTTGTTA	Wang et al., 2011	Sigma-Aldrich
Primers for the m.8993T>G PCR-RFLP: Forward: CCGACTAATCACCACCCAAC; Reverse: TGTCGTGCAGGTAGAGGCTT	White et al., 2005	Sigma-Aldrich
Recombinant DNA		
SoNar (NADH:NAD^+ ratio reporter)	Zhao et al., 2015	N/A
Autophagy reporter mCherry-EGFP-LC3	Addgene	Cat#22418
Mitophagy reporter mt-Keima	Addgene	Cat#56018
Software and Algorithms		

Seahorse Wave Desktop 2.6 software	Agilent	https://www.agilent.com/en/products/cell-analysis/cell-analysis-software/data-analysis/wave-desktop-2-6
Fiji	Schindelin et al., 2012	https://imagej.net/Fiji
MetaboAnalyst 4.0	Chong et al., 2019	https://www.metaboanalyst.ca/MetaboAnalyst/home.xhtml
Ingenuity Pathway Analysis	Qiagen	Cat#830018
Morpheus	The Broad Institute	https://software.broadinstitute.org/morpheus
NetworkAnalyst 3.0	Xia et al., 2015	https://www.networkanalyst.ca/NetworkAnalyst/home.xhtml
Custom TaqMan® Assay design tool	Thermo Fisher	https://www.thermofisher.com/order/custom-genomic-products/tools/genotyping/
Other		
DMEM, no glucose, no glutamine, no phenol red	Gibco	Cat#A1443001
DMEM, no glucose	Gibco	Cat#11966025
DMEM, high glucose, no glutamine	Gibco	Cat#11960044
Dialyzed Fetal Bovine Serum	Sigma-Aldrich	Cat#F0392

852 **METHODS**

853 **RESOURCE AVAILABILITY**

854 **Lead Contact**

855 Further information and requests for resources and reagents should be directed to and will be fulfilled
856 by the Lead Contact, Michael R Duchen (m.duchen@ucl.ac.uk).

857

858 **Materials Availability**

859 This study did not generate new unique reagents.

860

861 **Data and Code Availability**

862

863 **EXPERIMENTAL MODEL AND SUBJECT DETAILS**

864 **Cell Lines**

865 The A549 cybrid cell line derived from the fusion of enucleated patient cells harbouring the
866 m.3243A>G mtDNA mutation was a gift from Ian Holt (Biodondostia Research Institute, San Sebastián,
867 Spain). The 143B cybrid cell lines with ~50% and ~80% of the m.8993T>G mtDNA mutant loads were
868 gifts from the Minczuk lab (MRC Mitochondrial Biology Unit, Cambridge, UK). Control and patient
869 fibroblasts bearing the m.3243A>G mtDNA mutation were obtained from the MRC Centre for
870 Neuromuscular Disorders Biobank London. The patient fibroblasts with the m.3243A>G mutation
871 were isolated from two female subjects (mother and daughter) at the age of 59 (patient 1) and 35
872 (patient 2) at the time biopsies were taken. For patient 1, the clinical symptoms included diabetes,
873 myoclonus, sensorineural hearing loss, memory decline, myopathy, pigmentary retinopathy and
874 bipolar affective disorder. For patient 2, the symptoms included diabetes, sensorineural deafness,
875 cerebellar ataxia, myopathy, epilepsy, depression and cognitive impairment. These cell lines were
876 cultured in Dulbecco's modified Eagle's medium (Gibco #10566016) supplemented with 10% fetal
877 bovine serum (Gibco #16140071), and 1% Antibiotic-Antimycotic (Gibco #15240096) and incubated at
878 37 °C with 5% CO_2.

879

880 **Human muscle biopsies**

881 The muscle biopsies were from a female patient with the m.3243A>G mutation (at the age of 55) and
882 a matched healthy control. The study was approved by the Queen Square Research Ethics Committee,
883 London (09/H0716/76). Informed consent was obtained from all participants.

884

885 **METHOD DETAILS**

886 **Cell culture and drug treatments for PI3K, Akt, or mTORC1 inhibition**

887 A549 cybrid cells (WT and mutant) and 143B cybrid cells were passaged every 3-4 days at 80%
888 confluence and trypsinised using 0.25% trypsin-EDTA (Gibco #25200056). Similarly, control and
889 patient fibroblasts were passaged every week in the same way. Media with or without drugs were
890 changed every 2-3 days. For drug treatments, rapamycin (Cayman Chemical #13346), LY294002
891 (Cayman Chemical #70920) and MK2206 (Cayman Chemical #11593) were dissolved in DMSO (Sigma-
892 Aldrich #D2650) at 10 mM stock concentrations, while chloroquine (Cayman Chemical #14194) was
893 dissolved in PBS at 50 mM for stock. Drugs were subsequently diluted to their working concentrations
894 in media. Heteroplasmy level in the A549 cybrid cells, the 143B cybrid cells and the fibroblasts of
895 patient 1 without treatments did not change significantly throughout the study as assessed by ARMS-
896 qPCR or PCR-RFLP.

897

898 **Measurements for mtDNA mutations**

899 Levels of mtDNA mutation were detected using PCR-restriction fragment length polymorphism
900 (RFLP)(Nigou et al., 1998; White et al., 2005) or allele refractory mutation system (ARMS)-based
901 quantitative PCR (qPCR) analysis (Wang et al., 2011). DNA extractions from frozen cells were
902 performed using the DNeasy Blood & Tissue Kit (Qiagen #69506). Concentrations of DNA samples were
903 quantified using NanoDrop. All primer pairs used can be found in the Key Resources Table. For PCR-
904 RFLP, samples (20 ng/µl, 2 µl) were mixed with the master mixes containing 1 µl primers (10 µM each)
905 and reagents of GoTaq G2 (Promega #M7845) and the final volume was 25 µl. After 30 thermocycles,
906 amplified PCR products (8 µl) were further digested by ApaI (Promega #R6361) for the m.3243A>G
907 and HapII (Promega #R6311) for the m.8993T>G and analysed by a 2% agarose gel with ethidium
908 bromide. Densitometric analysis was performed by Fiji (Schindelin et al., 2012). For ARMS-qPCR,
909 samples were diluted to 0.4 ng/µl. ARMS primer working solutions (5 µM, 1 µl each) and SYBR Green
910 JumpStart Taq ReadyMix (Sigma-Aldrich #S4438) were added together as master mixes for mutant

911 and wild-type genes. DNA samples (3 µl) and master mixes (7 µl) were pipetted into a 96-well PCR
912 plate (Bio-Rad #MLL9651) and PCR amplification performed using the CFX96 Touch Real-Time PCR
913 Detection System (Bio-Rad). Each sample has three technical replicates. Mutant heteroplasmy level
914 (%) was calculated using $1/[1 + (1/2)^{\Delta CT}] \times 100\%$, where ΔC_T (cycle threshold) = $CT_{wild\text{-}type} - CT_{mutant}$.

915

916 **Quantification of relative mtDNA copy number**

917 The relative mtDNA copy number of cells was determined using quantitative PCR with primers for the
918 mtDNA $tRNA^{Leu(UUR)}$ and with primers for the nuclear B2-microglobulin as previously described (Rooney
919 et al., 2015). Standard 96 well PCR plate with optically clear sealing film and CFX96 Real-Time PCR
920 Detection System (Bio-Rad) were used. PCR mix consists of 2 µl of template DNA (3 ng/µl), 2 µl of
921 primer pair (final concentration of 400 nM), 12.5 µl of SYBR Green JumpStart Taq ReadyMix (Sigma-
922 Aldrich) and 8.5 µl of DNase/RNase free H_2O. The thermal cycling conditions were as follow: 50 °C for
923 2 min, 95 °C for 10 min and then 40 cycles of 95 °C for 15 s and 62 °C for 1 min. Each sample has three
924 technical replicates. The following equation was used to determine the relative mitochondrial DNA
925 content, $2 \times 2^{\Delta CT}$, where ΔC_T is nuclear DNA CT value subtracted by mtDNA CT value.

926

927 **The mitochondrial oxygen consumption rate**

928 Measurements of aerobic respiration and glycolysis were conducted with the Seahorse Bioscience
929 XFe-96 bioanalyzer using the Seahorse XF Cell Mito Stress Test Kit (Agilent #103015-100). Cells were
930 seeded on XF96 cell culture microplates (Agilent #102416-100) two days before the experiment (A549
931 cybrid cells, 1×10^4 cells/well; Fibroblasts, 2×10^4 cells/well). On the day of the experiment, the culture
932 medium was replaced with Seahorse XF Base medium (Agilent #103334-100) supplemented with 1
933 mM pyruvate (Gibco #11360070), 2 mM glutamine (Gibco #25030081) and 10 mM glucose (Gibco
934 #A2494001) and incubated for 30 min at 37 °C in a CO_2-free incubator before loading into the Seahorse
935 Analyzer. After measuring basal respiration, the drugs oligomycin (5 µM), FCCP (1 µM, 2 µM), and
936 rotenone/antimycin A (0.5 µM/0.5 µM) were added to each well in sequential order. Data were
937 analysed using the XF Cell Mito Stress Test Report Generator. After the assay, cells were stained with
938 Hoechst 33342 (5 µM; Thermo Scientific #62249) for 30 min. ImageXpress was then used to count the
939 numbers of cell nuclei (cell numbers) in each well. The normalisation of the experiments is based on
940 the relative cell numbers obtained.

941

942 **Mitochondrial membrane potential, $\Delta\psi_m$, and the mitochondrial fragmentation count**

943 Cells were seeded (3 x 10^4/well for A549 cybrid cells; 1 x 10^4/well for fibroblasts) in glass-bottom 24-
944 well plates, 2-3 days before imaging. Cells were washed twice with the recording medium, which was
945 phenol red-free DMEM (Gibco #A1443001) with 10 mM glucose, 1 mM glutamine, 10 mM HEPES,
946 adjusted to pH 7.4; and then incubated with 25 nM tetramethylrhodamine methyl ester (TMRM) for
947 30 min at 37 °C. Cells were imaged with an LSM 880 (Carl Zeiss) confocal microscope using Fluar
948 63x/1.40 oil immersion objective lens at 37 °C. TMRM was excited with a 561 nm Argon laser with an
949 output power of 0.2 mW. MBS 488/561 was used as a beam splitter and emitted fluorescence
950 collected at 564-740 nm. Images were acquired using Zen Black software (Carl Zeiss) and fluorescence
951 intensity was quantified using Fiji with the same threshold across all samples. To quantitatively
952 describe mitochondrial morphology, mitochondrial network fragmentation according to Rehman et
953 al., 2012 was applied. Briefly, thresholding images were binarized and mitochondrial structure of each
954 cell was count with the particle counting and normalised to the total mitochondrial area (μm^2) per cell
955 to obtain the mitochondrial fragmentation count (MFC). To be specific, MFC = (number of particles x
956 100)/total mitochondrial area.

957

958 **ROS measurements**

959 Rate of general ROS production was assessed using dihydroethidium (DHE, Invitrogen #D11347), an
960 intracellular superoxide indicator which is oxidised by superoxide to ethidium which fluoresces red.
961 As for mitochondrial ROS production, MitoSOX (Invitrogen #M36008) was used. One day before the
962 experiment, cells were seeded in a glass-bottom 96-well plate (SensoPlate #655892) at a density of 2
963 x 10^4 cells per well. On the day of the experiment, cells were washed twice with PBS and incubated
964 with 5 µM DHE or MitoSOX in recording medium (phenol red-free DMEM, 10 mM glucose, 1 mM
965 glutamine, 10 mM HEPES, adjusted to pH 7.4). Measurements of fluorescence intensity were taken at
966 intervals of 5 min at 37 °C using the CLARIOstar microplate reader (excitation/emission = 518/606 nm
967 for DHE excitation/emission = 510/580 nm for MitoSOX). The total incubation time for DHE is 1 h and
968 30 min for MitoSOX. The slope of fluorescence intensity was calculated (Fig. S1C) and represents the
969 rate of ROS production.

970

971 **Glucose uptake using 2-NBDG**

972 A fluorescent deoxyglucose analogue, 2-NBDG (Invitrogen #N13195), was employed as a probe to
973 measure rates of glucose uptake by cultured cells. Cells were seeded in a glass-bottom 96-well plate
974 as ROS measurements. On the day of experiments, cells were firstly washed with glucose-free
975 recording media twice and incubated with the glucose-free media for 1 h. After media aspiration,
976 recording media with 2-NBDG (100 µg/ml) were then added into wells and incubated for 30 min. After
977 the incubation, cells were then again washed with glucose-free recording media twice and
978 fluorescence intensity were measured using the CLARIOstar microplate reader (excitation/emission =
979 467/542 nm).

980

981 **Medium pH values**

982 Medium pH values were measured based on the ratiometric property of phenol red, a common pH
983 indicator in media. The absorbance of phenol red change in response to changing pH. Cells were
984 seeded in 96-well plates at a density of 1 x 10^4 cells per well with 200 µl media and cultured for 2 days.
985 On the day of experiments, media of each well were then transferred to a new 96-well plate and
986 measured the absorbance of phenol red at 443 and 570 nm immediately. The higher the absorbance
987 ratios of 443 to 570 nm, the more acidic the media.

988

989 **Glucose and lactate concentrations in media using CuBiAn**

990 Media for pH measurements were then directly used for quantifying glucose and lactate
991 concentrations in media. Samples and fresh media were measured using the CuBiAn HT-270
992 biochemistry analyser (Optocell technology) with its Glucose (#200106) and Lactate Assay Kits
993 (#200115) according to manufacturer instructions.

994

995 **Blue native gel electrophoresis (BNGE) and In Gel activity assays**

996 Mitochondria were isolated from cultured fibroblasts and cell lines according to the method described
997 earlier (ref). Digitonin-solubilized mitochondria proteins (100 µg) were separated on pre-cast 3%-12%
998 gradient blue native gels (Invitrogen #BN1001) according to manufacturer's instructions. After
999 electrophoresis, the gels were electroblotted onto PVDF membrane (Millipore #IPVH00010) and
1000 probed with anti-OxPhos antibody cocktail (1:1000, Invitrogen #45-8199), anti-SDHA (1:1000, Abcam
1001 #ab137040) and anti-ATP5A (1:1000, Abcam #ab14748). The enzymatic activity of different OxPhos

1002 complexes was determined by in-gel assays. For CIV+CI activity, the gels were incubated first in CIV
1003 substrate (50 mg diaminobenzidine and 100 mg cytochrome c in 50 mM phosphate buffer, pH 7.4)
1004 until brown signal was observed and then incubated in CI substrate (0.1 mg/ml NADH, 2.5 mg/ml
1005 Nitrotetrazolium Blue chloride in 100 mM Tris–HCl, pH 7.4) until blue signal appeared. The reaction
1006 was stopped with 10% acetic acid and the gels were washed and scanned.

1007

1008 **SDS-PAGE and immunoblotting**

1009 For immunoblotting, cells were seeded 1-day prior experiments (60 mm plates for the A549 cybrid
1010 cells and 10 cm plates for fibroblasts). To assess autophagic flux, cells were replenished with regular
1011 media for 1 h to prevent starvation-induced autophagy. After 1 h, treatment conditions resumed
1012 either with or without 50 µM chloroquine for 6 h. For other experiments, cells were then washed with
1013 ice-cold PBS once and lysed using 150-300 µl RIPA buffer (Sigma-Aldrich #R0278) with one cOmplete™
1014 Protease Inhibitor Cocktail (Roche #4693116001) tablet and one PhosSTOP Phosphatase Inhibitor
1015 Cocktail (Roche #4906837001) tablet. Cells were then scraped and centrifuged at 16,000 g at 4 °C for
1016 30 min. Protein concentration in the supernatant was quantified using the Pierce BCA Assay Kit
1017 (Thermo Scientific #23227). For immunoblotting, 30 µg of protein samples in NuPAGE 4x LDS Sample
1018 Buffer (Invitrogen #NP0007) and 2% β-mercaptoethanol (Sigma-Aldrich #63689) were boiled at 99ºC
1019 for 5 min. Proteins were separated on 4-12% NuPAGE Bis-Tris polyacrylamide gels (Invitrogen
1020 #NP0335) immersed in MOPS running buffer (Invitrogen #NP0001) and transferred onto PVDF
1021 membranes (Millipore #IPFL00010). Membranes were then incubated in Intercept (TBS) Blocking
1022 Buffer (Li-COR Biosciences #927-60001) for 1 h at room temperature. After addition of primary
1023 antibodies diluted in the blocking buffer with 0.1% Tween-20, membranes were incubated overnight
1024 at 4ºC on a shaker. Subsequently, membranes were incubated with appropriate secondary antibodies
1025 (Li-COR Biosciences; 1:10000; IRDye® 680RD Goat anti-Mouse IgG, #926-68070; IRDye® 800CW Goat
1026 anti-Rabbit IgG, #926-32211) for 1 h at room temperature before signals were developed with the
1027 LiCOR Odyssey CLx system. Densitometry analysis was performed using Fiji. Details of all the
1028 antibodies used in this study can be found in the Key Resources Table. Following is the antibodies and
1029 dilutions for immunoblotting: Anti-PC (1:1000, Novus Biologicals #NBP1-49536), anti-phospho-PDHA
1030 (1:1000, Millipore #AP1062), anti-PDHA (1:1000, Invitrogen #45-6600), anti-p-Akt (1:1000, Cell
1031 Signaling Technology #9271), anti-Akt (1:3000, Cell Signaling Technology #9272), anti-p-S6 (1:3000,
1032 Cell Signaling Technology #4858), anti-S6 (1:3000, Cell Signaling Technology #2217), anti-p-AMPK
1033 (1:1000, Cell Signaling Technology #2532), anti-AMPK (1:3000, Cell Signaling Technology #2532), anti-
1034 LC3B (1:3000, Cell Signaling Technology #3868), anti-p-eIF2α (1:1000, Cell Signaling Technology

1035 #9721), anti-eIF2α (1:3000, Cell Signaling Technology #9722), anti-ATF4 (1:1000, Cell Signaling
1036 Technology #11815), anti-ATF5 (1:1000, Abcam #ab60126), anti-CHOP (1:1000, Santa Cruz
1037 Biotechnology #sc-7351), and anti-β-actin (1:10000, Santa Cruz Biotechnology #sc-47778).

1038

1039 **Live-cell imaging for cell growth and death using the Incucyte platform**

1040 Cells were seeded at a density of 2,000 cells/well in a 96-well plate one-day prior imaging with regular
1041 cell culture media. For cell growth/death in a variety of nutrient conditions, cells were washed with
1042 PBS twice and then DMEM (Gibco #11966025 or #11960044) with different concentration of glucose,
1043 galactose (Sigma-Aldrich #G5388) or glutamine and 10% dialysed FBS (Sigma-Aldrich #F0392) were
1044 added. For drug treatments, media were then replaced with fresh media with/without drugs along
1045 with 20 nM SYTOGreen Nucleic Acid Stain (Invitrogen #S7572) just before imaging. Images were
1046 acquired using the Incucyte with 20X objective every 2 h for a 3-4 days period. Cell confluency and cell
1047 death numbers were analysis on Incucyte software and sequentially extracted. Rates of cell growth
1048 were analysed by fitting the growth curve to the exponential cell growth model (Fig. S1E) using the
1049 solver in Excel, while cell death was obtained by simply normalising the numbers of dead cells
1050 (SYTOGreen stained) to total cell confluency.

1051

1052 **Measurements of cytosolic NADH:NAD$^+$ using SoNar**

1053 The genetically encoded probes, SoNar for NADH:NAD$^+$ ratio, were developed by and obtained from
1054 the Yang's Lab (Chinese Academy of Sciences) (Zhao et al., 2015). For A549 cybrid cells, the cells were
1055 seeded at the density of 4 x 10^4/well in glass-bottom 24-well plates two days before transfection.
1056 Lipofectamine 3000 (Invitrogen #L3000001) was used for transfection according to the manufacturer's
1057 protocol. Specifically, we used 1 µg DNA and the ratio of p3000 to the 3000 reagent was 2:1. The cells
1058 were imaged two days after transfection in recording media with the LSM 880 microscope using
1059 20x/0.8 objective lens at 37ºC. Both probes were excited at 405 and 488 separately and emitted
1060 fluorescence longer than 535 nm was collected. For fibroblasts, Human Dermal Fibroblasts
1061 Nucleofector Kit (Lonza #VPD-1001) was used for transfection according to the manufacturer's
1062 protocol. Specifically, we used 2.5 µg DNA for 5 x 10^5 cells. Similarly, fibroblasts were imaged two days
1063 after transfection with the same conditions as A549 cybrid cells. Images were acquired using Zen Black
1064 software (Carl Zeiss) and analysed using Fiji. Regions of interest (ROI) were generated by thresholding
1065 and binarizing images and average fluorescence intensity in the ROIs for each channel were then
1066 measured. Ratios between the signal excited at 405 nm and 488 nm were calculated.

1067

1068 **Measurement of autophagy and mitophagy using mCherry-EGFP-LC3 and mt-Keima, respectively**

1069 The autophagy reporter, mCherry-EGFP-LC3 (Addgene plasmid #22418), and mitophagy reporter, mt-
1070 Keima (Addgene plasmid #56018) were purchased from Addgene. The procedure of transfection for
1071 A549 cybrid cells and patient fibroblasts was similar to SoNar. Imaging was performed with the LSM
1072 880 microscope using 63x/1.40 oil immersion objective lens at 37 °C. The mCherry-EGFP-LC3 was
1073 excited at 488 and 561 nm separately and emitted fluorescence 500-580 and longer than 600 nm was
1074 collected. Images were acquired using Zen Black software (Carl Zeiss). Numbers and area of
1075 fluorescent particles for each channel were quantified using Fiji by thresholding images. For mt-Keima,
1076 following transfection, the cells were treated as indicated for 24h and imaged via two sequential
1077 excitations (458 nm, green; 561 nm, red) using a 570- to 695-nm emission range. The laser power was
1078 set at the minimum output to allow the clear visualization of the mt-Keima signal and was separately
1079 adjusted for each experimental conditions. At least 10 z-stacks with 0.45 um thickness were acquired
1080 per sample in an experimental set. LysoTracker Green DND-26 (Invitrogen #L7526) was co-imaged
1081 using a 488 nm excitation and a 495-550 nm emission filter, where indicated. The ratio (high F_{543}/F_{458}
1082 ratio area/total mitochondrial area) was used as an index of mitophagy. Ratio (F_{543}/F_{458}) images were
1083 generated using the Ratio Plus plugin in Fiji. High (F_{543}/F_{458}) ratio areas and total mitochondrial area
1084 were binarized, segmented and quantified in Fiji.

1085

1086 **Metabolomics**

1087 Control and patient fibroblasts were plated 24 hrs before the experiment in 10 cm dishes (1 x 10^6
1088 cells/dish). On the day of experiments, the medium was replaced with phenol red-free DMEM with 1
1089 mM glutamine, 10% dialysed FBS (prepared as described in Yuneva et al., 2007) and 10 mM [U-^{13}C]-
1090 glucose (Goss Scientific #CLM-1396-1). After 24 h incubation, cells were washed once with ice-cold
1091 PBS. Metabolites were extracted with adding 500 µl of ice-cold methanol, scraping, and transferring
1092 into tubes on ice. Dishes were then subsequently washed with 250 µl methanol and 250 µl water
1093 containing 2.5 nM of each nor-leucine and scyllo-inositol per sample as internal standards. Finally, 250
1094 µl of chloroform was added and samples were sonicated for 3 rounds (8 min each) at 4 °C. After
1095 centrifugation (18,000 g for 10 min at 4 °C), the upper polar fraction was collected and used for GC-
1096 MS analysis, while he protein pellets were dried, lysed using 62.5 mM Tris buffer (pH 6.8) containing
1097 2% SDS and used for protein quantification using BCA assay (Abcam). Briefly, the polar fraction was
1098 washed twice with methanol, derivatized by methoximation (Sigma, 20 µl, 20 mg/ml in pyridine) and

1099 trimethylsilylation (20 µl of N,O-bis(trimethylsilyl) trifluoroacetamide reagent (BSTFA) containing 1%
1100 trimethylchlorosilane (TMCS), Supelco), and analysed on an Agilent 7890A-5975C GC–MS system.
1101 Splitless injection (injection temperature 270 °C) onto a 30 m + 10 m × 0.25 mm DB-5MS + DG column
1102 (Agilent J&W) was used, using helium as the carrier gas, in electron ionization (EI) mode. The initial
1103 oven temperature was 70 °C (2 min), followed by temperature gradients to 295 °C at 12.5 °C/min and
1104 then to 320 °C at 25 °C/min (held for 3 min). Data analysis and peak quantifications were performed
1105 using MassHunter Quantitative Analysis software (B.06.00 SP01, Agilent Technologies). The level of
1106 labelling of individual metabolites was corrected for the natural abundance of isotopes in both the
1107 metabolite and the derivatization reagent. Abundance was calculated by comparison to responses of
1108 known amounts of authentic standards (Méndez-Lucas et al., 2020). The data were further processed
1109 and visualised by MetaboAnalyst 4.0, using the Pathway Analysis module with the library of human
1110 SMPDB and the Metabolite Set Enrichment Analysis with the library of predicted metabolite sets
1111 (Chong et al., 2019).

1112

1113 **Lipidomics**

1114 Fibroblasts for lipid extraction were grown in 15 cm dishes in DMEM medium supplemented with 1%
1115 FBS until fully confluent. When confluent, cells were counted and about 10^6 cells were washed and
1116 lysed in 0.5 ml water on ice for 5 min. A Folch extraction was performed: 3ml of chloroform/methanol
1117 (2/1) was added to separate lipids in the organic phase and the solution was centrifuged at 4 °C for 30
1118 min. The organic phase was collected and stored in glass vials at -80 °C until the mass spectrometry
1119 analysis was performed. Before MS analysis, chloroform and methanol were evaporated and dried
1120 lipids resuspended in 150 µl MeOH/$CHCl_3$ 8:2. LC-MS measures were carried out by HPLC (Model 1100
1121 series; Hewlett-Packard) coupled to a quadrupole ion-trap mass spectrometer (Esquire-LCTM; Bruker,
1122 Bremen, Germany) equipped with an electrospray ion source (ESI), in both positive and negative ion-
1123 modes. Chromatographic separation of the lipids was carried out at 303 K on a C18 column by injecting
1124 5 µl of the 4 lipid raw extracts (3 biological replicates for each sample) into the column (Kinetex
1125 TMC18; length, 100 mm; particle size, 2.6 µm; internal diameter, 2.1 mm; pore size, 100 Å;
1126 Phenomenex, Torrence, CA, USA). The solvent system consisted of eluent A as CH_3OH/H_2O (7:3, v/v)
1127 containing 12 mM ammonium acetate, and eluant B as CH_3OH also containing 12 mM ammonium
1128 acetate. The linear gradient was run at a constant flow rate of 0.3 ml/min, and went from 30% B to
1129 100% B in 40 min. This was followed by the column wash using 100% B for 15 min, and then column
1130 re-equilibration under the starting conditions (i.e., 30% B). The nebuliser gas was high purity nitrogen
1131 at a pressure of 20 psi to 30 psi, at a flow rate of 6 L/min and 300 °C. The MS scan range was 13,000

1132 U/s in the range of 50 m/z to 1500 m/z, with a mass accuracy of ≈ 100 ppm. The ESI was operated in
1133 positive ion mode for the qualitative and quantitative analysis of lyso-GPC, GPC and SM, and both in
1134 positive and negative ion mode for glycerol-phospholipids classes GPI and GPE. For the structural
1135 assignment of the lipid species, the extracted ion chromatograms from the positive and/or negative
1136 ion full scan data were integrated using the DataAnalysis 3.0 software (Bruker Daltonik, Bremen,
1137 Germany). In particular, for PE, negative ion mode provided a good yield of molecular ions and
1138 information on the length and unsaturation index of the fatty acyl chains, while positive ion mode was
1139 used to confirm the correct assignment by analysis of the neutral loss of the polar head. The lipid
1140 quantitation was performed by integration of the extracted ion chromatograms (XIC), achieved
1141 through the proprietary software Bruker Daltonics esquireLC 4.5. Overall, the following lipid classes
1142 were detected: lysophosphatidylcholines (Lyso-GPC), glycerophosphatidylcholines (GPC), plasmenyl
1143 phosphatidylcholines (plasmenyl-GPC), sphingomyelins (SM), glycerophosphatidylethanolamines
1144 (GPE), plasmenly phosphatidylethanolamines (plasmenyl-GPE), glycerophosphatidylinositols (GPI),
1145 ceramides, and triacylglycerols (TAG), cholesteryl-esters and cholesterol. To compare across samples
1146 the results within a given lipid class, data were normalized with respect the total ion current (TIC) of
1147 this class (relative intra-class quantitation) whilst to compare the results among different lipid classes
1148 the corresponding signal areas were normalized to the total area of different classes in different runs
1149 (normalization to the relative protein amount leads to similar conclusions). Normalized MS data were
1150 further processed and visualised by MetaboAnalyst 4.0, using the Pathway Analysis module with the
1151 library of human SMPDB.

1152

1153 **Nile Red O imaging**

1154 Fibroblasts were plated on imaging coverslips and grown in DMEM medium supplemented with 1%
1155 FBS. After 24 hours, cells were incubated for 5 min with 0.1 µg/ml of Nile Red O (Sigma-Aldrich #72485)
1156 dissolved in imaging buffer (Listenberger et al., 2003). Live cell imaging was performed on a Zeiss 880
1157 confocal microscope, equipped with a 40x objective and exciting cells at 488 nm and collecting
1158 fluorescence longer than 530 nm. Image analysis was performed using Fiji to evaluate the number of
1159 Nile Red positive puncta, likely lipid droplets, and their areas for each cell that was imaged.

1160

1161 **RNA-sequencing**

1162 Fibroblasts for RNA-sequencing were plated in 10 cm dishes with regular media (1 x 10^6 cells/dish) one
1163 day before RNA extraction. RNA extractions were performed using the RNeasy Mini Kit (Qiagen
1164 #74104). Concentrations and quality of RNA samples were quantified using NanoDrop (total RNA >250
1165 ng, A_{260}/A_{280} = 1.8-2.1, A_{260}/A_{230} > 1.7). RNA-sequencing was then performed at UCL Genomics and
1166 analysed by the SARTools R package (Varet et al., 2016). The resulting datasets were further analysed
1167 by Ingenuity Pathway Analysis (IPA, Qiagen) with a threshold of FDR < 0.05 and visualised by Morpheus
1168 (https://software.broadinstitute.org/morpheus) for heatmaps and NetworkAnalyst 3.0 (Xia et al.,
1169 2015) for volcano plots and principal component analysis.

1170

1171 **Immunohistochemistry**

1172 For immunohistochemistry, muscle biopsies were fixed in phosphate buffered saline (PBS) and fixed
1173 in 4% paraformaldehyde (PFA), made in PBS, for 4-8 h at room temperature (RT). Following fixation,
1174 tissues were cryoprotected in 30% sucrose in Diethyl Pyrocarbonate (DEPC) treated PBS, embedded
1175 and frozen in a mixture of 15% sucrose /50% Tissue-Tek OCT (Sakura Finetek), and sectioned in the
1176 coronal plane at 20 µm using a Cryostat (Bright Instruments). Patient muscle biopsies sections were
1177 washed in PBS, blocked in a solution of 5% normal goat serum (Merck KGaA) (v/v) containing 0.1%
1178 Triton X-100 (v/v) (Merck KGaA) in PBS at RT for 2 h. They were first incubated in primary antibodies
1179 at RT overnight. The following antibodies were used: pan-AKT (1:200, Cell Signaling Technology
1180 #2920), phospho-AKT (p-AKT; 1:200, Abcam #ab81283), S6 (1:200), and phospho-S6 (1:200). Following
1181 incubation in primary antibodies, sections were washed in PBS, incubated in biotinylated anti-species
1182 secondary antibodies (1:250; Vector Laboratories) for 2 h. Sections were washed and incubated with
1183 bisbenzimide (10 min in 2.5 µg/ml solution in PBS; Merck KGaA). Images were collected using an SP2
1184 Leica confocal microscope (Leica Microsystems, UK). Sequential images were subsequently
1185 reconstructed using Metamorph imaging software (Universal Imaging Corporation, West Chester, PA).

1186

1187 **Immunofluorescence**

1188 For A549 cybrid cells, the cells were seeded at 1 x 10^5 cells per well in 6-well plates on 22 mm glass
1189 coverslips. On the day of the experiment, cells were replenished with regular media for 1 h to prevent
1190 starvation-induced autophagy. After 1 h, treatment conditions resumed either with or without 50 µM
1191 chloroquine for 6 h. The cells were then washed with PBS twice and fixed in 4% paraformaldehyde for
1192 20 mins at room temperature and permeabilised with 0.2% Triton X-100 in PBS for 5 min. Following
1193 washes with 0.2% Triton X-100 PBS, coverslips were incubated with primary anti-LC3B for

1194 autophagosomes/lysosomes (1:500) and anti-cytochrome c for mitochondria (1:200, BD Pharmingen
1195 #556432) antibodies in 3% BSA 0.2% Triton X-100 PBS at 4 °C overnight. The following day, cells were
1196 washed with 0.2% Triton X-100 PBS and incubated with Alexa Fluor 488-conjugated (goat anti-rabbit,
1197 1:200) and Alexa Fluor 647-conjugated (donkey anti-mouse, 1:500) secondary antibodies for
1198 visualisation of the lysosomes and mitochondria, respectively for 1 h. Following three PBS washes, the
1199 nucleus was counterstained using 5 µg/mL Hoechst 33342 solution diluted 1:2000 in 0.2% Triton X-
1200 100 PBS for 5 min. The coverslips were washed one final time with 0.2% Triton X-100 PBS and mounted
1201 on a glass slide using Fluoromount-G mounting medium (SouthernBiotech), stored at 4 °C until
1202 imaging. Imaging was performed with the LSM 880 microscope using 63x/1.40 oil immersion objective
1203 lens. For tricolour imaging, Hoescht 33342 was excited at 405 nm, Alexa Fluor 488 at 488 nm and Alexa
1204 Fluor 647 at 633 nm. Emitted fluorescence was collected at 410-480 nm, 500-650 nm and longer than
1205 660 nm. Images were acquired using Zen Black software (Carl Zeiss). Image acquisition parameters
1206 settings were maintained for all samples within the experimental set. The colocalisation coefficient
1207 (Pearson's R value) of 647 nm and 488 nm emission signals, LC3B and cytochrome c, was quantified
1208 using Coloc 2 in Fiji.

1209 For fibroblasts, cells were seeded at a density of 5 x 10^4 cells/well in 24 well plates on 10 mm
1210 coverslips. After 24h incubation, cells were treated with LY or RP for 4 weeks and 8 weeks respectively.
1211 After the long-term treatment, the cells were washed thrice with 1X PBS and fixed in 4%
1212 paraformaldehyde for 15 mins at room temperature and permeabilised with 0.1% Triton-X 100 for 15
1213 min in PBS. The cells were then washed and incubated with anti-MTCOI antibody (1:100, Abcam
1214 #ab14705) in 3% BSA for 1h at the room temperature followed by incubation with Alexa Fluor 488-
1215 conjugated secondary antibody for 1h at the room temperature. After antibody labelling, the
1216 coverslips were mounted on a glass slide using ProLong™ Gold Antifade mountant with DAPI and
1217 imaged using the confocal microscope as described above.

1218

1219 **TaqMan SNP genotyping for Single cell qPCR**

1220 Primers for distinguishing WT and the m.3243A>G mutant mtDNA were designed by submitting the
1221 region of the m.3243A>G mutation (~120 bp) to the website of online Custom TaqMan® Assay design
1222 tool (https://www.thermofisher.com/order/custom-genomic-products/tools/genotyping/) The
1223 Custom TaqMan SNP Genotyping Kit (Applied Biosystems #4332073) was ordered and prepared
1224 according to manufacturer instructions. For single cell sorting, cells were resuspended (1 x 10^6 cells/ml
1225 for A549 cybrid cells; 5 x 10^5 cells/ml for fibroblasts) in 1 ml PBS with 1% FBS, filtered through 70 µm

1226 mesh and then kept on ice. Sorting cells to 96-well PCR plates using BD FACS Aria Fusion was
1227 performed by Flow Cytometry Core Facility, Division of Medicine at UCL. Cells in 96-well plates were
1228 lysed with 2 µl of 0.2% Triton X-100 and kept in -80 °C immediately. For qPCR, TaqPath ProAmp Master
1229 Mix (Applied Biosystems #A30866) was mixed with primers of TaqMan SNP genotyping and added into
1230 96-well PCR plates to reach a final volume of 10 µl in each well. Thermo cycles were set according to
1231 manufacturer instructions. Mutant loads were determined by the ratio of mutant to total fluorescent
1232 intensity.

1233

1234 **QUANTIFICATION AND STATISTICAL ANALYSIS**

1235 All statistical analyses, unless otherwise stated in figure legends, were carried out using GraphPad
1236 Prism 8. To compare means between two groups, a two-tailed unpaired t-test was used for normally
1237 distributed data. One/two-way ANOVA with Tukey's multiple comparisons test was performed for
1238 multi-group (at least three) comparisons. Data are presented as graphs displaying mean ± s.d., of at
1239 least three independent biological replicates. Means of control samples on immunoblotting or
1240 immunofluorescence are typically centred at one (or 100%) to ensure easier comparisons unless
1241 otherwise noted. Differences were only considered to be statistically significant when the *p* value was
1242 less than 0.05. Estimated p values are either stated as the actual values or denoted by * $p < 0.05$, ** p
1243 < 0.01, *** $p < 0.001$, **** $p < 0.0001$.

1244 For detailed processing and statistical analysis of RNA sequencing, metabolomics and lipidomics,
1245 please find them in the previous section with the same subheadings.

1246 No statistical method was used to predetermine sample size, and replicates are shown in Figure
1247 legends. The investigators were not blinded to allocation during experiments and outcome
1248 assessment.

1249

1250 **REFERENCES**

1251 de Andrade, P.B.M., Rubi, B., Frigerio, F., van den Ouweland, J.M.W., Maassen, J.A., and Maechler, P.
1252 (2006). Diabetes-associated mitochondrial DNA mutation A3243G impairs cellular metabolic pathways
1253 necessary for beta cell function. Diabetologia *49*, 1816–1826.

1254 Barriocanal-Casado, E., Hidalgo-Gutiérrez, A., Raimundo, N., González-García, P., Acuña-Castroviejo,
1255 D., Escames, G., and López, L.C. (2019). Rapamycin administration is not a valid therapeutic strategy
1256 for every case of mitochondrial disease. EBioMedicine *42*, 511–523.

1257 Cappel, D.A., Deja, S., Duarte, J.A.G., Kucejova, B., Iñigo, M., Fletcher, J.A., Fu, X., Berglund, E.D., Liu,
1258 T., Elmquist, J.K., et al. (2019). Pyruvate-Carboxylase-Mediated Anaplerosis Promotes Antioxidant
1259 Capacity by Sustaining TCA Cycle and Redox Metabolism in Liver. Cell Metab. *29*, 1291-1305.e8.

1260 Castellano, B.M., Thelen, A.M., Moldavski, O., Feltes, M., van der Welle, R.E.N., Mydock-McGrane, L.,
1261 Jiang, X., van Eijkeren, R.J., Davis, O.B., Louie, S.M., et al. (2017). Lysosomal cholesterol activates
1262 mTORC1 via an SLC38A9–Niemann-Pick C1 signaling complex. Science (80-.). *355*, 1306 LP – 1311.

1263 Chae, S., Ahn, B.Y., Byun, K., Cho, Y.M., Yu, M.-H., Lee, B., Hwang, D., and Park, K.S. (2013). A Systems
1264 Approach for Decoding Mitochondrial Retrograde Signaling Pathways. Sci. Signal. *6*, rs4 LP-rs4.

1265 Chen, Q., Kirk, K., Shurubor, Y.I., Zhao, D., Arreguin, A.J., Shahi, I., Valsecchi, F., Primiano, G., Calder,
1266 E.L., Carelli, V., et al. (2018). Rewiring of Glutamine Metabolism Is a Bioenergetic Adaptation of Human
1267 Cells with Mitochondrial DNA Mutations. Cell Metab. *27*, 1007-1025.e5.

1268 Chong, J., Wishart, D.S., and Xia, J. (2019). Using MetaboAnalyst 4.0 for Comprehensive and Integrative
1269 Metabolomics Data Analysis. Curr. Protoc. Bioinforma. *68*, e86.

1270 Civiletto, G., Dogan, S.A., Cerutti, R., Fagiolari, G., Moggio, M., Lamperti, C., Beninca, C., Viscomi, C.,
1271 and Zeviani, M. (2018). Rapamycin rescues mitochondrial myopathy via coordinated activation of
1272 autophagy and lysosomal biogenesis. EMBO Mol Med *10*.

1273 Cotán, D., Cordero, M.D., Garrido-Maraver, J., Oropesa-Ávila, M., Rodríguez-Hernández, Á., Gómez
1274 Izquierdo, L., De la Mata, M., De Miguel, M., Bautista Lorite, J., Rivas Infante, E., et al. (2011).
1275 Secondary coenzyme Q10 deficiency triggers mitochondria degradation by mitophagy in MELAS
1276 fibroblasts. FASEB J. *25*, 2669–2687.

1277 Craven, L., Alston, C.L., Taylor, R.W., and Turnbull, D.M. (2017). Recent Advances in Mitochondrial
1278 Disease. Annu Rev Genomics Hum Genet *18*, 257–275.

1279 Deng, J., Lu, Y., Xie, Z., Liu, J., Yuan, Y., and Wang, Z. (2020). RNA-seq profiling, and impaired autophagic
1280 process in skeletal muscle of MELAS. Biochem. Biophys. Res. Commun. *523*, 91–97.

1281 Deus, C.M., Yambire, K.F., Oliveira, P.J., and Raimundo, N. (2020). Mitochondria–Lysosome Crosstalk:
1282 From Physiology to Neurodegeneration. Trends Mol. Med. *26*, 71–88.

1283 El-Hattab, A.W., Adesina, A.M., Jones, J., and Scaglia, F. (2015). MELAS syndrome: Clinical
1284 manifestations, pathogenesis, and treatment options. Mol. Genet. Metab. *116*, 4–12.

1285 Fessler, E., Eckl, E.-M., Schmitt, S., Mancilla, I.A., Meyer-Bender, M.F., Hanf, M., Philippou-Massier, J.,
1286 Krebs, S., Zischka, H., and Jae, L.T. (2020). A pathway coordinated by DELE1 relays mitochondrial stress
1287 to the cytosol. Nature *579*, 433–437.

1288 Garrido-Maraver, J., Paz, M. V, Cordero, M.D., Bautista-Lorite, J., Oropesa-Avila, M., de la Mata, M.,
1289 Pavon, A.D., de Lavera, I., Alcocer-Gomez, E., Galan, F., et al. (2015). Critical role of AMP-activated
1290 protein kinase in the balance between mitophagy and mitochondrial biogenesis in MELAS disease.
1291 Biochim Biophys Acta *1852*, 2535–2553.

1292 Gaude, E., Schmidt, C., Gammage, P.A., Dugourd, A., Blacker, T., Chew, S.P., Saez-Rodriguez, J., O'Neill,
1293 J.S., Szabadkai, G., Minczuk, M., et al. (2018). NADH Shuttling Couples Cytosolic Reductive
1294 Carboxylation of Glutamine with Glycolysis in Cells with Mitochondrial Dysfunction. Mol. Cell *69*, 581-
1295 593.e7.

1296 Gilkerson, R.W., De Vries, R.L., Lebot, P., Wikstrom, J.D., Torgyekes, E., Shirihai, O.S., Przedborski, S.,
1297 and Schon, E.A. (2012). Mitochondrial autophagy in cells with mtDNA mutations results from
1298 synergistic loss of transmembrane potential and mTORC1 inhibition. Hum Mol Genet *21*, 978–990.

1299 Golla, S., Ren, J., Malloy, C.R., and Pascual, J.M. (2017). Intramyocellular lipid excess in the
1300 mitochondrial disorder MELAS. Neurol. Genet. *3*, e160.

1301 Gorman, G.S., Schaefer, A.M., Ng, Y., Gomez, N., Blakely, E.L., Alston, C.L., Feeney, C., Horvath, R., Yu-
1302 Wai-Man, P., Chinnery, P.F., et al. (2015). Prevalence of nuclear and mitochondrial DNA mutations
1303 related to adult mitochondrial disease. Ann. Neurol.

1304 Guo, X., Aviles, G., Liu, Y., Tian, R., Unger, B.A., Lin, Y.-H.T., Wiita, A.P., Xu, K., Correia, M.A., and
1305 Kampmann, M. (2020). Mitochondrial stress is relayed to the cytosol by an OMA1–DELE1–HRI
1306 pathway. Nature *579*, 427–432.

1307 Haroon, S., Li, A., Weinert, J.L., Fritsch, C., Ericson, N.G., Alexander-Floyd, J., Braeckman, B.P., Haynes,
1308 C.M., Bielas, J.H., Gidalevitz, T., et al. (2018). Multiple Molecular Mechanisms Rescue mtDNA Disease

in C. elegans. Cell Rep *22*, 3115–3125.

Hoxhaj, G., and Manning, B.D. (2020). The PI3K–AKT network at the interface of oncogenic signalling and cancer metabolism. Nat. Rev. Cancer *20*, 74–88.

Janssen, G.M.C., Hensbergen, P.J., van Bussel, F.J., Balog, C.I.A., Maassen, J.A., Deelder, A.M., and Raap, A.K. (2007). The A3243G tRNALeu(UUR) mutation induces mitochondrial dysfunction and variable disease expression without dominant negative acting translational defects in complex IV subunits at UUR codons†. Hum. Mol. Genet. *16*, 2472–2481.

Johnson, S.C., Yanos, M.E., Kayser, E.-B., Quintana, A., Sangesland, M., Castanza, A., Uhde, L., Hui, J., Wall, V.Z., Gagnidze, A., et al. (2013). mTOR Inhibition Alleviates Mitochondrial Disease in a Mouse Model of Leigh Syndrome. Science (80-.). *342*, 1524 LP – 1528.

Kandul, N.P., Zhang, T., Hay, B.A., and Guo, M. (2016). Selective removal of deletion-bearing mitochondrial DNA in heteroplasmic Drosophila. Nat. Commun. *7*, 13100.

Khan, N.A., Nikkanen, J., Yatsuga, S., Jackson, C., Wang, L., Pradhan, S., Kivela, R., Pessia, A., Velagapudi, V., and Suomalainen, A. (2017). mTORC1 Regulates Mitochondrial Integrated Stress Response and Mitochondrial Myopathy Progression. Cell Metab *26*, 419-428 e5.

Koromilas, A.E., and Mounir, Z. (2013). Control of oncogenesis by eIF2α phosphorylation: implications in PTEN and PI3K–Akt signaling and tumor treatment. Futur. Oncol. *9*, 1005–1015.

Kotiadis, V.N., Duchen, M.R., and Osellame, L.D. (2014). Mitochondrial quality control and communications with the nucleus are important in maintaining mitochondrial function and cell health()(). Biochim. Biophys. Acta *1840*, 1254–1265.

Lin, Y.-F., Schulz, A.M., Pellegrino, M.W., Lu, Y., Shaham, S., and Haynes, C.M. (2016). Maintenance and propagation of a deleterious mitochondrial genome by the mitochondrial unfolded protein response. Nature *533*, 416.

Listenberger, L.L., Han, X., Lewis, S.E., Cases, S., Farese, R. V, Ory, D.S., and Schaffer, J.E. (2003). Triglyceride accumulation protects against fatty acid-induced lipotoxicity. Proc. Natl. Acad. Sci. *100*, 3077 LP – 3082.

Maeda, K., Kawai, H., Sanada, M., Terashima, T., Ogawa, N., Idehara, R., Makiishi, T., Yasuda, H., Sato, S., Hoshi, K., et al. (2016). Clinical Phenotype and Segregation of Mitochondrial 3243A>G Mutation in 2 Pairs of Monozygotic Twins. JAMA Neurol. *73*, 990–993.

1338 Manning, B.D., and Toker, A. (2017). AKT/PKB Signaling: Navigating the Network. Cell *169*, 381–405.

1339 McMillan, R.P., Stewart, S., Budnick, J.A., Caswell, C.C., Hulver, M.W., Mukherjee, K., and Srivastava,
1340 S. (2019). Quantitative Variation in m.3243A > G Mutation Produce Discrete Changes in Energy
1341 Metabolism. Sci. Rep. *9*, 5752.

1342 Méndez-Lucas, A., Lin, W., Driscoll, P.C., Legrave, N., Novellasdemunt, L., Xie, C., Charles, M., Wilson,
1343 Z., Jones, N.P., Rayport, S., et al. (2020). Identifying strategies to target the metabolic flexibility of
1344 tumours. Nat. Metab. *2*, 335–350.

1345 Mick, E., Titov, D. V, Skinner, O.S., Sharma, R., Jourdain, A.A., and Mootha, V.K. (2020). Distinct
1346 mitochondrial defects trigger the integrated stress response depending on the metabolic state of the
1347 cell. Elife *9*.

1348 Molenaars, M., Daniels, E.G., Meurs, A., Janssens, G.E., and Houtkooper, R.H. (2020). Mitochondrial
1349 cross-compartmental signalling to maintain proteostasis and longevity. Philos. Trans. R. Soc. B Biol.
1350 Sci. *375*, 20190414.

1351 Morán, M., Delmiro, A., Blázquez, A., Ugalde, C., Arenas, J., and Martín, M.A. (2014). Bulk autophagy,
1352 but not mitophagy, is increased in cellular model of mitochondrial disease. Biochim. Biophys. Acta -
1353 Mol. Basis Dis. *1842*, 1059–1070.

1354 N'Diaye, E.-N., Kajihara, K.K., Hsieh, I., Morisaki, H., Debnath, J., and Brown, E.J. (2009). PLIC proteins
1355 or ubiquilins regulate autophagy-dependent cell survival during nutrient starvation. EMBO Rep. *10*,
1356 173–179.

1357 Nigou, M., Parfait, B., Clauser, E., and Olivier, J.L. (1998). Detection and quantification of the A3243G
1358 mutation of mitochondrial DNA by ligation detection reaction. Mol. Cell. Probes *12*, 273–282.

1359 Picard, M., and Hirano, M. (2016). Disentangling (Epi)Genetic and Environmental Contributions to the
1360 Mitochondrial 3243A>G Mutation Phenotype: Phenotypic Destiny in Mitochondrial Disease? JAMA
1361 Neurol. *73*, 923–925.

1362 Picard, M., Zhang, J., Hancock, S., Derbeneva, O., Golhar, R., Golik, P., O'Hearn, S., Levy, S., Potluri, P.,
1363 Lvova, M., et al. (2014). Progressive increase in mtDNA 3243A>G heteroplasmy causes abrupt
1364 transcriptional reprogramming. Proc Natl Acad Sci U S A *111*, E4033-42.

1365 Plotegher, N., and Duchen, M.R. (2017). Mitochondrial Dysfunction and Neurodegeneration in
1366 Lysosomal Storage Disorders. Trends Mol. Med. *23*, 116–134.

1367 Quirós, P.M., Prado, M.A., Zamboni, N., D'Amico, D., Williams, R.W., Finley, D., Gygi, S.P., and Auwerx,
1368 J. (2017). Multi-omics analysis identifies ATF4 as a key regulator of the mitochondrial stress response
1369 in mammals. J. Cell Biol. *216*, 2027–2045.

1370 Raimundo, N., Song, L., Shutt, T.E., McKay, S.E., Cotney, J., Guan, M.-X., Gilliland, T.C., Hohuan, D.,
1371 Santos-Sacchi, J., and Shadel, G.S. (2012). Mitochondrial Stress Engages E2F1 Apoptotic Signaling to
1372 Cause Deafness. Cell *148*, 716–726.

1373 Rehman, J., Zhang, H.J., Toth, P.T., Zhang, Y., Marsboom, G., Hong, Z., Salgia, R., Husain, A.N., Wietholt,
1374 C., and Archer, S.L. (2012). Inhibition of mitochondrial fission prevents cell cycle progression in lung
1375 cancer. FASEB J. *26*, 2175–2186.

1376 Rooney, J.P., Ryde, I.T., Sanders, L.H., Howlett, E.H., Colton, M.D., Germ, K.E., Mayer, G.D.,
1377 Greenamyre, J.T., and Meyer, J.N. (2015). PCR based determination of mitochondrial DNA copy
1378 number in multiple species. Methods Mol Biol *1241*, 23–38.

1379 Russell, O.M., Gorman, G.S., Lightowlers, R.N., and Turnbull, D.M. (2020). Mitochondrial Diseases:
1380 Hope for the Future. Cell *181*, 168–188.

1381 Schindelin, J., Arganda-Carreras, I., Frise, E., Kaynig, V., Longair, M., Pietzsch, T., Preibisch, S., Rueden,
1382 C., Saalfeld, S., Schmid, B., et al. (2012). Fiji: an open-source platform for biological-image analysis.
1383 Nat. Methods *9*, 676–682.

1384 Schon, E.A., DiMauro, S., and Hirano, M. (2012). Human mitochondrial DNA: roles of inherited and
1385 somatic mutations. Nat Rev Genet *13*, 878–890.

1386 Shpilka, T., and Haynes, C.M. (2018). The mitochondrial UPR: mechanisms, physiological functions and
1387 implications in ageing. Nat. Rev. Mol. Cell Biol. *19*, 109–120.

1388 Stewart, J.B., and Chinnery, P.F. (2015). The dynamics of mitochondrial DNA heteroplasmy:
1389 implications for human health and disease. Nat. Rev. Genet. *16*, 530.

1390 Suen, D.-F., Narendra, D.P., Tanaka, A., Manfredi, G., and Youle, R.J. (2010). Parkin overexpression
1391 selects against a deleterious mtDNA mutation in heteroplasmic cybrid cells. Proc. Natl. Acad. Sci. *107*,
1392 11835 LP – 11840.

1393 Suomalainen, A., and Battersby, B.J. (2018). Mitochondrial diseases: the contribution of organelle
1394 stress responses to pathology. Nat Rev Mol Cell Biol *19*, 77–92.

1395 Szczepanowska, J., Malinska, D., Wieckowski, M.R., and Duszynski, J. (2012). Effect of mtDNA point

1396 mutations on cellular bioenergetics. Biochim. Biophys. Acta - Bioenerg. *1817*, 1740–1746.

1397 Valera-Alberni, M., and Canto, C. (2018). Mitochondrial stress management: a dynamic journey. Cell
1398 Stress *2*, 253–274.

1399 Varet, H., Brillet-Guéguen, L., Coppée, J.-Y., and Dillies, M.-A. (2016). SARTools: A DESeq2- and EdgeR-
1400 Based R Pipeline for Comprehensive Differential Analysis of RNA-Seq Data. PLoS One *11*, e0157022.

1401 Wang, J., Venegas, V., Li, F., and Wong, L.J. (2011). Analysis of mitochondrial DNA point mutation
1402 heteroplasmy by ARMS quantitative PCR. Curr Protoc Hum Genet *Chapter 19*, Unit 19 6.

1403 White, H.E., Durston, V.J., Seller, A., Fratter, C., Harvey, J.F., and Cross, N.C.P. (2005). Accurate
1404 Detection and Quantitation of Heteroplasmic Mitochondrial Point Mutations by Pyrosequencing.
1405 Genet. Test. *9*, 190–199.

1406 Wojewoda, M., Duszyński, J., and Szczepanowska, J. (2011). NARP mutation and mtDNA depletion
1407 trigger mitochondrial biogenesis which can be modulated by selenite supplementation. Int. J.
1408 Biochem. Cell Biol. *43*, 1178–1186.

1409 Xia, J., Gill, E.E., and Hancock, R.E.W. (2015). NetworkAnalyst for statistical, visual and network-based
1410 meta-analysis of gene expression data. Nat. Protoc. *10*, 823–844.

1411 Yambire, K.F., Fernandez-Mosquera, L., Steinfeld, R., Mühle, C., Ikonen, E., Milosevic, I., and
1412 Raimundo, N. (2019). Mitochondrial biogenesis is transcriptionally repressed in lysosomal lipid storage
1413 diseases. Elife *8*, e39598.

1414 Yuneva, M., Zamboni, N., Oefner, P., Sachidanandam, R., and Lazebnik, Y. (2007). Deficiency in
1415 glutamine but not glucose induces MYC-dependent apoptosis in human cells . J. Cell Biol. *178*, 93–105.

1416 Zhao, Y., Hu, Q., Cheng, F., Su, N., Wang, A., Zou, Y., Hu, H., Chen, X., Zhou, H.M., Huang, X., et al.
1417 (2015). SoNar, a Highly Responsive NAD+/NADH Sensor, Allows High-Throughput Metabolic Screening
1418 of Anti-tumor Agents. Cell Metab *21*, 777–789.

1419 Zheng, X., Boyer, L., Jin, M., Kim, Y., Fan, W., Bardy, C., Berggren, T., Evans, R.M., Gage, F.H., and
1420 Hunter, T. (2016). Alleviation of neuronal energy deficiency by mTOR inhibition as a treatment for
1421 mitochondria-related neurodegeneration. Elife *5*.

1422

1423 **ACKNOWLEDGEMENTS**

1424 We thank Benoit Bilanges (UCL Cancer Institute) for invaluable discussions and guidance, Alice
1425 Giustacchini (UCL ICH) for help with single cell analyses, Stephanie Carrington (Division of
1426 Neuropathology, UCL IoN) for sectioning the muscle biopsies, and Metabolomics STP of the Francis
1427 Crick Institute for assistance with GC-MS analysis. We also acknowledge The MRC Centre for
1428 Neuromuscular Diseases Biobank (supported by the National Institute for Health Research Biomedical
1429 Research Centres at Great Ormond Street Hospital for Children NHS Foundation Trust and at
1430 University College London Hospitals NHS Foundation Trust and University College London) for
1431 providing all patient-derived cells used in this study. NP was supported by Marie Sklodowska-Curie
1432 Individual Fellowship (Horizon 2020 Grant No. 653434) RDSP is supported by a Medical Research
1433 Council Clinician Scientist Fellowship (MR/S002065/1). GS is supported by Telethon GGP16026 and
1434 CRUK Pioneer Award C28472/A29264. MY is supported by the Francis Crick Institute which receives
1435 its core funding from Cancer Research UK (FC001223), the UK Medical Research Council (FC001223),
1436 and the Wellcome Trust (FC001223). We also thank Action Medical Research for funding the early
1437 stages of this work and the Taiwan government for funding CYC's PhD Fellowship.

1438